Universidad de Concepción
Dirección de Postgrado
Facultad de Ciencias Físicas y Matemáticas
Programa de Doctorado en Ciencias Físicas

Cinemática del gas central de Galaxias Activas cercanas con ALMA. (Central gas kinematics of nearby Active Galaxies with ALMA)

Tesis presentada para optar al grado académico de Doctor en Ciencias Físicas

Roy Lawrence Slater Clement
Mayo 2018
Concepción - Chile

Profesor Guía: Neil Mark Nagar
Departamento de Astronomía
Facultad de Ciencias Físicas y Matemáticas
Universidad de Concepción

Agradecimientos

There are many people whom I am grateful to meet along this path. First, I would like to express my sincere gratitude to my advisor, Professor Neil Nagar for his guidance and support in several ways throughout my time as his student. I have known a good scientist but more important, a very good person.

Also a special thanks to Venkatessh Ramakrishnan (Venki) for his important scientific contribution, for the good free times and also, his constant “good vibes“ to complete this adventure as well as Pierluigi Cerulo to support with the format of the present document.

Of course a special mention to the old glories of the astronomy and physics department Gustavo-Agape, Matias-Blana, Cesar, Caddy, Ale-Melo, Heinz, Gustavo-Aguayo, Negro as well as some newer ones as Pedro, Dania y Pame and everyone who have shared a lot of good moments and allowed an enriching experience.

I can not leave out to Professor Michael Fellhauer and his wife Annette for their constant understanding, lots of eternal talks and total disposal to help in anything.

Agradezco también al Grupo EDA, del cual formé parte en sus inicios siendo uno de sus fundadores, y a través de este darme cuenta el gran interés que despierta la astronomía en la comunidad en general y lo importante que resulta la divulgación científica. Logré apreciar personalmente el positivo cambio entre lo que era antes y en lo que se ha convertido ahora en conjunto con una gran labor logística de Marllory Fuentes: el grupo de divulgación científica mas importante de la Universidad y la mejor cara visible al exterior del departamento de astronomía.

Un especial y afectuoso agradecimiento a la gente fuera de la astronomía, que de estar todos los días con la mente en el Universo te permiten aterrizar: Los eternos Taito, Ariel, Ervinero, que siempre tuvieron el tiempo para molestar y recordarme en todo momento que tenía que terminar la Tesis; a ‘la colonia española’ compuesta por Ana, JuanJo, Miquel y Karina; a los partners JP, el arquitecto anarquista Begno y Karen; a la Sita Lucy por sus esquisitos almuerzos y su incomparable y casi incalculable calidez humana y casi un sinfín de otras personas mas allá de la ciudad de Concepción que de alguna u otra manera estuvieron siempre enviando entre bromas a buenas vibras como Hector, Wassap, Julio, Ximenacion y Marita.

Una especial dedicación también a mi padre loco por el fútbol y colo-colo William, y mi madre Estela, quien batalló durante mi tramo final del postgrado con un cancer y que logró vencer. Agradecer a ambos que soportar a este engendro de la naturaleza que optó

por cosas no convencionales y extensas para su desarrollo profesional, pero que aún así apoyaron en todo incluso con hasta lo que no tenían.

Agradezco el apoyo de CONICYT a través de su Beca/Nacional-Doctorado 21120516, como también a los fondos adicionales facilitados a mi persona para el término del programa de doctorado como el Programa Financiamiento Basal PFB-06 ETAPA II y el PROYECTO FONDECYT 1171506.

Adicionalmente y para terminar, mis mas sincero e inmenso agradecimiento al equipo de fútbol de la Facultad de Ciencias Físicas y Matemáticas (CFyM), que con la invitación de Raúl originó el punto de inflexión para los tremendos momentos que estaban por venir. A los jugadores-estudiantes Gerald Rivas, Geovanni Moreno, Bastian Ocampo, Daniel Rosas, Felipe Carrasco, Francisco Muñoz, José Barraza, Jhon Sanzana, Luis Lagos, Felipe Vargas, Alexis Adasme, Pablo Catril, Matias Vicencio, Patricio Muñoz, Marcelo Figueroa, Matias Cofré, Tomas Benavente, Matias Cartes, Cristian Reyes, Eduardo Pulgar, Raúl Dominguez y Alex Alarcón, solo agradecerles por la oportunidad de descargar toda mi obsesión por el fútbol e ideas locas siendo su D.T. y que junto a una gran generación de estudiantes como fueron ustedes, pasar a la historia de nuestra Facultad con un tercer lugar el 2016 y consagrar el año 2017 como Campeones del torneo de verano de segunda división por primera vez en la historia de nuestra Facu, en la ardua competencia del campeonato de fútbol universitario mas antiguo y grande de Chile: El Interfacultades UdeC.

Resumen

Para trazar flujos entrantes y salientes en núcleos de galaxias activas (AGNs), determinar la masa de gas involucrada y su impacto en la galaxia huésped y en el agujero negro central, se requieren estudios en imágenes 3-D de tanto gas ionizado como molecular. Estudios previos de imagen han revelado una correlación entre la presencia de espirales nucleares de polvo en escalas de unos cientos de parsecs con una actividad nuclear en galaxias, sugiriendo que tales estructuras trazan el flujo de alimentación al agujero negro supermasivo en el núcleo (SMBH). Como adición, estudios cinemáticos de gas ionizado y gas molecular caliente (2000 K) usando unidades de campo integral (IFU) en galaxias activas cercanas, han revelado flujos entrantes con velocidades de ∼50 km s^{-1} a lo largo de espirales de polvo. No obstante, las tasas de flujo de masa en esas fases del gas son usualmente pequeñas (10^{-4} – 10^{-3} M yr^{-1}) e interpretadas a ser solamente la piel caliente de una reserva de gas mucho mayor y flujo – el cual debería estar dominado por gas molecular frío. Dado esto, ALMA se convierte en el instrumento ideal para mapear tanto la distribucion espacial como la cinemática de este gas molecular frío de manera de cuantificar el flujo nuclear entrante y saliente presente a la misma escala probada por medio de observaciones en el rango óptico e infrarrojo cercano.

Este trabajo mostrará la cinemática y morfología del gas molecular a ∼0.5″de resolución (CO J:2-1 con ALMA) dentro del kiloparsec mas central en una muestra de 5 galaxias Seyferts seleccionadas por mostrar flujos entrantes de ∼50 km s^{-1} a lo largo de espirales nucleares de polvo en observaciones previas con IFU en en el rango óptico. Se presentan los diferentes métodos que resultan útiles para analizar la cinemática del gas a las escalas mas internas para cada fuente en nuestra muestra, para despues mostrar como estos métodos, una vez aplicados en una de las galaxias de nuestro interés (NGC 1566), nos permite realizar un análisis mas profundo para los distintos componentes detectados en la region nuclear a través d mapeos con una resolución espacial y espectral significativa como lo obtenido con el telescopio Gemini (GMOS-IFU) y especialmente, con el radiotelescopio ALMA (Banda 6 desde ciclo-1 y ciclo-2). Justamente para NGC 1566, se presentan observaciones de ALMA de la emisión de CO J:2-1 a una resolución de 24 pc espacial y ∼2.6 km s^{-1} espectral; observaciones de Gemini-GMOS/IFU de emisión de gas ionizado, y lineas de absorción estelar a resolución espacial similar, y 123 km s^{-1} de resolución espectral intrínseca. La morfología y cinemática estelar, molecular (CO) y de

gas ionizado ([NII]) son comparadas con las esperadas desde, flujos salientes y corrientes de flujo entrantes. Mientras que tanto el gas ionizado como molecular muestran signos de rotación, existen importantes movimientos no circulares en la region mas interna a 200 pc (CO and [NII]) y a lo largo de brazos espirales en el kpc central (CO). El núcleo muestra un perfil de doble peak de CO (ancho máximo a intensidad cero de 200 km s^{-1}), y lóbulos prominentes (∼80 km s^{-1}) con corrimiento al azul y al rojo son encontrados a lo largo del eje menor en el arco de segundo mas interno. Perturbaciones por la barra de gran escala puede explicar cualitativamente, pero no cuantitativamente todas las características en el campo de velocidades observado. Estamos a favor entonces de la presencia de un flujo saliente molecular en el disco con velocidades reales de ∼180 km s^{-1} en el núcleo y desacelerando hasta ∼0 en ∼72 pc. La tasa de flujo saliente molecular implicada es de 5.6 [$M_\odot$ yr^{-1}], con este gas acumulándose en los brazos nucleares a 2″. La cinemática del gas ionizado apoya una interpretación de un flujo saliente similar pero mas esférico, en la región mas interna a 100 pc, sin signos de desaceleración. Existe cierta evidencia de corrientes de flujo entrante de ∼50 km s^{-1} a lo largo de brazos espirales especificos o secciones, y la tasa de masa del flujo entrante molecular, ∼0.1 [$M_\odot$ yr^{-1}], es significativamente mayor que la tasa de acreción del SMBH (m = 4.8×10^{-5} [$M_\odot$ yr^{-1}]).

Abstract

Tracing nuclear inflows and outflows in active galactic nuclei (AGNs), determining the mass of gas involved in these, and their impact on the host galaxy and nuclear black hole, requires 3-D imaging studies of both the ionized and molecular gas. Previous imaging studies have revealed a correlation between the presence of dusty nuclear spirals at scales of hundred of parsecs and nuclear activity in galaxies, suggesting that such structures trace the feeding flow to the nuclear supermassive black hole (SMBH). In addition, studies of ionized gas and hot (2000 K) molecular gas kinematics using integral field units (IFU) in nearby active galaxies, have revealed inflows with velocities of ∼50 km s^{-1} along the dusty spirals. Nevertheless, the mass flow rates in these gas phases are usually small (10^{-4} – 10^{-3} M yr^{-1}) and interpreted to be only the hot skin of a much larger gas reservoir and flow – which should be dominated by cold molecular gas. Giving this, ALMA becomes in the ideal instrument to map both the spatial distribution and kinematics of this cold molecular gas in order to quantify the actual nuclear inflows and outflows at the same scale probed by the optical and near-IR observations.

This work will show molecular gas kinematics and morphology at ∼0.5″of resolution (CO J:2-1 with ALMA) within the inner kiloparsec in a sample of 5 nearby Seyferts selected for showing inflows of ∼50 km s^{-1} along dusty nuclear spirals in previous optical IFU observations. It presents, the different methods which result useful to analyze the gas kinematics at inner scales to each source of our sample, to then show how these methods, once applied in one of the galaxies of our interest (NGC 1566), allow us to make a deeper analysis for the different components detected in the nuclear region through maps with significant spatial and spectral resolution as obtained with Gemini telescope (GMOS-IFU) and specially, with the ALMA radiotelescope (Band 6 from cycle-1 and cycle-2). Justly for NGC 1566, it presents ALMA observations of the CO J:2-1 emission at 24 pc spatial and ∼2.6 km s^{-1} spectral resolution; Gemini-GMOS/IFU observations of ionized gas emission lines and stellar absorption lines at similar spatial resolution, and 123 km s^{-1} of intrinsic spectral resolution. The morphology and kinematics of stellar, molecular (CO) and ionized ([NII]) emission lines are compared to the expectations from rotation, outflows, and streaming inflows. While both ionized and molecular gas show rotation signatures, there are significant non-circular motions in the innermost 200 pc (CO and [NII]) and along spiral arms in the central kpc (CO). The nucleus shows a double-peaked

CO profile (Full Width at Zero Intensity of 200 km s^{-1}), and prominent (~80 km s^{-1}) blue and redshifted lobes are found along the minor axis in the inner arcseconds. Perturbations by the large-scale bar can qualitatively, but not quantitatively, explain all features in the observed velocity field. We thus favour the presence of a molecular outflow in the disk with true velocities of ~180 km s^{-1} at the nucleus and decelerating to ~0 by ~72 pc. The implied molecular outflow rate is 5.6 [$M_\odot$ yr^{-1}], with this gas accumulating in the nuclear 2″ arms. The ionized gas kinematics support an interpretation of a similar, but more spherical, outflow in the inner 100 pc, with no signs of deceleration. There is some evidence of streaming inflows of ~50 km s^{-1} along specific spiral arms or sections, and the estimated molecular mass inflow rate, ~0.1 [$M_\odot$ yr^{-1}], is significantly larger than the SMBH accretion rate (m = 4.8×10^{-5} [$M_\odot$ yr^{-1}]).

Contents

List of Figures

List of Tables

1 Introduction

1.1 General Context

The study of formation and evolution of galaxies has became in one of the greatest topics in the understanding of the Universe. Galaxies are far from being considered static structures since they are constantly evolving in time. For this, they can be found in the Universe in several morphologies with different properties. Therefore, to study them, normally they are classified into different morphological types like in the classical galaxy classification scheme of Hubble (Hubble, 1926). This classification put galaxies into categories of elliptical, spiral, barred spiral and irregulars, subdividing these with respect to properties such as the amount flattening of ellipticals as the arm shapes and bulge sizes of spirals. The galaxies are arrayed in a *tuning fork*, normally interpreted as the evolutionary sequence where galaxies evolve from a spiral morphology consisting of two types of paths (the right-hand of the tuning fork) to an elliptical one (the left hand o the tuning fork). More recent and sophisticated schemes has been proposed to study the evolution of galaxies, allowing to learn more about transitions processes like galaxy merging, interactions with companions as well as internal dynamic galactic processes that may occur. One of the most popular diagrams so far is the bimodal colour-magnitude distribution of galaxies which leads to a natural classification into 'blue star forming' and 'red passive' galaxies (e.g. Baldry et al., 2004). In general, this diagram shows in the nearby Universe that blue (red) galaxies have high (low) star formation rates, which means that galaxies are divided into star forming and quiescent galaxies based on their level of star formation activity. The regions are named as 'the red sequence' and 'the blue cloud' and between these two

distributions there is an underpopulated space known as 'the green valley' where galaxies hosted are characterized by a quenched star formation by inefficient gas reservoirs as well as others by hosted an active galactic nucleus which cause that the most part of the gas being destroyed very quickly due to feedback processes (see Sect. 1.4). Thus, from this diagram we can conclude that there must be a significant process (or processes) at some point during the evolution of galaxies that could produce these bimodality and active galaxies is proposed to be one of these processes due to its potential capability of heats or disrupts the gas, and hence slows down star formation. However this is not a solved problem yet. The energy from an AGN comes from a single very small radius which are often obscured by dust being very difficult to model how this could interacts with the surrounding gas. the traditional belief is that it heats up the gas and slows star formation, but there is evidence that it might not really have any major effect on the star formation rate at all; it might just heat up the central gas, and push the star formation out to a more distant radius rather than shutting it down or slowing it down. For all of this, the AGN becomes in a very important topic which could have a greater effect on star formation in galaxies an so in the galaxy evolution. In recent years, it has been realised that feedback phenomena, due to star formation or the AGN itself, can produce substantial gas outflows, self-regulating the inflow and the fueling. In the following sections, all these processes are described.

1.2 Active Galaxies

We know that a galaxy is a large gravitationally bounded structure composed of stars, gas, dust, energy and dark matter which emits large amount of electromagnetic radiation in different wavelengths. Typically, these radiation is linked predominantly to thermal radiation and emitted by the 'normal components' (stars,gas and dust), but in certain situations the emission spreads over full wavelength range, with an important fraction of the radiation as not thermal and emitted just by a very compact region located in the most central part of the galaxy at the point that sometimes overcomes the luminosity of stars in the visible spectrum and is usually accompanied by important ejections of matter. When this happens, we are under the presence of a galaxy hosting an *Active Galactic Nuclei* (AGN) which is called *Active Galaxy*.

There are different classes of active galaxies which are often classified in terms of their

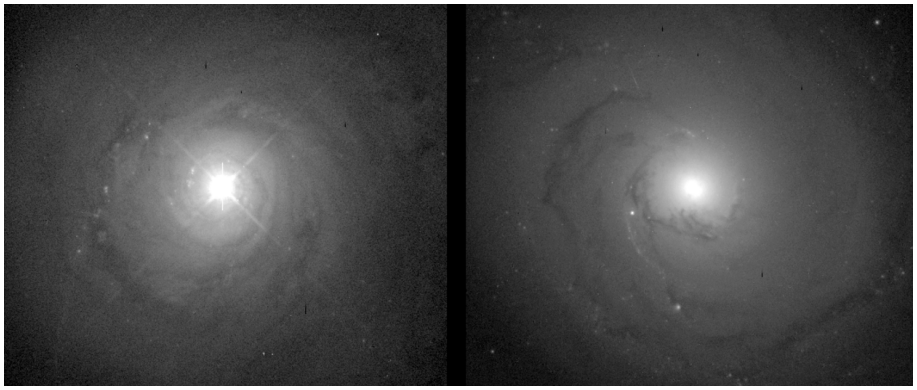

Figure 1.1 Active and non-active galaxy comparison. Optical images of the active galaxy NGC 5548 (left panel) compared with the non-active NGC 3277 (right panel). Both images were produced with the F606W filter from *Hubble Space Telescope* (*HST*) and displayed with the same brightness intensity scale to allow direct comparison. Source: *HST* (M. Malkan and M. Carollo).

physical appearances and the radiation they emit. Two of most numerous are the Quasars and Seyferts. Quasar galaxies are the most luminous (between $\sim 10^{45}$–10^{47} ergs s^{-1}) and typically distant systems (redshifts z=0.1 to ~7) whose radiation emitted by his nucleus, overcomes for almost 100 times the luminosity of a entire normal galaxy, whereas Seyfert galaxies morphologically are spiral galaxies which typically are hosted in the nearby universe and have a nuclear activity much less luminous than quasars (between $\sim 10^{43}$–10^{45} ergs s^{-1}) such that the galaxy can be clearly detectable. Apparently in a 10% of the all nearby galaxies reside Seyfert nuclei (Ho et al., 1997a), although considering galaxies with *low-ionization nuclear emission line regions* (*LINER* galaxies, Heckman, 1980), nowadays considered as a low-luminosity extension of Seyferts ($\sim 10^{39}$–10^{42} ergs s^{-1}), the estimation increases close to 50% (Ho et al., 1994, 1997a).

Differences between active and non-active galaxies can be clearly noted, by looking to a direct comparison from optical images between two galaxies with similar morphology and distance as in Fig. 1.1. On this, the active galaxy NGC 5548 (left panel) shows an unusual brighter nuclear region than the normal galaxy NGC 3277 (right panel). This brighter emission (see the diffraction pattern apparent as the diagonal spikes from the nucleus) is not from stars but is thought to be ultimately powered by material falling in the gravitational field of the supermassive black hole (SMBH) at the center of NGC 5548. Similar non-stellar emission is also seen at the center of many other nearby galaxies (Malkan et al., 1998; Baillard et al., 2011; Kauffmann et al., 2003; Davies et al., 2016).

The size of the active nucleus depends of the wavelength observed. In optical images as the example of Fig. 1.1, the nucleus is compact, but this changes at radio images where radiation extends much further away (e.g. see the prototypical radio source Cygnus A in Perley et al., 1984). Additionally to its characteristic luminosity that became them in the most luminous objects in the universe, other main features are:

- *Its non-thermal spectrum*, remarkably different of stellar spectra and so for normal galaxies where the energy distribution peak is founded at some specific wavelength and temperature roughly following the black-body spectrum (Wien law: $\lambda_{\max}\mathrm{T}$ = cte.), while an AGN emits in all regions of the electromagnetic spectrum, independently of the emission wavelength;

- *Its prominent and large-intensity emission lines*[1], in contrast with non-active galaxies. These lines are mainly broad (~800–8000 km s^{-1}) and have high ionization levels indicating a non-stellar and very strong ionizing source. Within the most typical are with low ionization lines like [OI] 6300Å, [NII] 6548+6584Å, [SII] 6716Å, [SII] 6731Å and high ionization lines like [OIII] 5007Å or [NeV] 3426Å;

- *Its emission variability*, with respect to the time, which in some cases become significantly important in a few days only. Its importance lies in allowing to estimate the size of the emission regions by measuring the time delay between continuum and emission lines originated from a region of photoionized gas close to the (SMBH) known as the broad line region (BLR) (Laor, 2004; Czerny & Hryniewicz, 2011);

- *Its relativistic jet of matter*, which some of them are strong radio emitters which are produced by electrons moving through magnetic fields close to the speed of light (synchrotron radiation). The ionized matter can extend beyond the hosted galaxy along the axis of rotation, reaching several millions of parsecs (pc) away in length.

We know about the existence of AGN since the decade of 30's and 40's and today the scientific community are still trying to figure out what exactly is happening on inside of them and what makes them distinguishable from each other. An important discovery of the past few years has been the fact that all nearby galaxies contain very compact,

[1]With the exception of BL-Lac objects which does not show neither strong emission nor absorption lines.

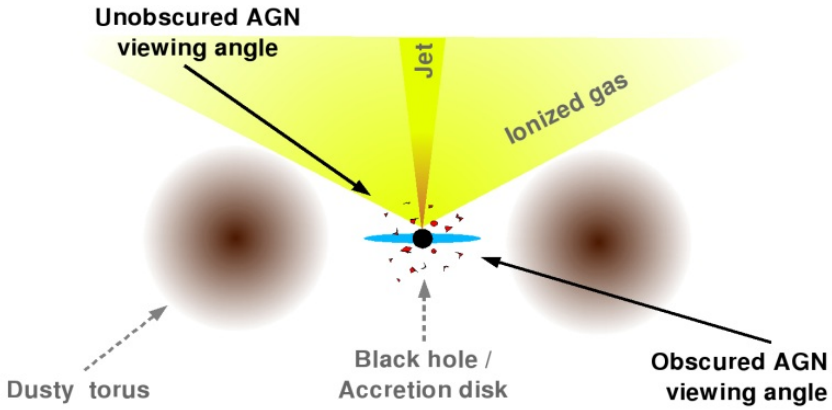

Figure 1.2 AGN Drawn scheme (not to scale). The central Black Hole accretes matter until make an accretion disk and emits high energy radiation which can ionize gas on the surroundings. Source: www.southampton.ac.uk.

gravitating nuclei which can only be massive black holes (Lynden-Bell & Rees, 1971; Kormendy & Richstone, 1995). According to this, our best model so far is that SMBHs are the ultimate power sources for active galaxies. In Fig. 1.2 we can find a representative scheme of how an AGN looks. The current model that generates greater consensus is that SMBH accretes matter forming an accretion disk around it which emits high ionizing radiation that affects the gas in the surroundings. Often this radiation can be seen in the form of the powerful relativistic jet extending over millions of parsecs. A dusty region similar as a donut that surrounds the SMBH known as Torus, can absorb a lot of the emitted radiation. If the orientation of the AGN is such that radiation reaches Earth directly (without passing through the Torus), we would see an unobscured AGN. Otherwise, an obscured AGN would be observed. In some cases, this obscuration can absorb most of the AGN light. In the follow section we will see how the torus is playing an important role to explain the different AGN types present in the Universe.

1.3 The Unified Model of AGN

As was mentioned above, AGN have properties in common and a similar nuclear structure (Fig. 1.2), however the different classes of AGN appear quite differently. Seyfert, QSOs[2], Radio-galaxies, Blazars, exhibit different observational characteristics such as in

[2]In modern terminology, the expression QSO encompasses both Quasars and the radio-quiet QSOs.

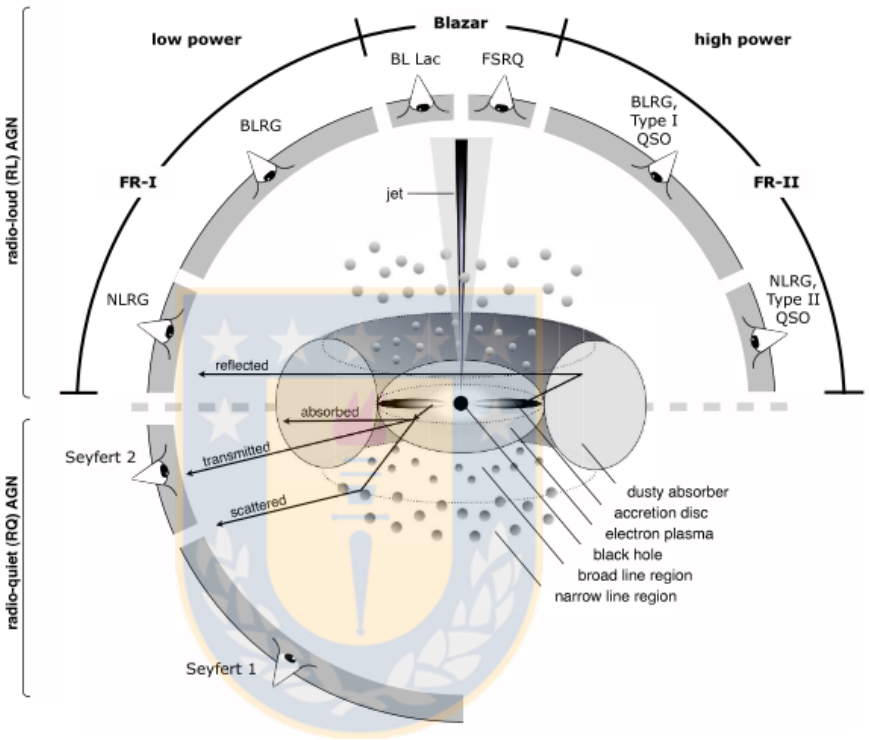

Figure 1.3 The unified model of AGN. Schematic representation with the different components and the possible orientations associated to different types of them (not to scale). The torus is the structure named as 'dusty absorber'. In the radio loud side, it shows: The Fanaroff-Riley classification (FR-I and FR-II) for high and low luminosity (see more in Fanaroff & Riley, 1974); the narrow and broad line radio galaxies (NLRG and BLRG, respectively); Type 1 and 2 for Quasi-Stellar Objects (QSO) and the Blazar types BL Lacertae (BL Lac) and flat-spectrum radio Quasars (FSRQ). Source: Beckmann & Shrader (2012).

flux intensity, variability, and emission lines. Thus an important question is whether the different classes of AGN are intrinsically different or such differences lie in the fact that we observe them at different angles. This concern has led to a model where the AGN are not different among them but they only *appear* to be different as a consequence of their orientation with respect to the line of sight (*LOS*). More specifically, this model proposes that the torus of gas and dust obscures the nuclear emission, producing the different characteristics observed when is viewed from different angles (see Fig. 1.3 for an illustration of the unified model of AGN).

Thus, the central purpose behind the 'AGN unification' is that the physics is the same for all AGN and their apparent diversity depends very strongly in the inclination of an dusty torus which, due to its optically thick nature, permits the escape of radiation to only a certain solid angles along the *LOS*. This model was described in Antonucci (1993) to mainly give and explanation about the different types observed in Seyferts (Seyfert 1 and Seyfert 2 in Fig. 1.3) and later in Urry & Padovani (1995) to analogously explain the differences for radio-loud galaxies.

1.4 Feeding and Feedback in Nearby Active Galaxies

The two most important conditions for producing an AGN are (1) the existence of a central SMBH, and (2) a sufficient amount of gas to fuel the nucleus. Therefore, to understand the formation of AGN, we must understand how SMBHs form and which mechanisms are responsible for transporting gas towards the center of the host galaxy to feed the black hole. In this section, we discuss the general aspects about the latter and demonstrate that not only the feeding processes participate in the relationship between SMBH and host galaxy, but also exist feedback processes in parallel which have a significant impact on avoiding an abundant formation of massive and luminous galaxies in the Universe as well to limit the growth of the SMBH, namely, a key role in the evolution of galaxies which have been empirically verified with several strong correlations (e.g. the widely used correlation for a stellar classical bulge in Ferrarese & Merritt, 2000; Gebhardt et al., 2000).

There are two known mechanism with the SMBH intimately relates with the host galaxy: via gas accretion, which requires inflows (feeding processes), and winds or jets, normally referred as outflows (feedback processes).

1.4.1 Feeding: Inflows

Gas inflows trigger the mass accretion in the SMBHs. The amount of mass involved in the fueling of an AGN can be a small fraction of the total mass of the host galaxy. As an example, median values for bolometric luminosities of nearby nuclei is $L_{Bol} \approx 3{\times}10^{40}$ ergs s^{-1} and assuming an accretion efficiency of 10% thought for geometrically thin accretion disks (Soltan, 1982), the required accretion rate is just around 5×10^{-6} $M_\odot$ yr^{-1}, which is a pitifully miniscule amount, in comparison with the amount of fuel actually available to be accreted (Ho, 2008). So, in principle, there is no difficulty in having a sufficiently large gas reservoir, the problem is how to funnel the required amount of gas into a very small region. Assuming first that the gas reservoir is cold, so that the pressure of the gas does not resist accretion, the gas accretion would be impossible if the gas has a significant amount of angular momentum. For example, taking into account a parcel of gas in a typical galaxy of mass 10^{11} $M_\odot$, and we want transfer it from a hypothetical distance of 10 kpc (galactic scales) to 0.1 pc (innermost nuclear scales) and assuming a SMBH mass around 10^8 $M_\odot$, its specific angular momentum (given by $j \sim \sqrt{GMR}$) must be reduced by a factor of 10^4, which clearly means that the formation of an AGN must be connected with events in which the gas in the host galaxy can lose its angular momentum very effectively. These events are still part of an intense discussion by the scientific community. To the date, there are some observational and theoretical evidence trying to elucidate what are the inflow-triggered mechanisms. There are many mechanisms proposed in the removal of angular momentum in the host galaxy and provide fuel to the central parsec (e.g. Martini, 2004, see their Fig. 1 and references therein) which can be divided between gravitational and hydrodynamic mechanisms. The formers (e.g. galaxy mergers and large-scale stellar bars), are one of the strongest form to act on the interstellar medium (ISM) and remove angular momentum through torques taking over preferentially on galactic scales, while the latters (e.g. turbulence in the ISM and spiral shocks), remove angular momentum through gas dynamical effects, taking over on smaller scales (inner kiloparsec). To the date, many Observations support the idea that large-scale bars funnel gas toward the center of galaxies (e.g. Mundell & Shone, 1999; Crenshaw et al., 2003; Sheth et al., 2005). Moreover, imaging has revealed that many structures are frequently observed in the inner kiloparsec of active galaxies such as inner disks (e.g. García-Burillo et al., 2003; Erwin, 2004; Krips et al., 2005; Smajić et al., 2015), rings (e.g. Pérez-Ramírez et al., 2000; Barbosa et al., 2006; Comerón et al., 2010;

Riffel et al., 2011), nuclear spiral arms (e.g. Martini et al., 2003; García-Burillo et al., 2005; Boone et al., 2007; Storchi-Bergmann et al., 2007; Schnorr-Müller et al., 2014a, 2017b) and nuclear bars (e.g. Colina & Wada, 2000; Martini et al., 2001; Erwin, 2004; Hunt et al., 2008) where the most common are the nuclear spirals, hosting in more than half of active galaxies and in all which are early-type ones (Martini et al., 2003). A strong correlation between the presence of nuclear dust structures and activity in galaxies has also been reported in Simões Lopes et al. (2007). This correlation, along with the frequency detected of dusty spirals, supports the hypothesis that nuclear spirals are one of the most important mechanism for fueling the SMBH, transporting gas from kiloparsec scales down to within a few tens of parsecs of the active nucleus. Numerical simulations as in Maciejewski (2004b) have reinforced the fact that nuclear spirals are good candidates to drive gas to fuel the AGN. These naturally form as a gas response to non-axisymmetry in the galactic potential and those generated by a strong bar take the form of shocks in gas instead of self-gravitating, triggering moderate gas inflow of ~0.03 $M_\odot$ yr^{-1}, enough to feeding local AGN, but if these are generated by a weak oval, they do not cause such inflows. Therefore, they concluded that inflows are likely triggered by spiral shocks and if this is not the case, inflows will not occur. However, in recent numerical simulations at high resolution in Kim & Elmegreen (2017) have postulated that even under a very-weak external potential, the mass inflow rates driven by nuclear spiral shocks are sufficient to power the observed level of AGN activity in diverse Seyfert galaxies. Hopkins & Quataert (2010) in their simulations, reinforced the presence of this feature at inner scales but they included also other morphologies as rings, clumps and nuclear bars, and showed that a cascade of subsequent gravitational instabilities from galactic scales of ~10 kpc down to 0.1 pc can generate a variety of morphologies as above and accretion rates around ~10 $M_\odot$ yr^{-1} for gas-rich systems, which is enough to fuel the most luminous quasars. These quasar-level inflows, arise from global perturbations such as galaxy mergers and large bars to then lie near to the radius of influence of the SMBH as a lopsided nuclear disk resulting in an accumulation of gas and the subsequent triggering of star formation.

Nevertheless, it seems that all these mechanisms involved are not entirely efficient for driving gas towards the nucleus. Theoretical studies and simulations (e.g. Emsellem et al., 2006) have shown how bars can efficiently promote gas inflow, but this seems to stall at an orbital resonance named as the Inner Lindblad Resonance (ILR), which is generally located within $\approx$ 1 kpc from the nucleus forming a circumnuclear ring where star

formation might be triggered (Pérez-Ramírez et al., 2000). On the other hand, several studies in nearby active galaxies that reveal the existence of nuclear spiral structures (e.g. Storchi-Bergmann et al., 2007; Riffel et al., 2008; Schnorr-Müller et al., 2014a,b, 2017a) have demonstrated that accretion rates are between 10^{-2}–10^{-4} $M_{\odot}$ yr^{-1}, corresponding to ∼2–3 orders of magnitude lower than inflow rates estimated. This suggests that most of the gas does not reach the nucleus, instead it accumulates a few hundred of parsecs from the nucleus, building a reservoir which can fuel the formation of new stars. The latter has been supported by observations of stellar intermediate-age (10^6–10^8 years) populations at low velocity dispersions in the inner kiloparsec regions (Barbosa et al., 2006; Riffel et al., 2010, 2011; Storchi-Bergmann et al., 2012). The low velocity dispersion indicates that these stars still keep the 'cold' kinematics of the gas from which they were formed.

In Sect. 3.3.7, this Thesis work will show an analysis of potential streaming inflow of cold molecular gas in the inner kiloparsec of NGC 1566 by modelling streaming inflows with a very simple toy model in which the inflow is assumed to have a constant radial inflow velocity (which we fix to 50 km s^{-1} after initial inspection of the results).

1.4.2 Feedback: Outflows

As was mention above,the energy released by an AGN, can have significant impact on the ISM and therefore, plays a participatory role in the host galaxy evolution. The latter process is known as AGN 'negative' feedback and can be in the form of radiation, winds or radio plasma jets. The result of this process is thought to prevent gas from cooling as inside as outside (intergalactic medium IGM) of galaxies affecting directly the star formation (quenching process), and to remove and/or redistribute gas by driving outflows. The feedback in turn, affects the fueling of the nuclear region so can regulate the SMBH growth. The overall picture about AGN feedback determines that there are two modes where these processes can operate (Fabian, 2012). These modes depend mostly on the type of the nuclear activity and are known as *the quasar mode* and *the jet mode*.

The quasar mode, also called *the radiative mode*, is mainly linked with AGN whose luminosity is close to the Eddington limit, $L_{EDD} \approx 33.000 \frac{M_{BH}}{M_{\odot}} [L_{\odot}]$, where M_{BH} is the mass of the Black Hole. This is characterized by energy mainly released by radiation or winds from the accretion disk, which drives gas outflows expelling gas from inner scales to galactic scales (e.g. Seyferts) to even the IGM (e.g. QSOs), leading a limitation on the mass than can be accumulated on the galaxy. On the other hand, the jet mode, also called

the kinetic mode, is considered to be dominant at lower luminosity AGN, with L_{Bol} <1–2% of L_{EDD} (Xie et al., 2017), corresponding typically to nearby massive galaxies like Ellipticals but also to low-luminosity Seyferts (Combes, 2015). This is characterized by a feedback ruled by radio jets which can prevents the gaseous environment from cooling back into the galaxy, keeping a balance between cooling and heating. The best evidence of this is found in cool core clusters of galaxies, where an AGN in the central galaxy of a cluster, moderates the cooling flow, through its radio jet, creating bubbles in the hot gas (e.g. Fabian, 2012, see their Fig. 4).

Outflows are mostly prevalent among powerful AGN such as young QSOs at high redshifts (Greene et al., 2012; Fabian, 2012; Lena et al., 2015), however, these can also play an important role in low-luminosity AGN ($L_{Bol}/L_{edd} \approx 10^{-6}$–$10^{-3}$) where the modest impact in comparison with high-luminosity AGN, is compensated by the abundance of such objects in the Universe (Combes, 2015; Rodríguez-Ardila et al., 2017) as well as their proximity in many of them. Studies in nearby Seyferts suggest that compact outflows (∼100 pc in extent) and velocities around ∼100 km s^{-1} with outflows rates of a few solar masses per year, are very common in low-luminosity AGN (Fabian, 2012) and a 60% of AGN, independently of their luminosity, host outflows (Ganguly & Brotherton, 2008). Thus, due to their abundance and proximity, most of studies in the context of feedback effects, have put their interests in nearby Seyferts with particular emphasis in the analysis of the inner kiloparsec of ionized gas and more recently in the new information provided by cold molecular gas (e.g. see in this Thesis work, Sect. 3.3.3). Some notes obtained with those gas tracers are as follows:

a) Outflows of ionized gas have been observed in optical and infrared (IF) lines and mostly by strong forbidden emission lines (e.g. [OIII] 5007å). These are been considerated as a *radiative mode* origin although, other mechanism are also observed (e.g. radio jets in galaxy 3C 293 according Mahony et al., 2016). Typically, the mass outflow rates of these are in the range 0.5–10$M_{\odot}$ yr^{-1} (Storchi-Bergmann, 2014) and the spatial extent can range to ∼ 10 kpc for AGN at redshift z∼0.1 (Sun et al., 2017), to just a few hundred of parsecs from the nucleus (100–500 pc) in nearby Seyferts (Barbosa et al., 2009; Storchi-Bergmann et al., 2010; Müller-Sánchez et al., 2011; Lena et al., 2015) they seem to have a non-preferred orientation, so the gas is transferred at random angles to the galaxy plane with velocities ranged between 200-1000 km s^{-1} and several ranges of open angles (Müller-Sánchez et al., 2011).

b) In recent years, the discovery of many massive molecular outflows as in atomic (HI) as in molecular (CO) gas, has given more support to AGN-driven outflows. The study of these cold components of gas at the present has been interesting by its uncertain origin (e.g. secular evolution, mergers, efficient cooling?) as well as its impact on the galaxy. Moreover, there are several studies evidencing that cold molecular gas is the most abundant component in outflows (Feruglio et al., 2010; García-Burillo et al., 2014; Cicone et al., 2014; Sakamoto et al., 2014), where they show a geometry rather arbitrary; molecular outflows are sometimes along the plane of the galaxy (e.g. IC 5063 in Morganti et al., 2015), as well as could be inclined by an angle (e.g. IRAS 17208 in García-Burillo et al., 2015). Furthermore, it is understood that molecular gas is the gas phase of which stars form, so molecular outflows must be directly affecting the star formation. A recent hypothesis to explain these outflows assumes that previous existing molecular clouds from the host ISM are pulled in the adiabatically expanding shocked wind and they can be accelerated to the observed velocities without being destroyed (Scannapieco, 2017). Additional ideas must be corroborated in the next years with the wide new possibilities provided by ALMA, since the mechanisms that can produce these outflows are still uncertain.

In Sect. 3.3.3, the present Thesis work, raises arguments on favor of a cold molecular outflow along the plane of the disk, particularly in the nearby seyfert galaxy NGC 1566. Several arguments are pointed out as well as it shows the main parameters involved in this fact.

1.4.3 Positive Feedback

The all mentioned negative feedback processes above is not necessarily an exclusive effect. There are evidences about *positive feedback* expected to occur in galaxies which means that feedback can also induce star formation (Maiolino et al., 2017; Cresci & Maiolino, 2018) through compression of molecular clouds in the galactic disk (Silk, 2013), as within the outflowing gas (Ishibashi & Fabian, 2012), which might explain the observed correlations between AGN luminosity and nuclear star forming regions. Therefore not only a negative effect in re-heating the cooling gas can occur, but also positive in allowing some further gas to cool.

1.5 Bars in Galaxies

Galaxies do not behave as a solid body structure. Themselves have shown that their rotating disks are wildly unstable, which could drive in the formation of grand design barred structures. To understand this, we have to be aware that the galaxy disks, where precisely the stars form and are hosted along with gaseous matter, were before rotating as a solid body. This means that stars were rotating on perfectly circular orbits and the relative velocities with respect to one star and another were zero (i.e. an observer from a star, will see that all stars are in rest). If the system is unstable, only a little perturbation in the medium will be enough to make little bit excess of density in some specific region of the disk. Thus, stars in the neighborhood of this little perturbation will be gravitationally influenced for this new higher-density region, so they will begin to fall towards this excess making it even more excessive. The unstable region is now more massive and so its gravity which allows to pull stars farther away and so to start to fall in to it as well. This process will be able to keep going until more material is falling towards the excess, making thus a structure known as bar. Once that a bar is formed, its non-axisymmetric gravitational potential induces in stars which are part of it to do not have circular orbits as at beginning, but they move on highly elongated orbits within the bar.

Therefore, in brief we can say that bars formed, as a direct consequence of the own gravity of galaxy disks: the heavier is the disk, more likely is that an unstable region originates, starting the above sequence mentioned for making a bar in a galaxy. Theoretical studies have pointed out that formation as well as destruction of bar are linked with the bulge and halo masses of the galaxy host. Concretely, Bournaud & Combes (2002) have shown that the bar evolution, depends on bulge and halo to disk masses ratios such that the bar can be dissolved to later be reformed, and previous studies as Norman et al. (1996); Sellwood & Debattista (1996) have emphasized that the halo have an impact in the bar dissolution although this is not a irrevocable issue but rather is part of cyclist changes of the galaxy.

Bars are efficient in the removal of gas angular momentum at different scales promoting gas cloud interactions. Their non-axisymmetric gravitational potentials produce torques that make gas lose angular momentum, leading to a gas transfer from galactic kpc scales down to parsec scales (Sellwood & Wilkinson, 1993). As the infalling gas accumulates in the galaxy center, bars can become unstable (Norman et al., 1996) until com-

pletely be destroyed (Shen & Sellwood, 2004). Consequently, bar fueling mechanisms are limited. García-Burillo et al. (2005) have pointed out that not all the gas reaches the central region, instead the gas has been found to concentrate in rings at inner Lindblad resonances (ILRs); a region where the star formation in galaxies is the great importance (Sheth et al., 2005). This ring seems to change the sign of the torques at this region, turning them positive and meaning that this material is not inflowing to feed the inner central region, but is flowing outwards. This implies that in strong barred galaxies, an AGN waits for the weakening of the bar. With this, the gas of the nuclear ring is liberated from positive torques to then form a disk through viscosity in the central region which could help to fuel the AGN (Combes, 2008). Thus, the proposed scenario is once the inner ring of star formation in the ILR is formed, and the bar has been weakened, the viscosity effects in the central region start to be important and smooth out the ring, bringing gas to the innermost part where it is under the gravitational influence of the SMBH to form a disk and feed the AGN. The process is cyclic so it is likely that the disk will be prone to a new bar if gas is accreted from the outer parts of the disk (e.g. mergers or the circumgalactic medium) and again, feeding process being affected. This clearly is suggesting that there exist a correlation between an AGN activity with a weak bar phase (Combes, 2008).

In the present Thesis, Sect. 3.3.6, it is considered the possibility that the large-scale bar in NGC 1566 is producing nuclear velocity deviations from normal rotation in the inner ∼100 pc from the nucleus in cold molecular gas (CO J:2-1). There is observational evidence about ALMA that cold molecular gas is outflowing from the nucleus, the concern that raises is if this is a nuclear outflow by the AGN, or is based in streaming motions, induced by gravitational torques of the large-scale bar, as was pointed out in previous studies (Combes et al., 2014; Smajić et al., 2015). This work argues in favor of a nuclear outflow by the AGN.

1.6 Seyfert Galaxies

Seyferts in the nearby Universe constitute the main objects to study in this Thesis work. Therefore, it is important to include a section entirely dedicated to them but dedicated exclusively to their types and main spectra features (some features and components in previous sections 1.2 and 1.3).

Seyfert galaxies are named after Carl Seyfert, who observed a sample of galaxies by

using optical spectroscopy in 1943. He found that several of these galaxies show high surface brightness nuclei, strong high excitation nuclear emission lines and that some Balmer lines are sometimes broader than others (Seyfert, 1943). These possess a quasar-like nucleus, but the host galaxy is clearly detected due to their lower luminosity. For distinguishing Seyferts from Quasars more clearly, the current accepted criterion is that the former are active galaxies with lower luminosity nuclei with an absolute B-band magnitude MB $> -21.51 + 5 \log h_0$[3] (Schmidt & Green, 1983). Seyferts are now identified spectroscopically by the presence of strong, high ionization emission lines. Morphological studies indicate that most if not all Seyferts occur in spiral galaxies and are frequently strongly perturbed and/or gravitationally interacting with others. Nevertheless, a relatively low percentage of spiral galaxies host Seyfert nuclei.

Khachikian & Weedman (1974) were the first to realize that there are two distinct subclasses of Seyfert galaxies according their spectroscopic features: Type-1 and Type-2. Their main difference is the appearance or non-appearance of broad permitted lines in the nuclear spectrum. In Type-1 Seyferts for example, permitted emission lines as Hα (6562.8Å) can possess a Full Width at Half Maximum (FWHM) > 1000 km s^{-1} and similar to others lines. The region where these lines come from is known as the *broad line region* (*BLR*). It is formed by dense photoionized clouds (electron density $n_e > 10^{10}$ cm^{-3}) such that, the forbidden emission lines are suppressed by collisional processes, implying that broad components appear only in permitted lines. Similarly, narrow emission lines comes from a region known as the *narrow line region* (NLR). This region has a lower density ($n_e \sim 10^3$–10^6 cm^{-3}) than the BLR and therefore, these can emit permitted and forbidden lines. The NLR is optically thinner and further from the nucleus than the BLR.

For Type-2 Seyferts, only narrow components are observed (both permitted and forbidden lines). Generally, these are lower luminous in X-ray band ($L_X < 10^{42}$ $ergs$ s^{-1} in Singh et al., 2011) and have a weaker continuum than their counterpart (Type-1) which allows the observation of absorption lines related to the stellar component of the host galaxy. Sometimes type-2 Seyferts are intrinsically type-1 (almost face-on to the *LOS*) but these can suffer obscuration on the BLR along the *LOS* and so do not show the characteristic broad lines of type-1 Seyferts.

Despite of that, this is the classification that most prevails, some authors as Osterbrock (1981) take into account a most detailed classification, including the 1.5, 1.8 and 1.9

[3]the factor $h_0 = H_0/100$, where H_0 is the Hubble constant.

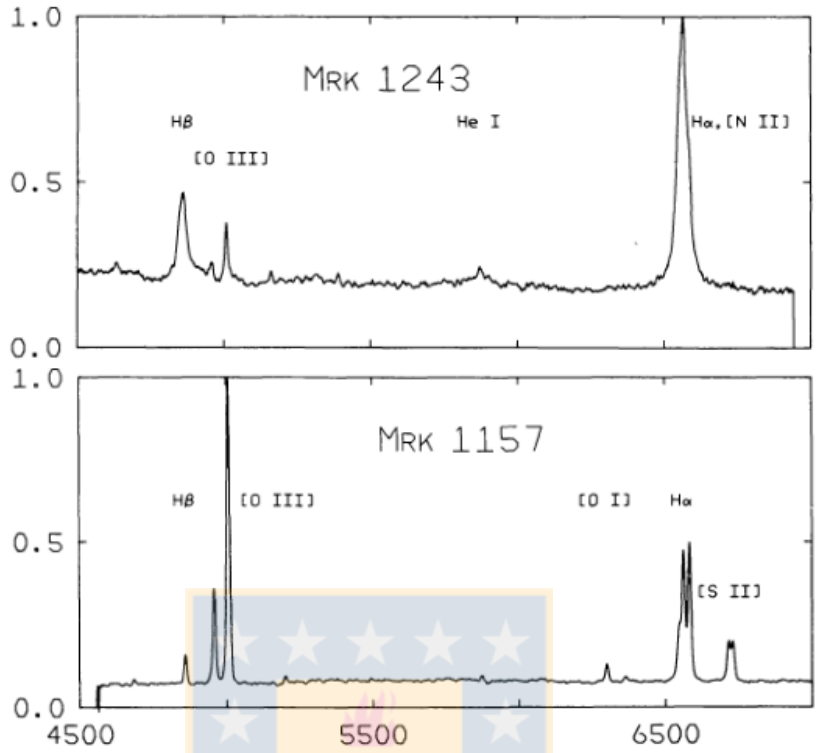

Figure 1.4 Optical spectra of Seyferts. Spectra for both type-1 (top panel) and type-2 (bottom panel) Seyferts. The y-axis indicates the relative energy flux in flux units per wavelength interval, while x-axis shows an optical wavelength range for these galaxies in angstroms units. Source: Osterbrock (1984).

notation to point Seyferts whose spectra present both narrow emission lines combined with broad Hα and Hβ components, namely, an intermediate classes between type-1 and type-2 whose typification depends of how much close is the spectrum from a type-1 or a type-2, putting the attention in the Balmer emission lines (Hα and Hβ).

In Fig. 1.4, is shown two spectra for Seyferts. Note how emission lines for the type-1 (MRK 1243) are broader than its type-2 counterpart (MRK 1157). This difference is normally appreciated in permitted lines (e.g. Hβ) whereas in forbidden lines, it is not obvious (e.g. [OIII]). The emission lines in type-1 Seyferts can be so broad, that they can even overlap until they hide the narrow lines (e.g. see Hα with [NII]in top panel of Fig. 1.4). We can also note in these galaxies how the power-law continuum in the optical is greater in the type-1 in comparison to the type-2, which is another of the main characteristic to distinguish them.

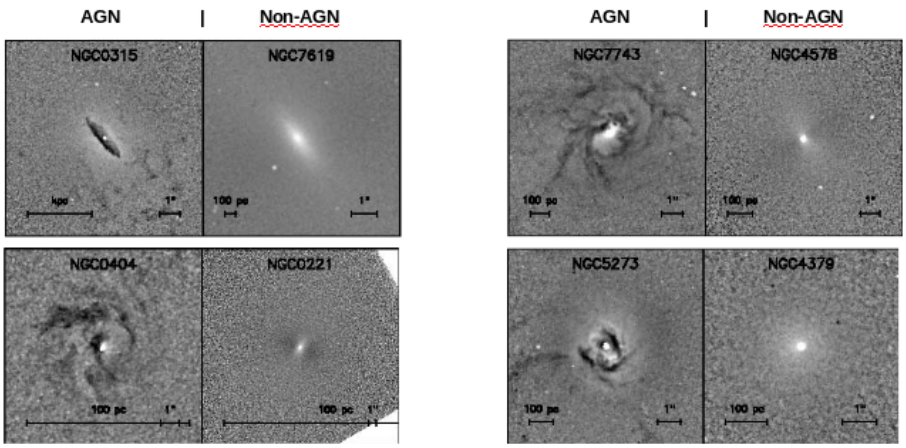

Figure 1.5 Dusty nuclear spirals in galaxies. Structure maps in the inner kiloparsec for active and non-active early-type galaxies. Each galaxy pair has the active galaxy on the left and the inactive galaxy control sample on the right. Source: Simões Lopes et al. (2007).

1.7 Motivation and this Work

As mentioned above, Seyfert galaxies, are spiral galaxies hosting an AGN. In the context of active galaxies, they are the most abundant in the nearby Universe, which added to its lower luminosity, allows the host galaxy to be clearly detected, so they become the ideal sources for mapping and quantifying the kinematical processes that are participating in the inflowing/outflowing of matter from galactic scales to nuclear scales and so, to advance in the understanding of how the mass is transferred from galactic scales down to nuclear scales to feed the SMBH.

To the date, many studies have shown theoretically that asymmetries in the gravitational potential efficiently promote gas inflow towards the inner regions of the galaxies (Emsellem et al., 2003; Englmaier & Shlosman, 2004; Hopkins & Quataert, 2011; Emsellem et al., 2015) and it has also been observationally confirmed as outer as inner scales (Mundell & Shone, 1999; Combes, 2003; Haan et al., 2009; Combes et al., 2014; Querejeta et al., 2016, among others). Projects as the *NUclei of GAlaxies* (NUGA), which studied the molecular gas kinematics at arcsecond scale resolution in 12 nearby weakly active galaxies, have found a large range of nuclear gas morphologies including lopsided disks, bars, (one and two-arm) spirals, rings and in some of them, gas streaming motions towards the nucleus (García-Burillo et al., 2003; Casasola et al., 2008; Hunt et al., 2008; Haan et al., 2009; van der Laan et al., 2011, among others). Among these morphologies,

the most common has been nuclear dusty spirals. Martini et al. (2003) found that nuclear dusty spirals, occur with comparable frequency in both active and non-active galaxies and that the only difference is that none of the AGN lack this structure. Consequently, in a similar study, Simões Lopes et al. (2007) analyzed images of 34 active and 34 non-active (as a control sample for each active galaxy), lenticular and elliptical galaxies. They reported a strong correlation between the presence of nuclear dust structures (filaments, spirals and disks) and activity related with matter accretion in these galaxies: a presence of 100% of these in AGN and around 26% for non-active galaxies. In Fig. 1.5 is shown some examples about the pair comparisons related to that study where it is possible to appreciate the clear morphological differences (nuclear dusty structure) between active and non-active galaxies. All these signs, support the idea that dusty nuclear spirals are likely associated to shocks and angular momentum dissipation, a scenario which has been also theoretically supported (e.g. Elmegreen et al., 2002; Maciejewski, 2004a,b), therefore it might be an important mechanism for fueling the nuclear SMBH, transporting gas from kiloparsec scales down to a few tens of parsecs of the active nucleus. The latter has been recently confirmed in several studies based in Integral Field Units (IFU) observations as Riffel et al. (2008); Barbosa et al. (2009); Storchi-Bergmann et al. (2010); Riffel et al. (2013); Diniz et al. (2015); Lena et al. (2015); Schnorr-Müller et al. (2014a, 2017b,a), among others. All these observations have revealed streaming motions of gas towards the nucleus along dusty spiral arms observed in *HST* images. In Fig. 1.6 is shown maps for two nearby active galaxies related to the above studies. In NGC 2110 (top panels), the largest blueshifts in the velocity map, mainly observed in the near side of the galaxy, are cospatial to dust lanes whereas for NGC 1667 (bottom panels), the dust lanes are observed cospatially to the spiral pattern in the residual map. Considering in both examples that the gas is in the plane of the disk, blueshifted residuals on the far side of the galaxy and redshifted residuals on the near side imply we are observing radial inflow to the nucleus. Despite of clear evidences for gas streaming motions, the calculated mass flow rates in the ionized and hot molecular gas (T$\approx$ 2000K) is nevertheless of the order of 10^{-4}–10^{-5} $M_{\odot}$ yr^{-1} which is considerate small to feed significantly an active nucleus, implying that these phases are only tracers of a much larger flow of cold molecular gas. ALMA give us the possibility to map these flows with a necessary spatial resolution to reveal the presence of streaming motions at the scales they are observed in the optical and near-IR.

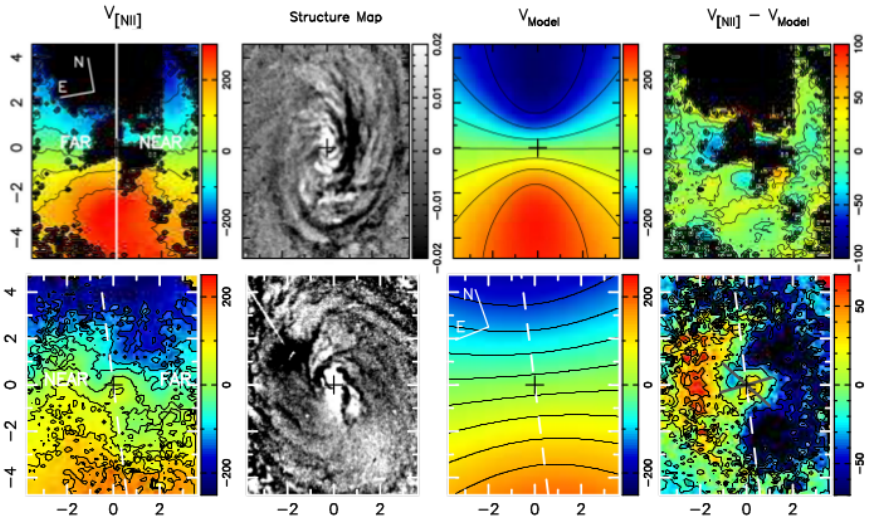

Figure 1.6 GMOS maps for NGC 2110 and NGC 1667. The maps show the centroid velocities, structure maps highlighting the nuclear dust spirals, modelled velocity fields and residuals for Seyfert galaxies NGC 2110 (top panels) and NGC 1667 (bottom panels). Source: Schnorr-Müller et al. (2014b, 2017a).

Now that IFU studies of the central kiloparsec (~5″) have completed for a wide sample of nearby Seyfert galaxies having dusty nuclear structures and finding signatures of streaming motions along these nuclear spirals in many of them, This work put the interest in the observation of cold molecular gas of 5 nearby Seyfert galaxies selected for: (1) showing signature of inflows in our previous IFU observations; (2) having previous detection of CO emission with smaller arrays; (3) being close enough to resolve structures at scales of tens of parsecs (e.g. see structure maps in Fig. 1.6).

Thus, our primary goal consist in to obtain the spatial distribution and kinematics of the cold molecular gas within the inner kiloparsec of 5 nearby seyfert galaxies previously well studied in optical IFU observations, in order to map the molecular gas mass distribution and obtain the overall kinematics involved as well as the mass flow rates along the nuclear spirals. For this project, we have applied for ALMA cycle-1 in 2012 and got the data during mid and the end of 2014, with an improved spatial resolution and sensitivity relative to previous observations in the past. It was used molecular gas kinematics less than 50 pc of resolution (CO J:2-1 with ALMA) within the inner kiloparsec in our sample selected as for showing inflows of ~50 km s^{-1} along dusty nuclear spirals in previous optical IFU observations as for being close enough to resolve structures at scales of

tens of parsecs. Once mapped the molecular gas mass distribution and obtain the overall kinematics for each galaxy from our ALMA data, we will be in position to study the spiral structures, and in particular, the mass flow rates along the nuclear spirals and try to demonstrate the agreement with studies in the optical part which says that spiral structures are the feeding channels of the SMBH for accretion and therefore, the key mechanism for a nuclear activity in galaxies.

This Thesis work is organized as follows. Chapter 2 presents the sets of observational data and kinematical methods used; Chapter 3 shows an extended morphological and kinematical analysis, by applying the methodologies proposed in the previous Chapter, of the ionized and cold molecular gas in the inner kiloparsec for NGC 1566; the best well-detected galaxy of our sample. And finally, Chapter 4 highlights the general conclusions along with some future prospectives according this work.

2

Observing and Analysis Methods

2.1 ALMA and Observing cycles

The *Atacama Large Millimeter/Sub-millimeter Array* (ALMA) is an aperture synthesis telescope currently consisting of 66 antennas that can be used in a number of different configurations and operating over a broad range of observing frequencies in the millimeter and submillimeter of the electromagnetic spectrum (from 84 GHz to ending at ~950 GHz). It consists of primary set of fifty antennas of 12 meters in diameter with baselines up to 16 km, along with an additional and more compact set of twelve antennas of 7 meters in diameter with other four antennas of 12 meters, all of them, located on the Chajnantor plateau (Antofagasta region, Chile), at more than 5000 meters in altitude. ALMA was constructed and is operated by an international collaboration including Europe (represented by the European Southern Observatory), North America (represented by the National Radio Astronomy Observatory), East Asia (represented by the National Astronomical Observatory of Japan) and the cooperation of Chile. Up to now, is still considerated the most powerful land observatory of the history.

Within their main science goals are[1]:

- The ability to detect spectral line emission from CO or [CII] in a normal galaxy like the Milky Way at a redshift of z=3, in less than 24 hours,
- The ability to image the gas kinematics in protostars and in protoplanetary disks around young Sun-like stars in the nearest molecular clouds (150 pc),

[1]https://almascience.eso.org/about-alma/alma-basics

- The ability to provide precise high dynamic range images at an angular resolution of 0.1 arcsec.

For all above, ALMA becomes in the ideal instrument to image the nuclear cold molecular gas distribution in the central kiloparsec at improved spatial resolution and sensitivity, and therefore the subsequent development of this Thesis.

This work is based in ALMA cycle-1 and cycle-2 observations; all our sources were approved for cycle-1 but observed during cycle-2. It was proposed in early 2013; accepted in mid-2013 and finally observed between mid-2014 and mid-2015 (cycle-2:project-ID 2012.1.00474.S; PI: Nagar). The data started the arriving during end of 2014 (delayed). Cycles 1 and 2 are the second and third 'Early science' periods that were available to the international community. After this, ALMA started the science period with the completion of 66 antennas and so, with their full capabilities. Below a summary of the ALMA capabilities that were available for the observations of our sample:

- Thirty two 12-meter antennas in average (34 in cycle-2).
- Band 6 receivers (211-275 GHz) for detection of cold molecular gas emission line CO J:2-1 ($\nu_{\rm obs}$ = 229.401922 GHz) as priority; 13CH3OH ($\nu_{\rm obs}$ = 241.548041 GHz) and CS(J:5-4) ($\nu_{\rm obs}$ = 243.728532 GHz) in a few cases.
- Baseline ranges between 160 mts. to ~650 mts. (1 km maximum for ALMA cycle-1 and 1.5 km for cycle-2).
- 0.5″ of angular resolution (0.25″ maximum for cycle-1).
- 4 spectral windows in Band 6 (two in the lower sideband and two in the upper sideband), each with a width of 1.875 GHz (after discarding edge channels) with a total velocity coverage (for CO J:2-1) of ~2464 km s^{-1}.
- Lines covered with a relatively high spectral resolution of ~ 1.3 km s^{-1}).

The flux and the phase calibrators used for every source along with the total observing time and the beam size is listed in Table 2.1. Data were calibrated and imaged using mainly CASA 4.7.0 (McMullin et al., 2007). The CO J:2-1 emission line was strongly detected over a velocity range of ~ ±200 km s^{-1}, and we were able to map the CO line at the intrinsic (observed) velocity resolution of 1.3 km s^{-1}.

Table 2.1 Observing Parameters in the sample. Source: Ramakrishnan et al. (2018).

Sources	Date of observation	Flux calibrator	Bandpass / Phase calibrator	Total observing time (min)	FWHM (″× ″) (°)	rms (mJy km s^{-1})
NGC 1566	2014 Jun 29	J0519-4546	J0519-4546	65.4	0.56 × 0.43 (14)	1.1
NGC 1386	2014 May 27	Neptune	J2357-5311 / J0334-4008	39.0	0.80 × 0.54 (85)	0.8
NGC 1667	2014 Jul 08	J0423-013	J0423-0120	45.4	0.55 × 0.51 (66)	0.7
NGC 2110	2015 May 14	Ganymede	J0423-0120 / J0541-0541	45.0	0.99 × 0.56 (-69)	0.9
NGC 7213	2014 May 27	Neptune	J2056-4714 / J2235-4835	44.0	0.62 × 0.57 (81)	0.8

2.2 Data Sample

This sample consist in 5 nearby Seyfert galaxies which can briefly be described as follows:

NGC 1566 is a near Seyfert 1 galaxy sometimes classified as 1.5 due to its variability nature. It is the brightest member of the Dorado group showing clear spiral patterns associated with strong HII regions and a prominent large-scale bar (although the shape weakly defined) easily detected in optical and infrared (more details about this source in Sect. 3.1).

NGC 1386 is a Seyfert 2 galaxy with extended [OIII] and radio emission (Weaver et al., 1991; Storchi-Bergmann et al., 1996). The direction of the extended [OIII] emission is similar to the extended radio emission detected by Nagar et al. (1999).

NGC 1667 is a low-luminosity Seyfert 2 galaxy (Ho et al., 1997b). The contribution in the UV, Hα and radio is very minimal by the AGN. Less than 1% of the UV emission originates from the nucleus of this galaxy (inner 2”), where the emission may in part be due to nuclear radiation scattered in our direction, or to circumnuclear star formation. Most of the emission in this band comes from star-forming regions along the spiral arms of the galaxy. The Hα emission is significantly stronger at the nucleus. It also shows emission from the star-forming regions along the spiral arms.

NGC 2110 is a well-known Seyfert 2 active galactic nucleus (Pfefferkorn et al., 2001). Strong emission lines are seen, with a large spatial extension beyond the continuum. Strong rotation is seen with an off-centre peaked velocity dispersion profile.

NGC 7213 is a Seyfert 1 AGN with a very bright nuclear point source embedded in a circular bulge. The disk is very faint and featureless. The [OIII] emission of this galaxy has a halo-like morphology, homogeneously distributed around the nucleus, with a diameter of 1″ (130 pc). The radio emission is unresolved (Schmitt et al., 2001). The kinematics and the chemical abundance of the gas in this galaxy was studied byStorchi-Bergmann et al. (1996).

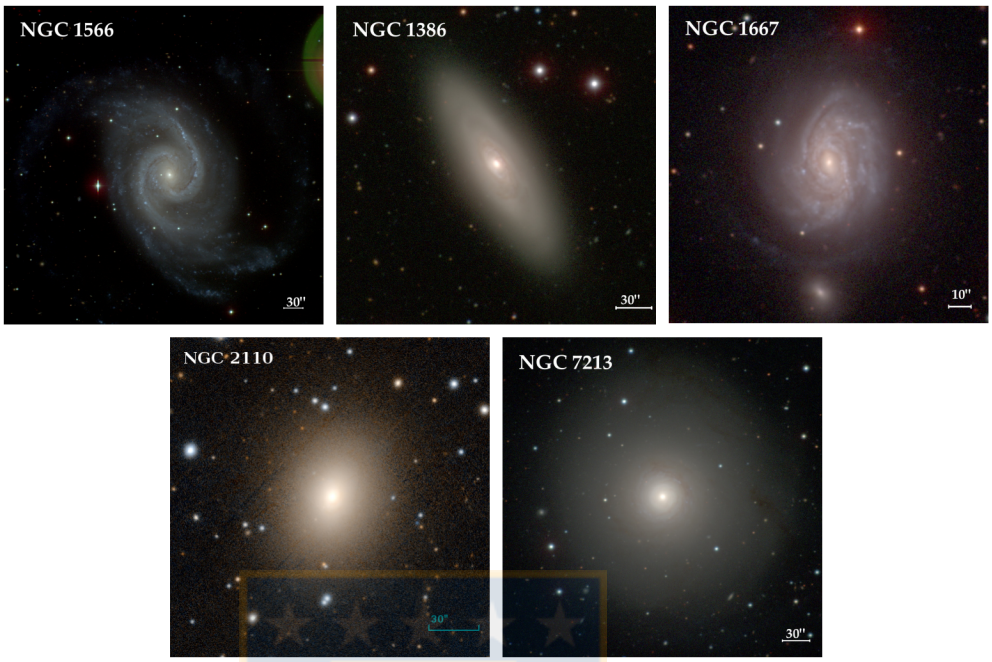

Figure 2.1 Reference images of each source of our sample. Source: *The Carnegie-Irvine Galaxy Survey* (CGS) and *Pan-STARRS* (NGC 2110).

These galaxies were observed using ALMA with particular interest in tracing the CO J:2-1 emission at inner kpc and were selected according previous studies by: showing signatures of inflows and nuclear outflows mainly in optical and infrared observations; having previous detection of CO emission with at lower resolution and being close enough to resolve the morphology in the central kpc. The source list along with their default parameters are given in Table 2.2 whereas wide field images for each source from optical are shown in Fig. 2.1.

A strong nuclear continuum was detected in all sources except NGC 1667. Therefore, it was necessary to subtract the continuum from the spectral windows to detect any molecular line emission in the *uv*-plane distinctly. Following this procedure, the CO J:2-1 spectral line of every source was imaged using a natural weighting at a spectral resolution of 1.3 km s^{-1}, although according our special treatment to NGC 1566, which was strongly detected, here we have also taken in count the uniform weighting to then analyze maps with the highest spatial resolution as possible (see more details in Sect. 3.2). To improve the dynamic range of the final spectral cube, both amplitude and phase self-calibration solutions that were obtained from the continuum was implemented on the spectral cube.

Table 2.2 List of sources. Source position and distance are according to those cited in the NED webpage. The luminosity distance and scale was estimated according to the assumption a flat cosmology with $H_0 = 75$, $\Omega_M = 0.3$ and $\Omega_\Lambda = 0.7$. The position angle (P.A.) and the inclination (i) are of those from the 2MASS catalogue, with the exception of NGC 1566 which were estimated according to a part of the analysis detailed in Chapt. 3. Source: Ramakrishnan et al. (2018).

Sources	Morphology	Nucleus type	R.A.	Dec	z	D_L (Mpc)	Scale (pc arcsec^{-1})	P.A. (°)	i (°)
NGC 1566	SAB(s)bc	Sy1	04:20:00.42	-54:56:16.1	0.005017	10.0	48	45	33
NGC 1386	Sa	Sy2	03:36:46.18	-35:59:57.87	0.002895	11.6	55	25	68.90
NGC 1667	Sc	Sy2	04:48:37.14	-06:19:11.88	0.015167	61.3	297	165	38.74
NGC 2110	S0	Sy2	05:52:11.38	-07:27:22.36	0.007789	31.3	152	165	34.91
NGC 7213	SA(s)	Sy1	22:09:16.31	-47:09:59.80	0.005839	23.4	113	70	19.95

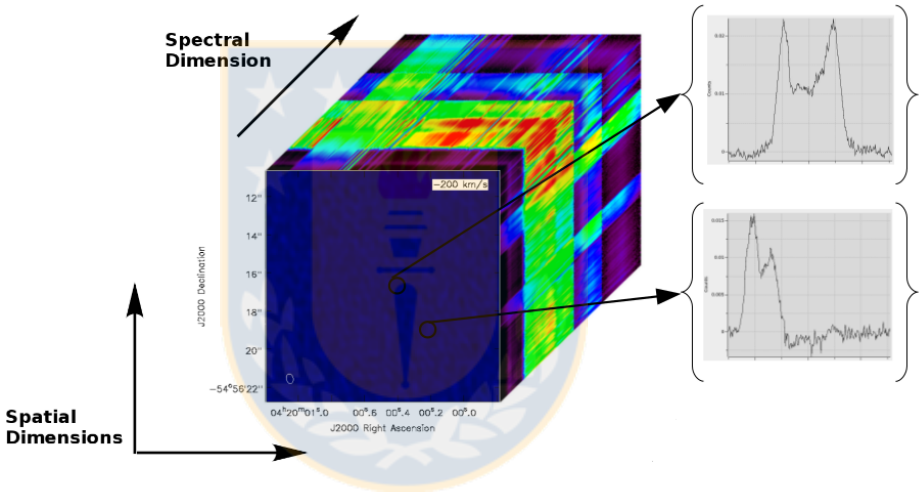

Figure 2.2 Schematic representation of a data cube. On the right hand is included an illustrative example of how line profiles are obtained. Source: Own elaboration.

2.3 Methods for a kinematic analysis

2.3.1 Moment Maps

After calibration and imaging of the data observations, we are able to map all channels in the data set to obtain a spectral line 3D data cube (RA, Dec, Velocity). In Fig. 2.2 this data set is schematized. The data cube obtained above is a series of images stacked along a spectral dimension normally represented by the velocity. In order to facilitate further interpretation, it is useful to create 1-2 Dimension maps (1-D, 2-D) through a linear combination of individual planes, which provide different ways to analyze the data

observations as: a) line profiles (1-D along spectral dimension), b) channel maps and movies (2-D slices along velocity axis), c) moment maps and (integration along the velocity axis) and d) Position-velocity diagrams (slices along spatial dimension. See later Sect. 2.3.3). Line profiles are useful for showing changes in line shape, width and depth in different portions of a source. Fig. 2.2 illustrates this example by taking spectra from specific locations above the data cube through apertures of one pixel size, however it is also possible to create a line profile of the entire data cube, first extracting each spectrum in the pixels as above, to then make an overlay in all of them along the relative axis of the velocity(the spectral dimension). Channel maps as well as channel movies, show how the spatial distribution of the line emission changes with velocity. These normally are represented as a map array with several images of the source at specific velocity values (channel maps) or by consecutive series of channel images gradually changing (movies). In this work, we generate three of such maps, specifically moment maps (in Chapt. 3 we will also take in count a fourth one: the skewness map), with each dependent on the sum (integrated intensity, M_0), average (integrated velocity, M_1) and the standard deviation (velocity dispersion, M_2) along the velocity (or frequency) dimension. The equations to generate the respective maps and are given in top panels of Fig. 2.3. The maps are computed with a threshold that defines the pixel values to be included. For all the sources shown in this section, we generated moment maps assuming a threshold of 4σ with the noise level shown in Table 2.1. The number of channels chosen to stack the maps varied from 250 to 600. (for NGC 1566, see Sect. 3.3.1)

The moment maps for all sources are shown in the Figures 2.4. We can immediately realize the importance of these maps for a morphological and kinematic first view and interpretation for the sources. All sources share important features like a markedly spiral morphology (except NGC 2110 which is not obvious with a more disky feature) and higher flux intensities in their centers, supported by higher velocity dispersions in the same scale; a typical feature of active galaxies. NGC 1667 contains two such regions within the inner $\sim 2''$ of the nucleus that are posited distinctly opposite to one another. Interestingly, have a peculiar nuclear morphology as can be inferred from the moment 0 map. The inner region shows to be clearly decoupled with the large spiral arms, in fact there is a clear sign that this galaxy suffers a change of position angle of the major axis in the inner $5''$ to around $150°$; a classical effect reported in barred galaxies at lower radii of the ILR. All the Velocity maps seem to show a clear velocity gradient with an indication

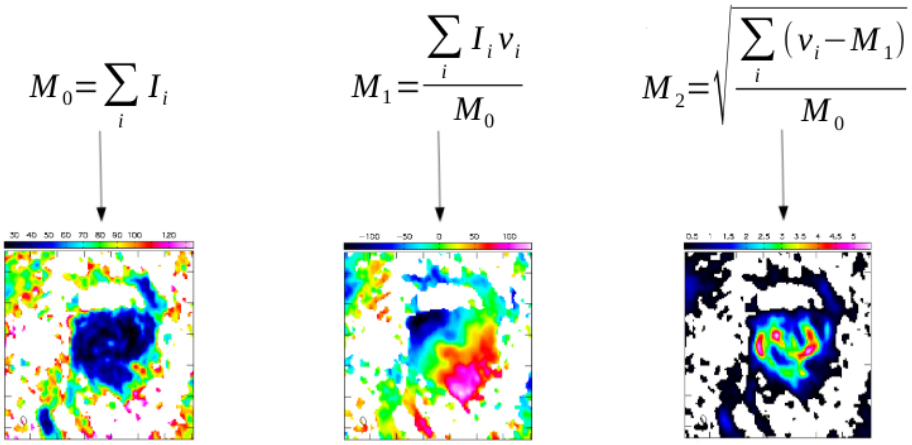

Figure 2.3 Schematic view for moment equations and their corresponding maps. Top panels show each equation relative to create the flux (bottom left), velocity (middle) and velocity dispersion. Source: Own elaboration.

of a rotating component.

2.3.2 Residual Maps

Analyzing residual maps could be an efficient tool to identify deviations components from a normal axis-symmetric rotation velocity. These potential deviations could be interpreted as inflows or outflows from the source and thus, giving the possibility to measure important quantities which allow us to advance in the understanding of the gas kinematics in a respective source. A disadvantage lies in the fact that residual maps are the result of a velocity model extraction from the velocity map, which shows the intensity weighted average velocity of the spectrum corresponding to each spatial pixel. Therefore, these deviations must be strong enough in comparison to normal rotation components to be appreciated and so being separated from normal rotation components. Unfortunately this is not always the case which forces the searching of other methods to analyze potential non-circular velocities more properly (for alternative methods, see Sect. 3.3.7).

In these sources, as a demonstration to obtain residual maps, we can model the velocity map of all galaxies by assuming circular orbits in a spherical potential, for example as

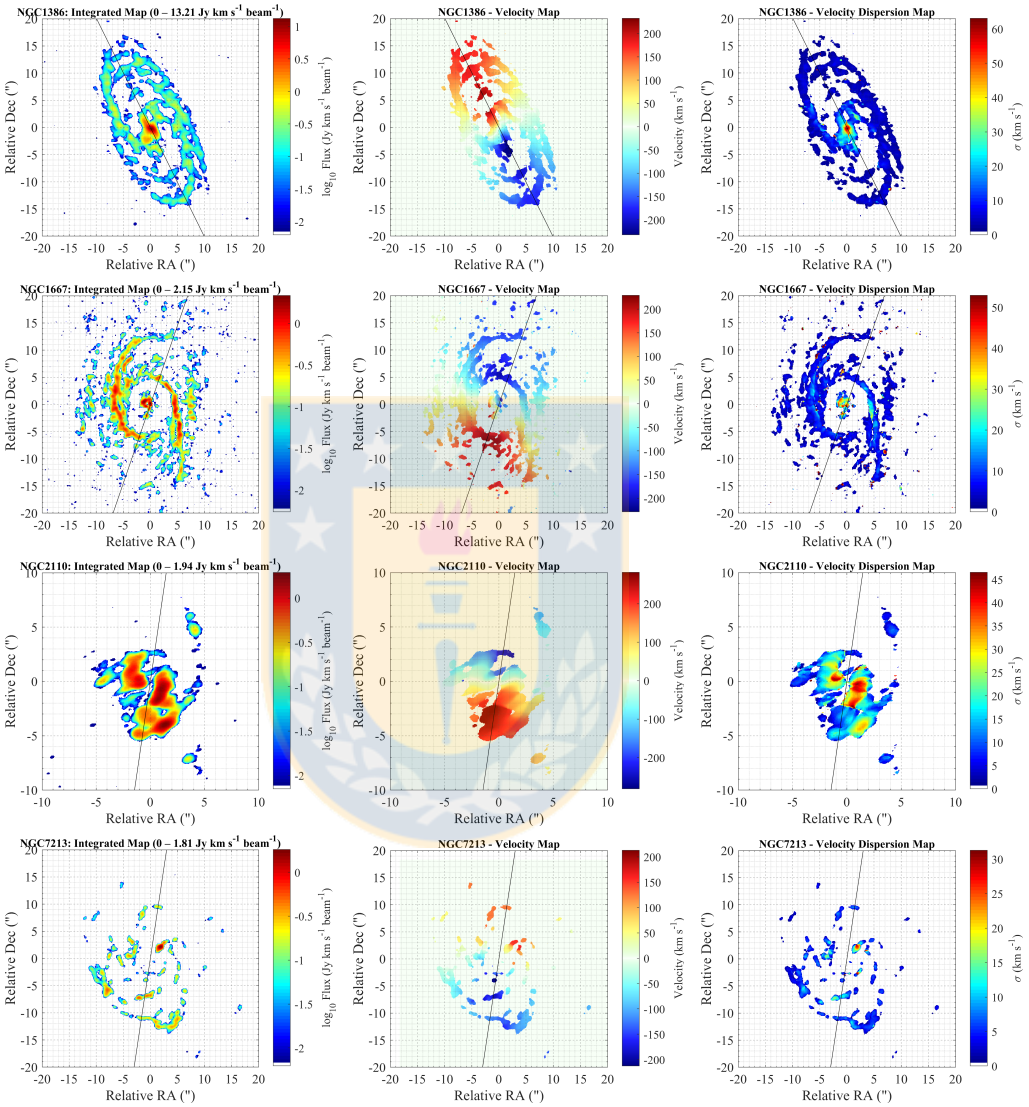

Figure 2.4 Moment maps for each source. From left to right, integrated flux, velocity field and velocity dispersion. Solid lines are the kinematic major axis estimated. (For ALMA and GMOS observations in NGC 1566, see Figs. 3.2 and 3.3, respectively). Source: Ramakrishnan et al. (2018).

given in Bertola et al. (1991):

$$V_{\rm mod}(R,\psi) = V_{\rm sys} + \frac{AR\cos(\psi-\psi_0)\sin(\theta)\cos^p(\theta)}{\{R^2[\sin^2(\psi-\psi_0)+\cos^2\theta\cos^2(\psi-\psi_0)]+c_0^2\cos^2\theta\}^{p/2}} \tag{2.1}$$

Here, $v_{\rm sys}$ is the systemic velocity, A the amplitude of the rotation curve, R and ψ are the radial and angular coordinates for a given pixel in the plane of the sky, ψ_0 is the position angle of the line of nodes and θ is the inclination of the disk. The parameter p denotes the mass distribution of the galaxy such that for a $p = 1$ the rotation curve is asymptotically flat while enclosing the total mass of the system for a $p = 1.5$. The concentration parameter c_0 corresponds to the radius at which the velocity reaches 70% of the amplitude.

In order to obtain an interpretation of the gas velocity field, we fit the equation 2.1 to the velocity map as obtained in section 2.3.1. The model fitting was done using an optimization routine (Ramakrishnan et al., 2018) allowing all six parameters of the model to vary with the only tighter constraint on p in the range $1.0 - 1.5$. Apart from the given parameters, we also attempted to find the best-fitting centre coordinate (x_0, y_0) of the model (for more details, see Ramakrishnan et al., 2018).

Thus, by modelling the kinematics of all the galaxies we are able to construct a model map for each one, which we can use to subtract on each velocity map and then to obtain residual velocities which as we mentioned above, are the maps which help us to determine potential non-axisymmetric components that have an important effect inside the overall gas kinematics. In Fig. 2.5 is shown all the respective residuals for each galaxy, associated also to the velocity field and velocity model used to create them. Some quick statements according these maps are: NGC 1667 shows important non circular components in its residual map, however it seems to be an important difference between the major axis estimated by the model (solid line) with respect to the true major axis of this galaxy (by eye, tracing an imaginary line between the red-shifted and blue-shifted maximum values in the velocity map). This could be the real fact of the strong deviations detected in the inner 5″ and not necessarily related to non-circular components. On the other hand, the major axis of the model in NGC 1386 seems to agree very well such as in NGC 2110. Residual map of NGC 1386 shows a good subtraction along the arms a greater scales and reveals important non circular components in the inner region that might be indications of outflowing

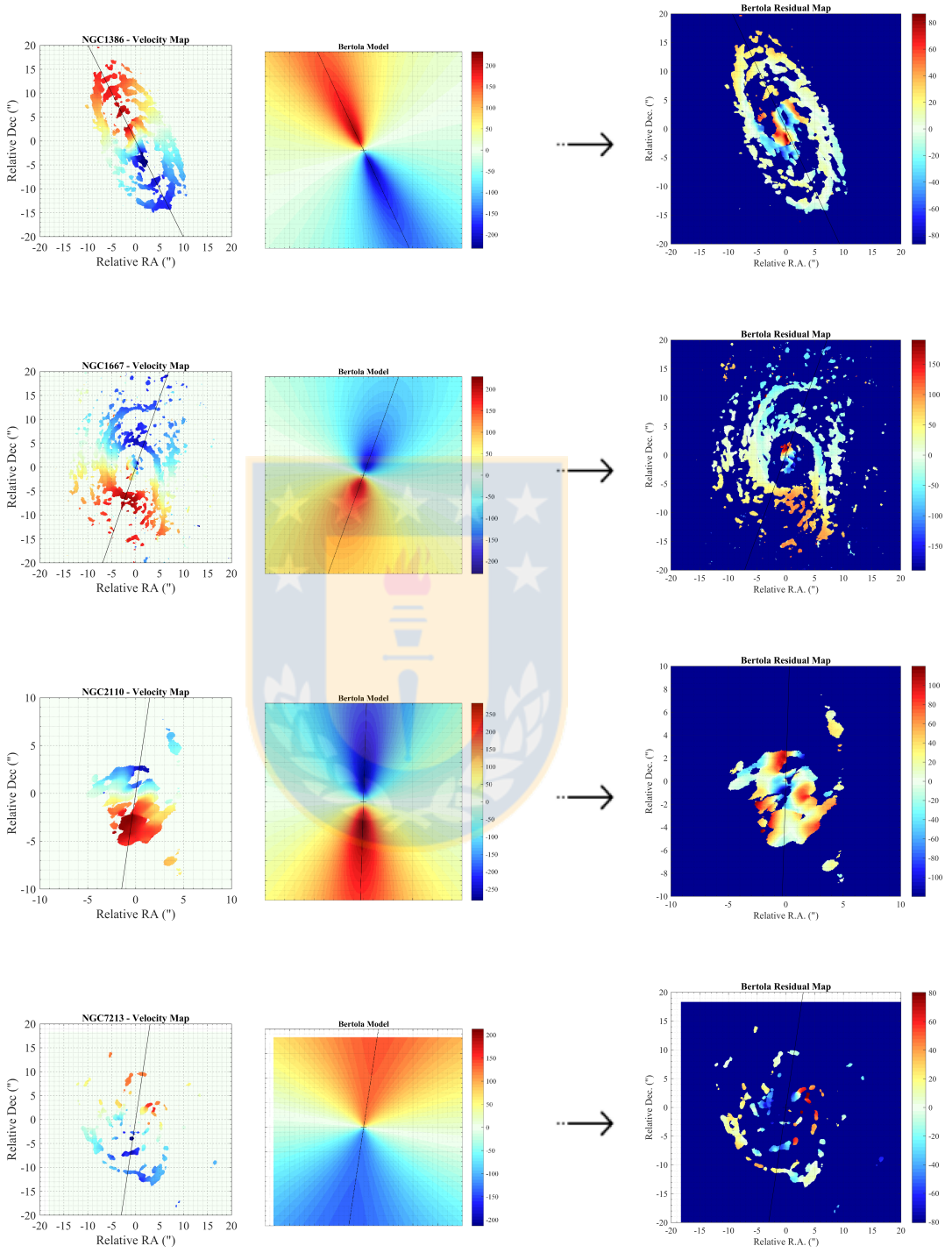

Figure 2.5 Residual extraction for each source. On the left hand and smaller, maps of the velocity field (most left) and the respective velocity model according the equation 2.1 with same velocity ranges, while in the right hand and greater to highlight, the corresponding residual maps after a subtraction of the models in the velocity fields (V_{field} -V_{model}). Velocity map, velocity model and also the residual map, have the same spatial scales. Solid lines are the major axis estimated for each galaxy. Source: Ramakrishnan et al. (2018).

gas according its orientation (near side to the northwest and far side to the southeast). Lena et al. (2015) reported a biconical nuclear outflow of ionized gas which seems to matches interestingly with the non-circular components shown here, which makes to this source a strong candidate for a deeper kinematic analysis in the near future. In NGC 2110, the residual shows a disturb morphology with important regions over-subtracted by the model in the north side and a possible scenario of inflows in the inner 2″, taking in count its orientation (near side to the west, far side to the east with a red-shifted and blue-shifted components, respectively). There are important evidence in optical studies that this source was a scenario of a recent minor merger in the inner 5″ south to the nucleus, which could explain in part its disturbed feature (González Delgado et al., 2002). NGC 7213 also reveals some perturbations in the inner 5″, however is difficult to invoke an interpretation due to the poor data in the velocity field.

In general, all sources have demonstrated to get significant components in the residual maps meaning that there hare strong potentials non-circular components linked with streaming inflows or nuclear AGN/starburst outflows. However and as we can directly see, residual maps can show us deviations from velocity maps but this require a deeper analysis to truly conclude if these features are in fact, important components, or is just noise driven by bad-fitting velocity models among others issues.

In Sect. 3.3.2 it is shown a more detailed analysis for moment maps and their interpretation with respect to our special source NGC 1566. It is specifically argued that residual maps are an important method for the analysis but not enough to disentangle non-circular components in whole.

2.3.3 Position-Velocity diagrams

Position-Velocity (pv) diagrams represent another mechanism for the analysis of line cubes and a complement for those based in moment maps. Their main role is to give the line emission velocity as a function of radius along a line (called a long slit) through an arbitrary position angle. Thus, the construction of the pv diagram through the major axis of a source dominated by rotation as for example a spiral galaxy, gives as a result the projected rotation curve of itself, by showing the velocity of a certain component (e.g. specific gas or stars) of the galaxy viewed edge-on along the line of sight as a function of distance from the center.

To understand how this is generated, first we choose a slit with a length proportional

to the spatial size of the data cube and a width at some pixels which could be estimated depending on the beam size of the observed data (not mandatory, changeable according to the own requirements). Then the slit is placed it on the data cube and oriented at certain angle of our convenience blocking the spectra from the rest of the data cube. Thus, only all spectra in each pixel covered by this slit are extracted one by one to then being plotted as a function of velocity (y-axis) and distance to the center (x-axis). The velocity values are associated with the spectral dimension in the data cube while the distance values are according the spatial dimensions (x,y) of the same (see the dimensions in Fig. 2.2).

The resulting plot is similar as we can see for our sources in Figs. 2.7 and 2.6. Colors convey the intensity of the emission (redder imply higher, bluer is lower) giving us an extra information about the spread in velocity at different distances (offsets) from the nucleus. For pv diagrams along the major axis, we have overplotted the projected rotation curve with respect to the circular velocity model used (Eq. 2.1). For a galaxy in a ideal circular rotation regime, the pv diagram along the major axis would be a perfect S-shape mirrored not only across the y-axis but also the x-axis. For the minor axis, the velocity would be zero for any offset from the center. Galaxies NGC 2110 and NGC 1386 trace a projected rotation curve strongly correlated with a normal circular rotation however in both cases, their minor axis show velocity components in the inner 5″ indicating an inflowing/outflowing scenario depending on their orientations with respect to the LOS. For NGC 2110 these deviations seem to be significantly important with velocities around ± 200 km s^{-1}. For NGC 1667, the components seem to show a characteristic S-shape indicative of normal rotation velocities but these are offsets with respect to the model overplotted. This reinforce the fact mentioned in Sect. 2.3.1 that this galaxy does not match well with the model giving as a result, non circular components in the inner region as in its residual map as in the pv diagram that could be a result of a bad subtraction due to PA differences in the major axis between the model and the observing data and not necessarily real non-circular components as nuclear inflows/outflows. For NGC 7213 the interpretation result difficult due to the poor data.

Therefore, has been revealed the complementary advantages by analyzing projected rotation curves through pv diagrams and so to describe the kinematics in several sources. The pv diagrams allow us to identify features that could be ‘hidden’ in velocity maps as consequence of data averaging, instead, pv diagrams are a direct method which extract the information from the data cube showing data along the spectral dimension without

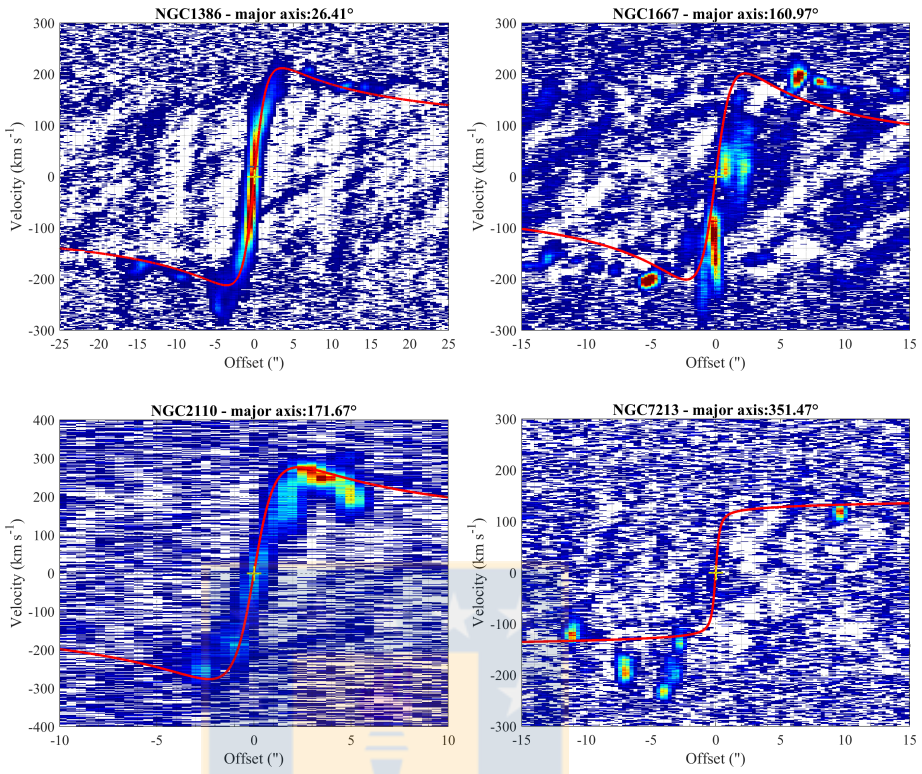

Figure 2.6 Position-Velocity diagrams for major axis in each source. Red solid lines represent the projected rotation curve from our velocity model (Eq.2.1) whereas yellow crosses indicate the kinematic center of the source. The position angle (PA) of the 'slit' over which the pv diagram was extracted is indicated above each panel. Positive offsets on the x-axis correspond to the PA listed above the panel, i.e. negative offsets are along the 180° plus the listed PA. For NGC 1566, see Fig. 3.9. Source: Ramakrishnan et al. (2018).

averaging which makes it more efficient in the detection of weaker non-circular components.

In Sect. 3.3.5, is shown a more complete analysis by using this method in our best-detected galaxy NGC 1566. A similar features are present but it is analyzed other potential implications that could be participating to generate these deviations, specially if the role of the long scale bar is of greater significance at inner scales or if that features are direct consequence of an AGN activity in its center.

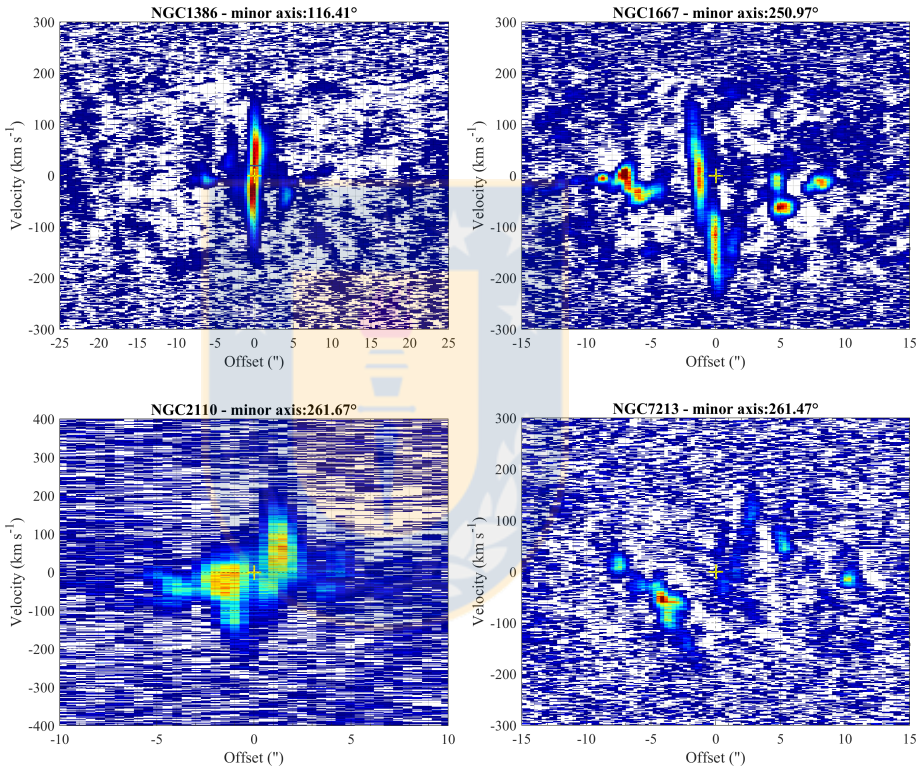

Figure 2.7 Position-Velocity diagrams for minor axis in each source. Specifications as in Fig. 2.6. For NGC 1566, see Fig. 3.9. Source: Ramakrishnan et al. (2018).

3

Morphology and Kinematics in the inner kiloparsec of NGC 1566.

3.1 Introduction

Supermassive black holes (SMBH) are thought to be ubiquitous in galaxies with bulges and may be key to the formation and evolution of galaxies (Kormendy & Ho, 2013). The correlation between the host bulge and central black hole mass (Ferrarese & Merritt, 2000; Gebhardt et al., 2000; Tremaine et al., 2002; Ferrarese & Ford, 2005; Gültekin et al., 2009; Kormendy & Ho, 2013) has been argued to imply a direct causal relationship between the accretion of material by the black hole, the host galaxy star formation and AGN-driven feedback, but direct observational evidence of the mechanisms responsible has remained elusive (Heckman & Best, 2014). Over the past decade, there have been a growing number of facilities providing 3-D spectroscopic imaging observations which have been supporting the study of gaseous and stellar kinematics in active and inactive galaxies at radio (e.g. Morganti et al., 2009; Nesvadba et al., 2010), infrared wavelengths (e.g. Storchi-Bergmann et al., 2010; Riffel et al., 2013; Diniz et al., 2015) and optical (e.g. Dumas et al., 2007; Storchi-Bergmann et al., 2007; Dicaire et al., 2008; Westoby et al., 2012; Schnorr-Müller et al., 2014a; Lena et al., 2015; Roche et al., 2016). The combination of enhanced sensitivity at unprecedented spatial and spectral resolution provided by ALMA has opened a new window on molecular gas dynamics to study the central kiloparsec of local galaxies where the dynamical and AGN-activity timescales become comparable, and nuclear fueling, AGN feedback and host galaxy quenching can be probed

directly.

NGC 1566, a nearly face-on barred spiral galaxy (morphological type SAB) is the dominant (de Vaucouleurs, 1973) and brightest member of the Dorado group (Bajaja et al., 1995; Agüero et al., 2004; Kilborn et al., 2005), and one of the nearest and brightest Seyfert galaxies. Despite having many features of a Seyfert 1, several studies (Alloin et al., 1985; Bottema, 1992; Ehle et al., 1996; Kawamuro et al., 2013) have indicated this nature as uncertain. NGC 1566 has an intermediate-strength bar (projected radius 33″ or ∼1.5 kpc and P.A. ∼0°; Agüero et al., 2004), and two strongly contrasted spiral arms. Both the assumption of trailing spiral arms and the more marked dust obscuration on the NW side (dust in the disk obscuring light from the bulge) seen in Hubble Space Telescope (HST) imaging (Malkan et al., 1998), point to the NW side as the near side and the SE as the far side of the disk.

Despite its proximity, the distance of NGC 1566 is controversial. Several studies using the Tully Fisher Relation (TFR) have claimed distances between 18 Mpc (EDD[1]) to around 6 Mpc (Sorce et al., 2014; Tully et al., 2013). The HI spectra used in these studies, though of high signal to noise, clearly show a double-peaked structure, which could lead to significant underestimations of the rotation velocity and thus the TFR based distance. Consequently, in this work, we use the mean distance of 10 Mpc from NED[2], in agreement with the distance used by Combes et al. (2014, hereafter C14). At this adopted distance, the linear scale in our images is 48 pc/arcsec.

The systemic velocity of NGC 1566 is 1504 km s^{-1} from HI observations (NED), but there is wide range in the optical-spectroscopy based recession velocity values found by different authors. C14 found a systemic velocity of 1516 km s^{-1} for CO J:3-2; offset ∼12 km s^{-1} from the HI- derived value. We (see below) find that the galaxy's integrated CO J:2-1 profile is centered on a systemic velocity of 1485 km s^{-1}. As we discuss in this work, the nuclear CO profiles are highly perturbed and non-axisymmetric about the nucleus. Thus the molecular gas derived systemic velocities do not necessarily trace the true systemic velocity of the nucleus of NGC 1566.

The position angle of the major axis of NGC 1566 is ∼45° (HyperLEDA; Makarov et al., 2014)[3], and the inclination of the disk was found to be i=35° (C14, Agüero et al., 2004).

[1] http://edd.ifa.hawaii.edu/dfirst.php

[2] The NASA/IPAC Extragalactic Database (NED) is operated by the Jet Propulsion Laboratory, California Institute of Technology, under contract with the National Aeronautics and Space Administration.

[3] http://leda.univ-lyon1.fr/

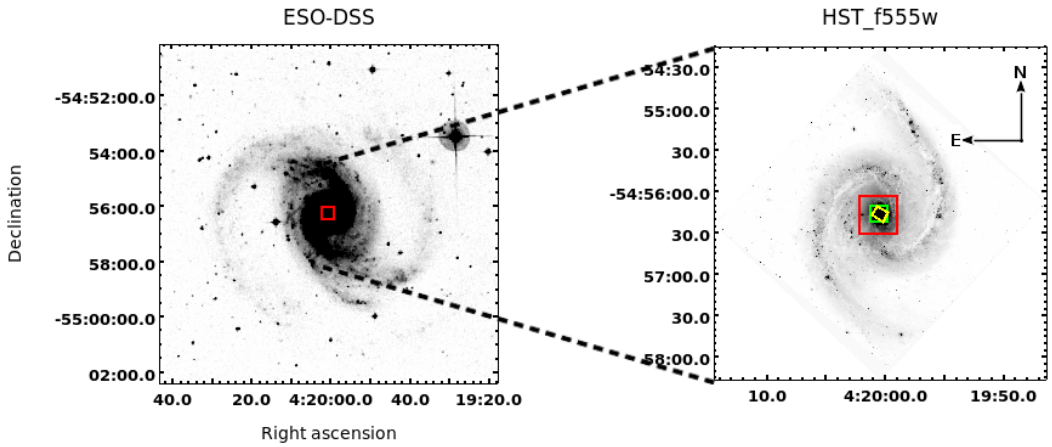

Figure 3.1 Wide field images of NGC 1566. The left panel (ESO-DSS image from the UK Schmidt Telescope) shows the full galaxy, while the right panel (ID:13364, PI:Calzetti. HST image taken with the F555W filter) shows the inner morphology, and highlights the inner spirals arms and the ∼1′ bar in PA ∼0. In both panels the fields of view of the datasets used in this work are shown in yellow (GMOS/IFU), green (inner ALMA FOV: 12″ × 12″) and red (full ALMA FOV: 27″ × 27″) squares. Source: Slater et al. (2018).

In this work we use this major axis position angle and a galaxy disk inclination of i=33°, as derived from our CO data (Sect. 3.2).

HI studies of the local group of NGC 1566 (a sub-part of the Dorado group) show that NGC 1566 is interacting with its smaller companions (Kilborn et al., 2005), and this finding is reinforced with the strong correlation found between galaxies with prominent barred structures and companions in the Dorado group (Kendall et al., 2011). Given its strong and symmetric spiral arms, its active nucleus (AGN), and its proximity, NGC 1566 has been the subject of great interest within the community, and has extensive studies of its spiral arm formation (Korchagin et al., 2000; Ma, 2001; Erwin, 2004; Kendall et al., 2011), its gas kinematics (Pence et al., 1990; Bottema, 1992; Bajaja et al., 1995; Agüero et al., 2004; Dicaire et al., 2008; Mezcua et al., 2015) and the feeding and feedback of the SMBH in its center (Elvis et al., 1989; Schmitt & Kinney, 1996; Combes et al., 2014; Smajić et al., 2015; Davies et al., 2016; da Silva et al., 2017).

An early kinematic study of NGC 1566 in HI and Hα (Pence et al., 1990) showed that the most significant Hα kinematic feature (after subtraction of regular rotation) was a spiral arc located 26″ from the nucleus towards the main spiral arm on the southeast (far) side of the galaxy. This spiral arc has a redshifted velocity of 60 km s^{-1}, i.e. gas moving away from the nucleus under the assumption of motion in the disk of the galaxy.

Under this assumption, Pence et al. (1990) estimated outflow velocities, most plausibly driven by the AGN, of 130 km s^{-1} in the plane of the galaxy, i.e., an equatorial outflow. Schmitt & Kinney (1996) also supported the presence of an outflow when analyzing the morphology of the nuclear [OIII] emission; they observed a total extension of ∼0.″7, mainly to the SE, which they interpreted as the base of a conical NLR originating in the nucleus and oriented perpendicular to the plane of the disk, i.e. a polar outflow. An extension in the nuclear [OIII] emission to the SW was also found by da Silva et al. (2017) in integral field unit (IFU) imaging. They interpreted the morphology and blue-shifted kinematics of the [OIII] line as being consistent with an outflow of ∼500–800 km s^{-1} driven by the AGN perpendicular to the plane of the disk. Agüero et al. (2004) found a HII deficiency in the inner regions of NGC 1566 (see also Pence et al., 1990), reinforcing the evidence of outflows to the SE, and posited that the blueshifted knot found ∼8″ from the nucleus on the far side of the disk signaled the presence of inflows along the galaxy minor axis. Using optical integral field spectroscopy, Davies et al. (2016) found a high (∼100–200 km s^{-1}) dispersion in the Hα line over a region ∼200pc to the SW of the nucleus, which they interpret as most likely due to an outflowing gas illuminated by the radiation field of the AGN. They find that the latter is sufficiently high to drive outflows in this galaxy. In X-rays, Elvis et al. (1989) found extended X-ray emission centered at a position ∼10″ from the nucleus along PA=308° and at 30″ from the nucleus on the (roughly) opposite side (PA=130°). Pence et al. (1990) compared their posited outflow model with these extended X-ray emission regions and found that they share the same center. Radio imaging with *Australia Telescope Compact Array* (ATCA) at 3.5 cm (1.3 × 0.75 arcsec synthesized beam; Morganti et al., 1999) detected the nucleus in continuum, with a potential extension in PA ∼10°, and a weak radio blob 3 arcsec to the N (PA ∼10°). The nucleus is detected by the *Parkes Tidbinbilla Interferometer* (PTI) at 13 cm (5 mJy; Roy et al., 1994), i.e. it hosts a compact radio source. The previous reports of outflows in NGC 1566 are consistent with a picture of a nuclear outflow driven by the AGN in which the compact base detected in blue-shifted [OIII] is primarily from a polar ionization cone tilted towards the observer and close to face-on and a more extended (out to 1 kpc) equatorial outflow component detected in a Hα arc in the disk of the galaxy. The reason that only the blueshifted inner (¡1″) ionization cone has been detected towards the far side of the galaxy disk most likely lies in the dusty features seen on the opposite side (NW) of the nucleus (see Fig. 8 of da Silva et al. (2017) and our structure map in Fig. 3.3).

C14 have presented CO J:3-2 observations of NGC 1566 using ALMA in Cycle 0: their relatively low spectral resolution (∼10.2 km s^{-1} per channel) and relatively sparse *uv* coverage limited the interpretation of the molecular gas kinematics in the nuclear region. Their kinematic study of the CO emission showed a relatively regular rotational velocity field with redshifted streaming motions on the far side of the minor axis, and blueshifted streaming motions on the near side, both centered on, and within a few arcsec of the nucleus. However, they argued that the small velocity amplitudes (total width $\lesssim$100 km s^{-1}) of these perturbations, and the fact that they were only seen in the central 1″, makes an outflow scenario improbable, and instead attributed the non-circular rotational motions to other factors, e.g. streaming and bars. More recently Smajić et al. (2015) extended the same study by adding SINFONI observations of near-IR molecular emission lines, and came to similar conclusions, i.e. reinforcing the idea that the velocity perturbations are more easily explained by streaming motions along the minor axis as a consequence of the central bar, rather than outflows.

In this Chapter, we reanalyze the nuclear molecular and ionized gas kinematics using new ALMA and Gemini-GMOS/IFU data. We present new ALMA observations of NGC 1566 in the CO J:2-1 emission line which covers the inner 12″ (∼600 pc) at 1.3 km s^{-1} channel spacing, i.e. a ∼2.6 km s^{-1}spectral resolution. These new CO J:2-1 observations are more sensitive allowing us to create datacubes at the intrinsic channel spacing of the observations and have a higher image fidelity (due to the improved *uv* coverage from the ∼32 antenna array) as compared to the previously published Cycle 0 CO J:3-2 observations. We compare the distribution and kinematics of molecular gas with that of ionized gas (specifically the [NII] 6583Å emission line) and stellar absorption lines observed with Gemini-GMOS/IFU at optical wavelengths. We argue that the kinematics can be best explained by a quenched spherical outflow in ionized gas, a decelerating outflow of molecular gas in the plane of the inner (∼300 pc) disk (a scenario we favor over only bar-perturbed kinematics and streaming), and discuss molecular gas streaming inflows to the nucleus.

This Chapter is structured as follows: In Sect. 3.2 we present the observations and data processing. In Sect. 3.3 we present our results, including the morphology and kinematics of the ionized and molecular gas and stars, a comparison with our outflow, bar-perturbation and streaming models, and a discussion of the results. Finally, in Sect. 3.4, we present our summary and conclusions.

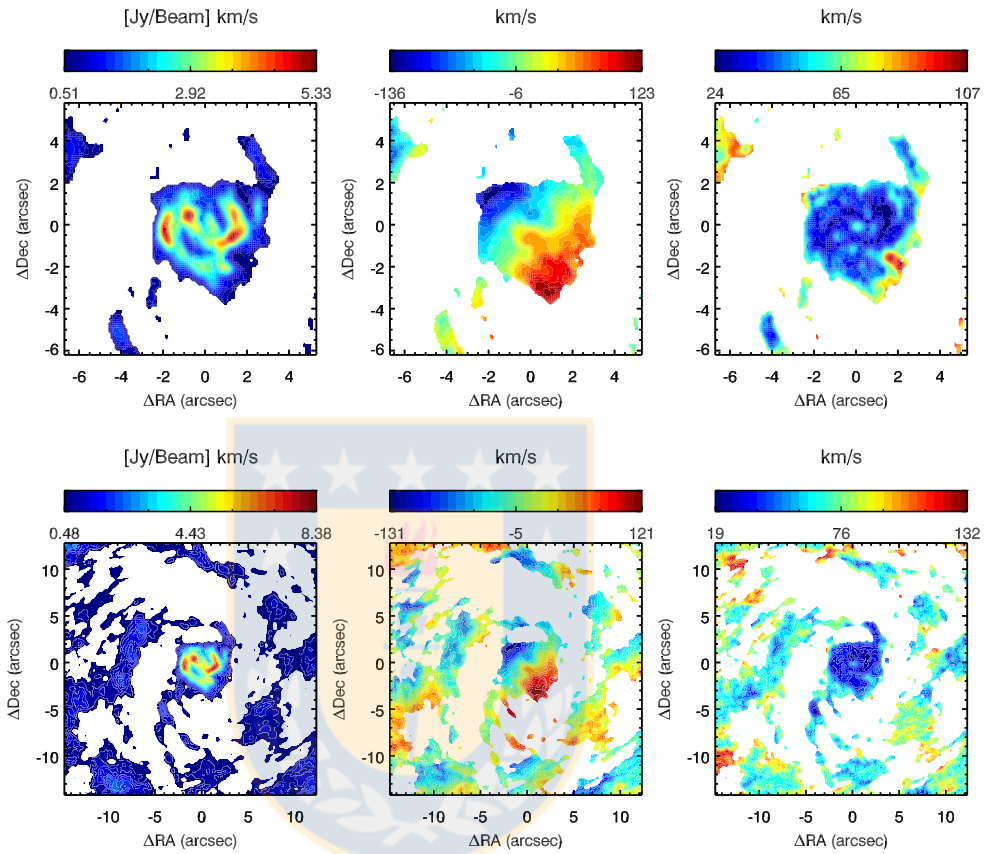

Figure 3.2 Moment maps of the CO J:2-1 emission in NGC 1566. Left to right panels show the 0th (integrated flux), 1st (velocity) and 2nd (velocity dispersion) moments. The top row shows the moment maps derived from the highest spatial resolution maps (over a $12'' \times 12''$ FOV) to best emphasize the nuclear features. The moment 0 (left) panel has a r.m.s. of 0.17 Jy/beam km s^{-1}, and pixels with flux density lower than 0.51 Jy/beam km s^{-1} (3σ) in the moment 0 image were 'masked' in all panels of the row by setting them to a value which results in a white color in the panel. The bottom row panels show the moments derived from lower spatial resolution (but higher signal to noise) maps and show a larger $27'' \times 27''$ FOV to emphasize the larger scale spiral arms. The moment 0 (left) panel has a r.m.s. of 0.16 Jy/beam km s^{-1}, and pixels with flux density lower than 0.48 Jy/beam km s^{-1} (3σ) in the moment 0 images were 'masked' in all panels. Source: Slater et al. (2018).

3.2 Observations, Data Processing, and Software

We observed NGC 1566 with ALMA and Gemini-GMOS/IFU in order to obtain a comprehensive picture of the morphology and kinematics of the molecular gas, ionized gas, and stars. Images of NGC 1566, illustrating the FOVs of our observations are shown in Fig. 3.1.

We observed NGC 1566 with ALMA as part of a survey of five nearby Seyfert galaxies during Cycle 2: *project-ID 2012.1.00474.S* (PI: Nagar) originally approved for Cycle 1 but carried over to Cycle 2. The observations of NGC 1566 were taken on June 29, 2014, using the ALMA Band 6 receivers on thirty-two 12-meter antennas. Four spectral windows (SPWs) were used; two in the lower sideband (LSB) and two in the upper sideband (USB). Three of the SPWs were configured to cover the following lines at relatively high channel spacing (~1.3 km s^{-1}): CO J:2-1 (ν_{obs} = 229.401922 GHz) , 13CH3OH (ν_{obs} = 241.548041 GHz) and CS(J:5-4) (ν_{obs} = 243.728532 GHz). A fourth SPW was used in 'continuum' mode to best detect any nuclear continuum emission. The SPWs were thus centered on 229.415 GHz, 227.060 GHz, 241.554 GHz and 243.735 GHz, with bandwidths of 1.875 GHz, 2.0 GHz, 1.875 GHz and 1.875 GHz, respectively, and spectral channel spacing of 1.27 km s^{-1}, 20.53 km s^{-1}, 1.22 km s^{-1}, and 1.21 km s^{-1}, respectively. At these frequencies, the full-width half maximum of the 12 m primary beam is about 26′. Antenna baselines ranged from 17 m to 650 m, resulting in a typical synthesized beam of 0.″6 × 0.″5 with a position angle (PA) of 25.3°.

Observations were carried out in two continuous observation blocks, totalling 124 min. The nearby radiogalaxy J0519-4546 (PICTOR A) was used as a phase, bandpass and flux-calibrator. Data were calibrated and imaged using CASA 4.2.1 (McMullin et al., 2007). The CO J:2-1 emission line was strongly detected over a velocity range of ~ ±200 km s^{-1}, and we were able to map the CO line at the observed channel spacing of 1.3 km s^{-1}. Thus, our effective spectral resolution (2.6 km s^{-1}) is higher than the internal dispersion of a typical GMC. At this spectral resolution, our highest spatial resolution maps (made with Brigg's weighting with the *robust* parameter set to −2) have a synthesized beam of 0.″52 × 0.″35 (beam PA= 13°). The r.m.s. noise per channel in line free channels is ~1 mJy/beam, and rises by up to a factor 2 in channels with significant line emission. Equivalent 'natural weighted' maps (Brigg's weighting with *robust*=2) have a resolution of 0.″6 × 0.″5 (beam PA= 15.6°) and an r.m.s. noise per channel of 1.2 mJy/beam in line free channels, rising

by up to a factor of 4 in channels with significant line emission. The task *immoment* of CASA was used to create moment (integrated flux, velocity, and dispersion and skewness) maps from the above data cubes.

Gemini-GMOS observations of NGC 1566 were obtained on the night of 27th of September 2011 with GMOS in IFU mode and using the R400_G5325 grating in combination with the r_G0326 filter (*program ID: GS-2011B-Q-23*; P.I. Nagar). This grating yielded an intrinsic spectral resolution (FWHM) of 123 km s^{-1}, which was sampled on the CCD at ~30 km s^{-1} per pixel near the [NII] line. The total spectral coverage was from 5620Å to 6970Å. The observations consisted of two adjacent IFU fields covering $7'' \times 5''$ each, resulting in a total spatial coverage of 7×10 arcsec. Six exposures of 350 seconds were obtained for each field, each slightly shifted in wavelength and position in order to correct for detector defects and fill in CCD chip gaps. The data was processed using specific tasks developed for GMOS data in the *gemini.gmos IRAF*[4] package.

We use four software packages for obtaining velocities, velocity fields, and related parameters from the datacubes or moment images. Ionized gas kinematics were obtained by fitting Gauss-Hermite polynomials and double Gaussians to the [NII] 6583Å emission line using a modified version of the *profit*[5] routine (Riffel, 2010). The Gauss-Hermite polynomial fits were used to obtain total flux (moment 0), velocity (moment 1), and velocity dispersion (moment 2) maps over the full FOV. The nuclear stellar velocity and velocity dispersion was determined by using the *Penalized Pixel Fitting (pPXF)*[6] code (Cappellari & Emsellem, 2004), on the integrated (over our full FOV) spectrum of the galaxy, and using templates based on simple stellar populations (SSPs) from Bruzual & Charlot (2003).

We used a modified version of the *Kinemetry*[7] package (Krajnović et al., 2006) to constrain the major axis and inclination of NGC 1566 via fits to the CO J:2-1 velocity field, and to determine the best fit circular velocity field via fits to the moment 1 (velocity) maps of both CO J:2-1 and [NII]. This modified version uses an improved global optimization thereby yielding results that are less affected by the starting values and are more robust to missing pixels in the map (discussed in detail in Ramakrishnan et al., 2018). Some parameters such as the position angle and inclination of the galaxy can either be fixed or

[4]http://iraf.noao.edu
[5]http://w3.ufsm.br/rogemar/software.html
[6]http://www-astro.physics.ox.ac.uk/ mxc/software/
[7]http://davor.krajnovic.org/idl/

obtained on the fly (see Krajnović et al., 2006, for a more detailed description of the software and its features). On the first *Kinemetry* run we allowed both PA and inclination to vary with radius. The PA and inclination were then fixed to their median values and a second run of *Kinemetry* was used to obtain the circular rotation map and the coefficients of each circular velocity and perturbation term. Briefly, *Kinemetry* fits concentric elliptical rings to the velocity fields under the assumption that it is possible to define the latter such that data extracted along each ellipse can be described by a simple cosine law. Therefore, along each ellipse fitted to our velocity map, the program constructs a Fourier series as a function of azimuthal angle. When using *Kinemetry* we used six odd terms, i.e. cos(nθ) and sin(nθ) with n=1, 3, 5.

3.3 Results

The molecular (CO; ALMA) and ionized gas emission lines (Gemini-GMOS/IFU) are detected at high signal to noise out to the edge of the observed FOV. The [NII] emission line is detected in every pixel of the GMOS FOV at signal to noise ratios of 3 to 250 in the moment 0 maps. The CO line is detected in well defined structures which cover a fraction of the FOV: here the signal to noise ratio in moment 0 maps ranges between 8 and 35.

3.3.1 Observed Moment Maps: ALMA and Gemini-GMOS/IFU

Our ALMA 230 GHz continuum map shows only an unresolved nucleus and a few other weakly detected components. We do not present or discuss these 230 GHz continuum maps further since the sub-mm continuum morphology of the nuclear region can be better appreciated in the 345 GHz continuum maps of C14 due to the dust emission being brighter at this frequency. The principal use of our 230 GHz continuum map is thus to set the position of the nucleus in the CO maps. The extensive dust lanes in the nuclear region of NGC 1566 could cause a small systematic offset between the nucleus and the location of the optical continuum emission peak. Since this systematic offset is most likely to be significantly less than 0.″5 (see the structure map in the bottom panels of Fig. 3.3) we here assume that the nucleus is coincident with the stellar continuum peak in the Gemini-GMOS datacube.

The moment 0 (integrated flux), moment 1 (velocity) and moment 2 (velocity disper-

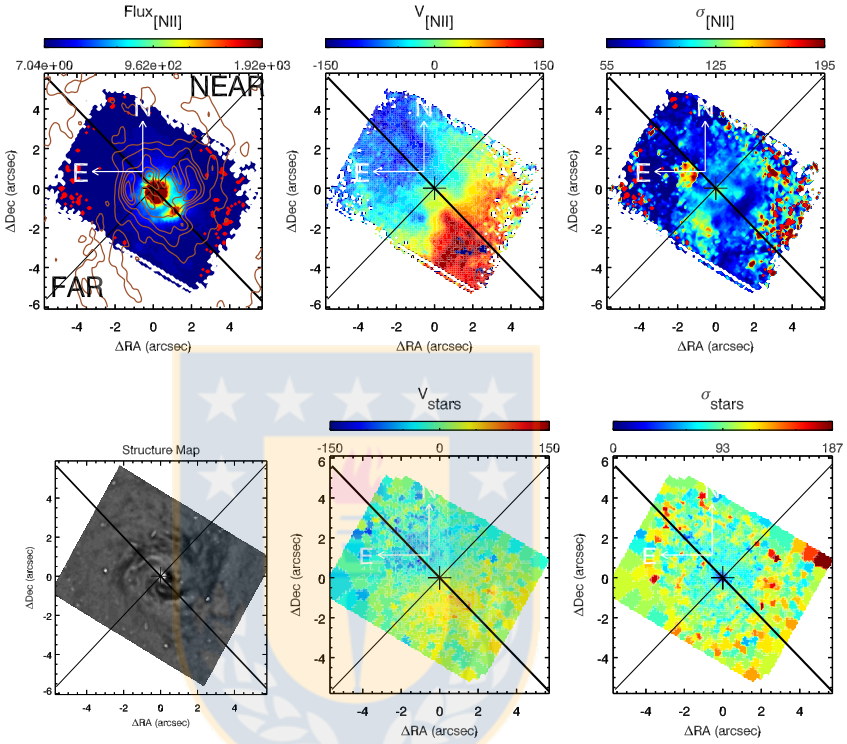

Figure 3.3 [NII] and stellar moment maps as well as the structure map in NGC 1566. Top row: Moment maps of the [NII] 6583Å emission line. From left to right, the panels show the 0th (integrated flux), 1st (velocity) and 2nd (velocity dispersion) moments. The nuclear position (marked with a cross) was derived from the peak flux of the continuum in Gemini-GMOS datacube, and the solid lines indicate the major axis (thick line) and the minor axis (thin line). In the moment 0 map (left panel), the brown contours show the integrated flux (moment 0) of the CO J:2-1 line. Bottom row: from left to right the structure map, and maps of the stellar velocity and stellar velocity dispersion. All maps have N to the top and E to the left (see compass). The structure map was created from a HST F606W filter on which unsharp masking was used to emphasize dust features. It is shown at the same size and orientation as the other panels. Source: Slater et al. (2018).

sion) maps of the CO J:2-1 line in NGC 1566 are shown in Fig. 3.2. The molecular gas in the nucleus of NGC 1566 has a clearly defined disk-like structure in the inner 3″ (144 pc), even though this region is deficient in both atomic gas and H II regions (Pence et al., 1990; Agüero et al., 2004; Smajić et al., 2015). Within this nuclear disk, the CO J:2-1 traces a two-arm spiral structure in the inner 1.″7 (82 pc); this spiral structure is also seen in near-infrared and optical images (Smajić et al., 2015) and in previous CO J:3-2 maps (C14). This inner molecular spiral (in which the arms almost close into a ring) sprouts two more extended but fainter CO J:2-1 spiral arms which extend out of the inner disk until roughly 134 pc (2.″8). These more extended spiral arms coincide with the dust lanes seen in HST images (Fig. 3.3; see also C14). The CO velocity map shows velocities ranging over ± ∼140 km s^{-1}. While the disk in its inner 3″ shows a predominantly rotational 'spider' velocity diagram, the velocities are asymmetrical, pointing to a warped inner disk or the presence of non-circular velocities. Despite the common association of outer HI disks to warped disks, there exists some evidence for the latter at parsec scales (Greenhill et al., 2003). Warp scenarios at nuclear scales for molecular gas has been explored as, e.g. in Schinnerer et al. (2000) reporting that molecular gas could be warped or bar perturbed in the nuclear region, although without analyzing deeply the origins of thereof. The trailing pattern of spiral arms in the CO velocity maps agrees with that at larger scales in the right panel of Fig. 3.1, allowing us to assume that the near and far sides of the galaxy disk is to the NW and SE, respectively. The velocity dispersion map reveals a typical dispersion of ∼30 km s^{-1} in the inner spiral arms (see also Fig. 3.6), with a high (∼100 km s^{-1}) velocity dispersion region ∼3″ to the SW of the nucleus along the major axis. Note that this region does not correspond to the star-forming region which is clearly detected in the optical observations of Smajić et al. (2015). The nucleus of NGC 1566 shows a velocity dispersion of ∼ 60 km s^{-1} (see also Fig. 3.6).

The moment maps of the [NII] line in NGC 1566, obtained from the GEMINI-GMOS/IFU data, are shown in the top row of Fig. 3.3. Overall, these are roughly similar to those of the CO line. The [NII] moment 0 image clearly shows the bright [NII] region to the SW, corresponding to the optically-emitting star-forming region seen in Smajić et al. (2015) and in agreement with a blue region seen to the SW of the nucleus in the CO velocity residual map. The velocity map shows kinematics consistent with rotation with velocities similar to those seen in the CO maps. Once more there are non-symmetrical velocity patterns closest to the nucleus: note especially the excess of blueshifts seen on the far side of

the galaxy disk ∼2″ from the nucleus. The map of the [NII] velocity dispersion is more difficult to interpret. The [NII] dispersion is in general higher than that seen for CO, and the inner spiral structure is not as clearly discernible as a higher dispersion region. The star-forming region to the SW has a dispersion of ∼50 km s^{-1} in [NII] (less than that in CO). The nucleus shows a velocity dispersion (∼120 km s^{-1}) significantly higher than that seen in CO and two regions ∼2″ from the nucleus in the NE and S directions also show relatively high (150–180 km s^{-1}) velocity dispersions. These will be interpreted below in conjunction with the results of the two component fits to the [NII] emission line.

The bottom row of Fig. 3.3 shows a structure map and the first two moments of the stellar velocity field. The structure map was created by running the IDL routine 'unsharp_mask.pro' on a HST image taken through the F606W filter, in order to emphasize sharp changes in the image. While the highest contrast dust arc is seen on the far side of the galaxy as expected, several strong dust features are also visible on the near side of the galaxy. The stellar velocity map, derived from running *pPXF* on a Voronoi binned datacube (to achieve a minimum signal to noise of 25 in the continuum near the [OIII] line in each spectrum), shows a clear rotation pattern. The stellar rotation velocities are significantly lower than those seen in the molecular gas. Since the map is relatively noisy even after Voronoi binning we did not attempt to fit a PA and inclination to this velocity field using *Kinemetry*. Visually, the PA appears consistent with the values we derive from our CO J:2-1 map; this is corroborated by our best fit rotation model to the stellar velocity field (see next section).

3.3.2 Modeling the Observed Velocities: Rotation

We used *Kinemetry* to analyze the CO J:2-1 velocity field (see Sect. 3.2), both to constrain the PA and inclination of the CO disk, and to constrain the relative contributions of circular rotation and perturbations. We assumed m=2 modes and thus use six (odd) Fourier decomposition terms. In the first run both the PA and inclination were allowed to vary with radius, and in the second run we fixed both to their median values from the first run. The Fourier decomposition coefficients of the best fit *Kinemetry* model are shown in Fig. 3.4. Here the $\cos\theta$ term represents the pure circular (rotation) velocity and the other terms are perturbations. In the innermost ∼1″, the $\sin\theta$ (radial) term is positive and dominates the pure rotation term (below we argue that this is best explained by a nuclear outflow) while the $\cos\theta$ (circular rotation) term dominates between ∼1 and 4″.

Beyond 3.4″, the CO velocity field is sparse and the results of *Kinemetry* are thus less reliable. Nevertheless we note that the coefficient of $\sin\theta$ remains stable at ∼20 km s^{-1}at radii beyond 1.4″, and the $\cos 3\theta$ coefficient is significantly negative between 4″and 5″ which could signify an asymmetry about the minor axis. The other terms show relatively small amplitudes, and given that we sample a very small range of radii (significantly less than the bar co-rotation radius) we are unable to reliably interpret their variations. To emphasize the changing reliability of these results with radius we plot two dashed vertical lines. To the left of these is the region with a 100% of data coverage in the ellipse fitting (between 0 and 2.2″); between these there is a linear decrease from 100% to a 50% and to the right of these the data coverage of the ellipse fitting is lower than 50%, decreasing to 30% at 3.4″and beyond. It is thus clear that beyond 3 to 4″ the values of the coefficients are relatively unreliable due to the sparseness of the velocity field, and we thus do not attempt to interpret, e.g., the fact that the s1 term remains positive and almost constant.

We fit the observed stellar velocity field with a 'Bertola' model rotation curve (Eq. 2; Bertola et al., 1991). This model uses six parameters: the maximum amplitude of the rotation curve A; the radius at which this maximum amplitude is achieved c; a p factor which drives the slope of the rotation curve at larger radii (p=1 gives a flat rotation curve at large radii and p>1 gives a decreasing rotation curve at large radii, emulating a finite total mass in the disk), the position angle of the major axis; the inclination of the galaxy, and the systemic velocity. Of the six parameters of the model we fixed the c parameter (by visual inspection of the radius at which the rotation amplitude reached its maximum) and the inclination (the same value obtained running *Kinemetry* on the CO velocity field). The best fit parameters obtained were A=200 km s^{-1}, p=1.5, PA=45° (same as derived by *Kinemetry* on the CO velocity field), and a systemic velocity offset of −5 km s^{-1} with respect to that used in this work (1485 km s^{-1}). This rotation model is shown with a dash-dotted line in Fig. 3.5, and is later (Sect. 3.3.6) used in the bar perturbation analysis.

The asymmetries in the observed CO and [NII] velocity fields are best appreciated once ordered rotational motions are subtracted out. We use three rotation models for our analysis of the observed gas velocity maps: all models use a major axis P.A. of 45° and an inclination of i=33°, derived from running *Kinemetry* on our CO J:2-1 velocity field. These three models differ in the parametric form of the circular rotation velocity with

radius: (a) solid body rotation with parameters:

$$Vc_{radial} = (S_{rot} * r) * \cos(\phi) * \sin(i). \quad (3.1)$$

where S_{rot} is equal to 1.9 [km $s^{-1}pc^{-1}$], r and ϕ are the polar coordinates in the velocity map, and i is the galaxy inclination; (b) An empirical axisymmetric rotation model (hereafter, ModC2014) based on the nuclear rotation curve derived by C14, but with a gradual decrease in circular velocity beyond 2″, roughly following the results from the *Kinemetry* fit to the CO J:2-1 velocity field. Recall that C14 derived the nuclear rotation curve by using their observed CO J:3-2 velocity field - specifically by minimizing the residual (observed − model) velocities - at small radii, and literature Hα velocities at larger radii (the black line in their Fig. 9). Since the nuclear CO kinematics are highly perturbed and the velocity field is relatively sparse (especially beyond 2.″5), it is not clear that a *Kinemetry* fit or a minimization of residuals will produce a reliable circular rotation model. In fact the circular velocity model obtained by applying *Kinemetry* to our CO velocity field, and that from fitting a Bertola model to the stellar velocity field, are both significantly different from the C14 rotation model (Fig. 3.5): the most significant difference is a decrease in the rotation velocities beyond 2″. Since a major function of the rotation model in the following sections is to emphasize asymmetries in the observed velocity field, we create a smooth rotation model which follows C14 (and the solid body model above) in the inner 2″ and decreases (to reflect the *Kinemetry*-derived and Bertola models) at larger distances (dashed lines in Fig. 3.5). This ModC2014 model is used to produce residual (observed − model) velocity maps which better emphasize deviations from circular rotation as compared to using the C14 rotation model; and (c) the gas circular rotation model (specifically the variable gascirc) obtained by running *Kinemetry* on the CO J:2-1 velocity map.

A direct comparison of the rotation models considered by us in the inner kpc of NGC 1566 is shown in Fig. 3.5. The CO J:2-1 velocities extracted along the major axis (crosses) show several differences from the solid body and ModC2014 models. First, the velocities are not axisymmetric with the blue-shifted velocities (to the NE) larger than the red-shifted ones (SW) between 1–2.5 arcsec from the nucleus. Second, both blue and red shifted sides show wiggles with larger velocities in the inner 0.″5 and relatively small velocities at distances ≥2.″5 arcsec from the nucleus. The circular gas velocity fit of *Kinemetry* to the CO J:2-1 velocity field (solid line) is by definition an axisymmetric fit;

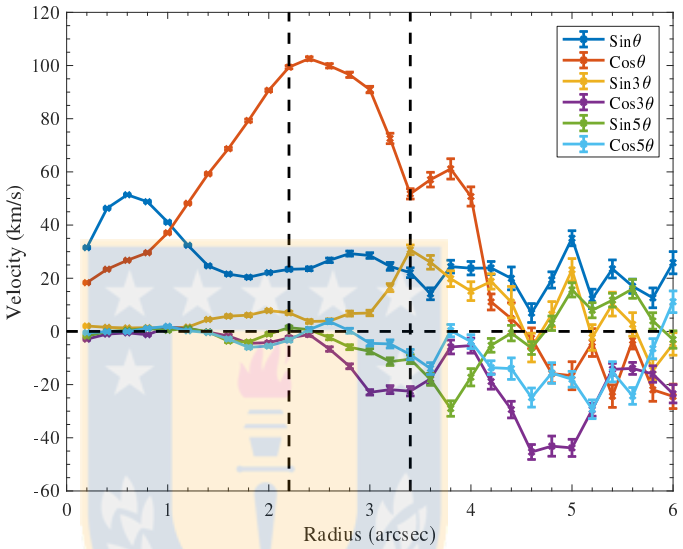

Figure 3.4 Fourier components in CO velocity map of NGC 1566 by *Kinemetry*. The amplitudes were obtained as a function of distance from the nucleus. The solid red line represents the coefficient of the $\cos\theta$ term (pure circular rotation in a disk) and the other solid lines show the additional components (associated to perturbations) in the Fourier decomposition, following the colours specified in the inset. Only odd Fourier components were used. The vertical lines delineate radii at which we have abrupt changes in the fraction of pixels at a given radius which have values in the velocity map. At radii smaller than the left vertical line, this fraction is 1. Between the two vertical lines the fraction drops linearly from 1 to 0.5, and beyond 4″ the fraction is relatively steady at ~0.3. The horizontal dashed line delineates zero velocity. Source: Slater et al. (2018).

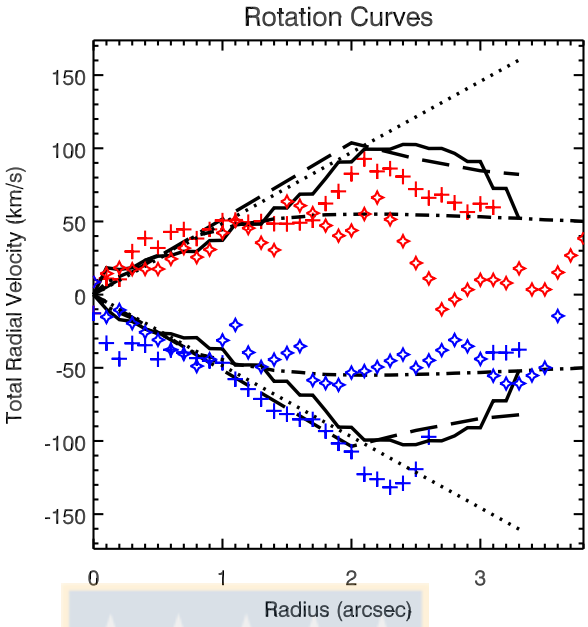

Figure 3.5 Observed velocities and models along the major axis of NGC 1566. Comparison of the (projected) rotation models and observed velocities extracted along the major axis, in the central kpc. The solid body model is shown with a dotted line, our ModC2014 model (see text) is shown with a dashed line, the circular ('gascirc') model obtained by the *Kinemetry* fit to the CO J:2-1 velocity field is shown with the solid line, and the Bertola model fit to the stellar velocity field is shown with a dashed-dot line. CO J:2-1 and stellar velocities extracted along the major axis are shown with crosses and stars, respectively. Blue is used for the NE (approaching) side of the galaxy, and red for the SW (receding) side of the galaxy. The zero velocity on the *y*-axis corresponds to 1485 km s^{-1}; at the nucleus, the velocity of the CO J:2-1 line is offset from this by -12.8 km s^{-1}; a consequence of the asymmetric double-peaked profile of the nucleus, most likely caused by the effects of nuclear outflows and/or bar related perturbations. Source: Slater et al. (2018).

it well follows the solid body rotation model until 2.″4 (except for an excess of velocities in the inner 0.″5 (below we argue that this is due to a nuclear outflow) after which it shows rotation velocities slightly lower than ModC2014.

On the other hand, the stellar velocities along the major axis (stars in Fig. 3.5) presents two stages: the blue and red shifted sides are quite similar until ~2″: in the inner arcsec it is completely consistent with our ModC2014 model. Beyond 2″, on the NE (blueshifted) side the stellar velocities flatten at ~60 km s^{-1} while on the SW (redshifted) side the stellar velocities reach a similar peak but then decrease to almost zero velocity at 2.8″, after which they gradually increase again to ~40 km s^{-1}.

For the three models - solid body rotation, ModC2014, and *Kinemetry*-derived - the residual (observed minus model) CO J:2-1 velocity maps reveal similar asymmetries in the inner 2.6″. The differences in the residual maps are seen at greater radii: the *Kinemetry* model undersubtracts the observed velocities while the ModC2014 and solid body rotation models oversubtract the observed velocities. The *Kinemetry* model results in the best and most symmetrical residual velocity map for CO J:2-1, but does not work well for the GMOS/IFU data. For GMOS-derived ionized gas velocity fields, the inner region is well subtracted but a radii greater than 2″ the velocities are not well subtracted as a consequence of the very low model velocities; i.e., rotation velocities in ionized and stellar lines do not decrease at radii greater 2.6″ as in the case of CO J:2-1. Given that we are interested primarily in identifying deviations from axis-symmetric rotation in the innermost region, rather than accurately predicting the true rotation curve, unless otherwise stated, we consistently use the ModC2014 model for all (ALMA and GMOS) kinematical analysis in this work.

The residual (after subtraction of the rotation model) velocity field of the CO J:2-1 emission line is shown in Figs. 3.6 and 3.7. The departures from pure rotation are now clearer, especially in the inner 3″. The largest deviations are (a) blue and red shifted clumps ∼1″ to the NW and SE of the nucleus; (b) red spiral arms ∼4″ to the N and SE with the latter less redshifted, and (c) a diffuse clump some redshifted ∼3″ to the SW of the nucleus. The blue (residual velocity ∼50 km s^{-1}) clump ∼1.″5 to the SW of the nucleus along the major axis in our CO residual velocity map (Fig 3.7) marks the location of the star-forming region noted by Smajić et al. (2015): recall that this region is discernible in our [NII] moment maps, both as a a high flux region in the [NII] moment 0 map, and a relatively low velocity dispersion region in the [NII] moment 2 map. Further, this is also the region found to have a velocity gradient in its [OIII] emission line da Silva et al. (2017). Disturbances produced by the star forming region could explain why the CO velocity here does not agree with the expectation from pure rotational.

3.3.3 Modeling Observed Velocities: Molecular Outflows?

The CO J:2-1 residual velocity map in Fig. 3.7 shows excess blueshifts to the NW (near side) and redshifts to the SE (far side) of the galaxy, around 1″ from the nucleus along the minor axis. This is the expected signature of outflows within the plane of the galaxy disk. This feature (but at lower spatial resolution, and at significantly lower spectral

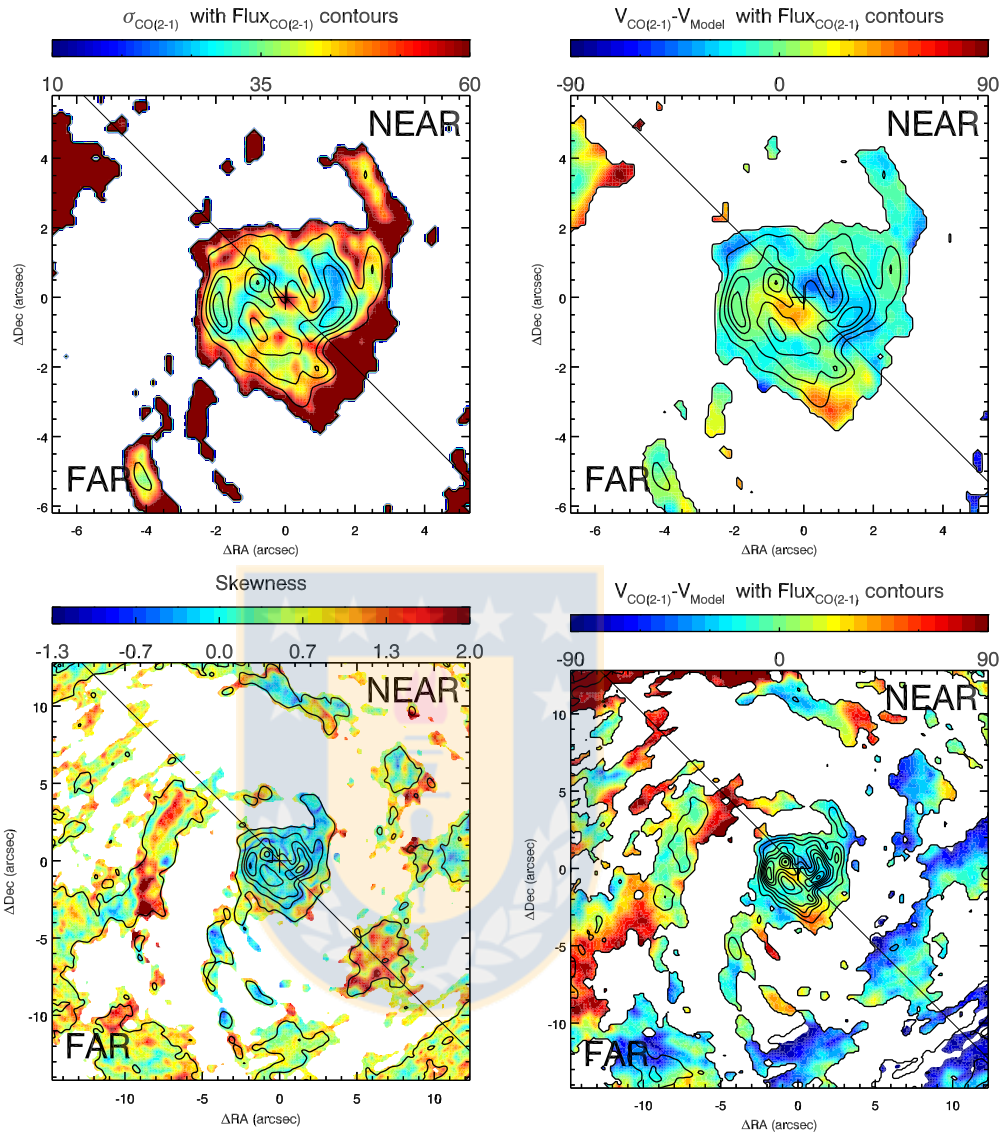

Figure 3.6 Dispersion, skewness and residuals maps of NGC 1566. **Top:** Maps of the CO J:2-1 velocity dispersion (left) and velocity residuals after subtraction of the ModC2014 rotation model (right panel) for the inner FOV. Contours in both panels show the moment 0 (integrated flux) map of the CO J:2-1 emission, ranging from 0.4 mJy/beam km s^{-1} to 5.4 mJy/beam km s^{-1}. **Bottom left:** moment 3 (skewness) map of the CO J:2-1 emission for the larger FOV, shown in color following the color bar: blue colors represent spectra with excess emission towards the blue side of the weighted mean velocity. The CO Moment 0 (total flux) map is overlaid with black contours. **Bottom right:** As in the top right panel but for the larger FOV. Pixels with velocity less than −90 km s^{-1} in the right panels are shown in white. Contours in bottom panels show the moment 0 (integrated flux) map of the CO J:2-1 emission, ranging from 0.4 mJy/beam km s^{-1} to 8.4 mJy/beam km s^{-1}. Source: Slater et al. (2018).

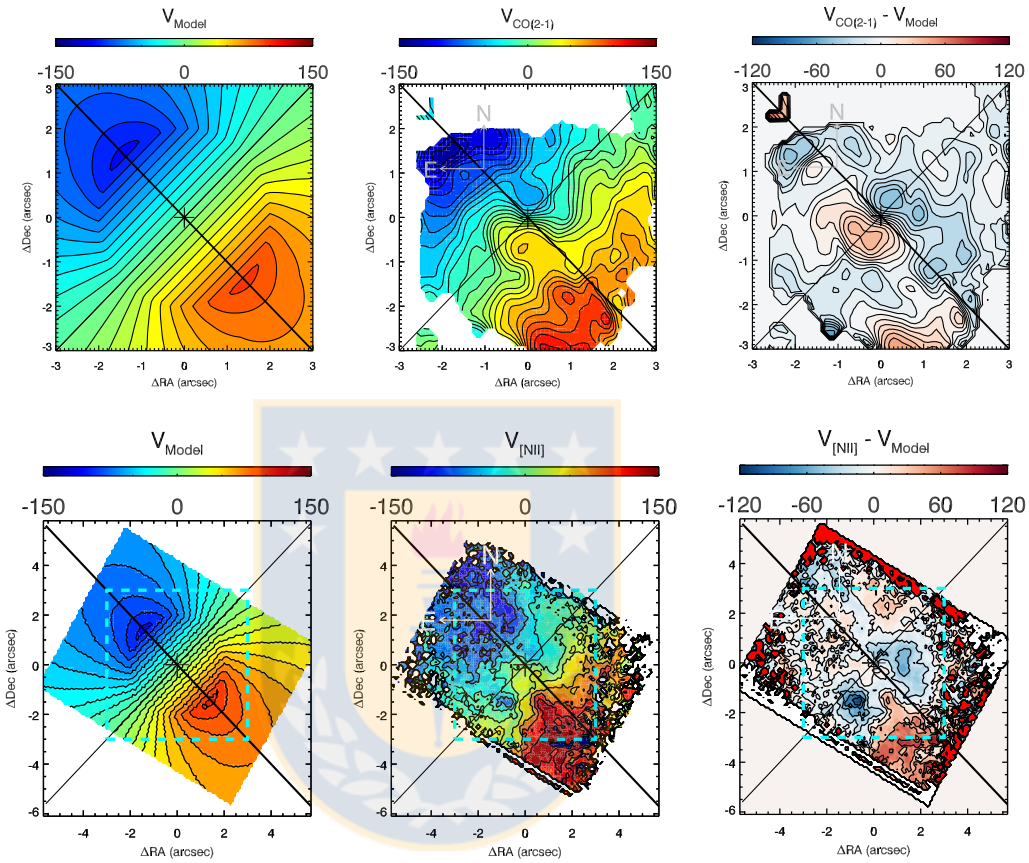

Figure 3.7 The nuclear velocity fields of NGC 1566 and models. The CO J:2-1 (top row) and [NII] 6583Å (bottom row) emission lines, in contours and color following the color bar above each panel. The left column shows the expected radial velocity field from the ModC2014 model (see text), the middle column shows the observed radial velocity, and the right column shows the residual velocities (observed – model). A cyan dashed squares were drawing inside bottom panels for showing the FOV of top panels. In these figures we use a systemic velocity of 1485 km $s^{-1}$and the nuclear position (marked with a cross) is determined by the 230 GHz continuum emission peak. The major (PA=45°) and minor axes are shown in solid lines. One arcsecond corresponds to 48 pc. Source: Slater et al. (2018).

resolution and image fidelity) was noted by C14 and Smajić et al. (2015), but they argued that the small velocities seen in their CO J:3-2 maps made an outflow scenario unlikely. Smajić et al. (2015) have shown that residuals in the nuclear kinematics of the H_2 are consistent with outflows along the minor axis, but that these residuals are also easily explained by deviations introduced by the density waves of the nuclear spiral; non-circular orbits, e.g. a closed elliptical orbit with axes not parallel to one of the symmetry axes (minor or major) can produce residual velocities (Smajić et al., 2015).

We nevertheless argue for the presence of a nuclear outflow (which may of course co-exist with other bar-, warp, or spiral-related perturbations) based on the following reasons: (a) the presence of a nuclear outflow in NGC 1566 is not unexpected as previous studies have claimed kinematic and morphological evidence for the presence of outflows in the NLR (Schmitt & Kinney, 1996; Davies et al., 2016; da Silva et al., 2017), which are most likely to intersect the disk given the observed geometries, and in the larger scale disk (Pence et al., 1990). Note also the evidence of a blueshifted velocity in [OIII]5007Å near the star-forming region ∼1.″5 SW of the nucleus discussed above which da Silva et al. (2017, see their Fig. 20) interpreted as a consequence of contamination from an AGN outflow; we also detect this blue residual in our CO residual (observed − rotation model) velocity map (Fig. 3.7); (b) the unresolved nuclear aperture shows a double peaked profile with Full Width at Zero Intensity (FWZI) ∼200 km s^{-1} (Figs. 3.13 and 3.15), higher than that seen in the lower fidelity maps of C14. If these velocities are attributed to an outflow, the fact that opposite velocities are observed on each side of the nucleus implies that the outflow axis is not aligned with our line of sight. Large angles to the line of sight are unlikely as this would imply extremely high true outflow velocities. An outflow in the plane of the disk would imply an outflow with velocities up to 180 km s^{-1}. Conversely, attributing these observed velocities along the minor axis to other perturbations in the plane of the disk, requires radial velocity perturbations of ∼80–100 km s^{-1} in a nuclear region where the intrinsic (undisturbed) rotation velocities are expected to be $\lesssim$40 km s^{-1}. As we will show in Sect. 3.3.6, our modelling of the bar-related perturbations does not reliably produce both the morphology and the large perturbations seen in the observed velocity field; (c) the pv diagram along the minor axis (bottom right panel of Fig. 3.9) not only shows the high-velocity components (±60–90 km s^{-1}) in the nuclear aperture but also lower brightness emission which connects these high-velocity components to the zero velocity components seen at r∼1.8″ on both sides of the nucleus. To the N (negative

offsets in the bottom right panel of Fig. 3.9) the decrease in velocity in the inner arcsec is clearly seen, and to the S (positive offsets) the decrease is more clearly seen in the r∼1-2″ range. (d) the pv diagrams show velocity deviations which are consistent with radial outflows in the plane of the disk over several PAs (and not just the minor axis) and over apertures at distances of several synthesized beams from the nucleus (see Sect. 3.3.5); (e) as discussed in the next section, the kinematics of the emission line gas in the optical (from GMOS-IFU) are consistent with a nuclear spherical (or bipolar) outflow, which makes the interpretation of a related molecular outflow less surprising. In summary, we support the presence of a nuclear outflow, without ruling out the presence of additional bar- or spiral-related perturbations (Sect. 3.3.6). Other scenarios, e.g., a warped disk or non-coplanar disks (e.g., Wong et al., 2004; García-Burillo et al., 2014) cannot be constrained by us due to the limited resolution, the sparse velocity field, and the lack of a reliable circular rotation model for the galaxy.

This posited molecular outflow is most likely primarily in the disk of the galaxy for the following reasons: (a) outflows outside the disk are often related to nuclear jets (e.g.: Morganti et al., 2013; Sakamoto et al., 2014), but there is no clear evidence for radio-traced jets and outflows in the nucleus of NGC 1566. The potential radio extension in PA 10° (Sect. 3.1) is not aligned with our posited outflow axis. Further, apart from the Seyfert 1 classification there are no data (e.g., maser disks) to constrain the orientation of the central engine; (b) outflows are also often seen perpendicular to the plane of the disk, especially in the case of starburst driven winds (eg., Veilleux & Rupke, 2002; Veilleux et al., 2005; Leroy et al., 2015). However, for such a polar outflow the blueshifted (redshifted) emission would be seen towards the far (near) side of the galaxy disk, the opposite of that seen in NGC 1566; (c) a large (e.g. ¿30°) opening angle for the outflow, often the case in radiation-pressure-, jet-, and starburst-driven outflows will produce a large observed velocity dispersion due to the varying projection angles of the outflowing gas to the line of sight. In NGC 1566 we see a relatively low CO J:2-1 velocity dispersion (FWHM of ∼30 km s^{-1}) in the posited nuclear outflow components (see Figs. 3.6 and 3.15). A spherical outflow scenario can be rejected as this would produce a large velocity dispersion centered on zero velocity, under the assumption of optically-thin emission in CO J:2-1. Note that in Sect. 3.3.4, we argue for the presence of spherical outflow in the ionized gas, which does not contradict our claim that the molecular outflow is in the disk; (d) the posited nuclear outflow has a limited extension, and an apparently decreas-

ing velocity, both of which argue for deceleration of the molecular gas in the high-density medium of the disk; (e) the higher molecular gas density in the disk of the galaxy will make this component more easily detectable in short integrations, as compared to more diffuse molecular gas outside the galaxy disk. In summary, while the molecular outflow could have a larger opening angle (and indeed be isotropic) we appear to be preferentially detecting this component within the galaxy disk.

Is the posited outflow AGN or starburst-driven? As mentioned above, there is no clear evidence of a radio jet, and so any AGN-driven outflow would most likely be due to radiation-pressure. We note that the highest velocities in the outflow are detected at the position of the nucleus and not towards the star-forming knot 1.″5 to the SW. Several authors have presented photometric and kinematic data which argue against the likelihood of a starburst-driven outflow in NGC 1566: Davies et al. (2016) used diagnostic diagrams of [OIII]/Hβ to demonstrate that there is no significant contribution from star-forming regions in the nucleus and it is the radiation pressure from the AGN which dominates in the inner scales. Smajić et al. (2015) present similar diagnostic diagrams using Molecular Hydrogen (H_2) and report an AGN domination for the nuclear region inside 1″ and a relatively modest SFR ($\sim 8 \times 10^{-3}$ [$M_\odot yr^{-1}$]) in the inner 3″, implying a relatively low star-forming efficiency given the observed gas reservoir. Both the galaxy-wide SFR (~4.32 $M_\odot yr^{-1}$; Gruppioni et al., 2016) and the SFR surface density (~0.033 $M_\odot yr^{-1} kpc^{-2}$; Hollyhead et al., 2016) are relatively low, and thus star formation is not expected to drive a nuclear outflow (e.g., Cicone et al., 2014).

As seen in the pv diagrams of Fig. 3.9, a model which sums the ModC2014 model and our empirically derived outflow model (black solid lines in the pv diagrams; see Sect. 3.3.5) provides a much better fit (as compared to a pure rotational model) to the inner 2″ in the pv diagrams at all PAs. Note that our synthesized beam of $\lesssim$0.5 arcsec well resolves the central 4 arcsec of the galaxy (e.g. Fig 3.7). Nevertheless there are several specific features which cannot be fit only with the model of radial outflows (in the galaxy disk) plus rotation, e.g. the apparent morphological double structure of each outflow lobe (Fig. 3.7) and the pv diagram in PA=75° (middle right panel of Fig. 3.9) where observed velocities 1.5–2 arcsec from the nucleus to the E are not well fit by the model. These are discussed in Sect. 3.3.5.

In the residual velocity map of CO (top right panel of Fig. 3.7) the blue- and red-shifted lobes 1″ from the nucleus have a double-peaked morphology. The largest velocity

deviations are along PAs of 100° and 140°, i.e. straddling the minor axis. How can this be explained? Do streaming motions into the nucleus along PA ∼120° create the valley between the two peaks? Further, why is it that almost the entire near side of the galaxy (NE) has a blue residual, while almost the entire far side of the galaxy (SW) has a red residual in the top right panel of Fig. 3.7? This is not due to the use of an incorrect major axis PA (varying the major axis PA does not change these features). Effectively, the NE and SW sides of the galaxy are not axisymmetric in their rotation (see, e.g., Fig. 3.5).

3.3.4 Modeling Observed Velocities: Ionized Gas Outflows?

The [NII] line velocity map was (obtained from the Gauss-Hermite fit version of *profit.pro* after subtracting the broad Hα line emission). The [NII] velocity residual map constructed using the same rotation model used for the CO J:2-1 line at first glance appears morphologically similar to its CO J:2-1 counterpart (bottom panels in Fig. 3.7). However the P.A. of the major axis for the [NII] rotation (especially to the SW) appears to be ∼15° smaller than that used in our model. Further, the [NII] residual velocity map clearly shows blue residual velocities at ∼1–2″ on both sides of the nucleus (with the largest velocity deviation to the SE), in contrast to the CO J:2-1 residual velocity map which clearly shows opposite colors on each side of the nucleus (interpreted above as the sign of a nuclear molecular outflow in the disk).

In the [NII] velocity residual map, the blue region on the near side of the galaxy (NW of the nucleus) is in rough agreement with the equivalent blue region in the CO J:2-1 residual map, and thus would be consistent with the outflow scenario posited for the CO J:2-1 data. On the other hand, the blue region in the [NII] velocity residual map on the far side of the galaxy (SE of the nucleus) is located along the minor axis at ∼1.″8 from the nucleus: this does not match the feature seen in the CO J:2-1 residual map which is closer to the nucleus (∼1″) and redshifted. Note that this blue SE feature in the [NII] residual velocity map is roughly cospatial with a region of high dust extinction (structure map in Fig. 3.3). A red region closer to the nucleus matches with the red region to the SE seen in the CO residual map, however, this consists in redshifted radial velocities around 10 km s^{-1} which is too low to be considered significant as a part of an outflowing gas. There is another small region to the SW at ∼2″ which is redshifted and around 50 km s^{-1} but in spite of having a similar dynamic range, it does not match with the redshifted outflow region to the SE in the ALMA residual map (∼1.″5), being placed too close to the

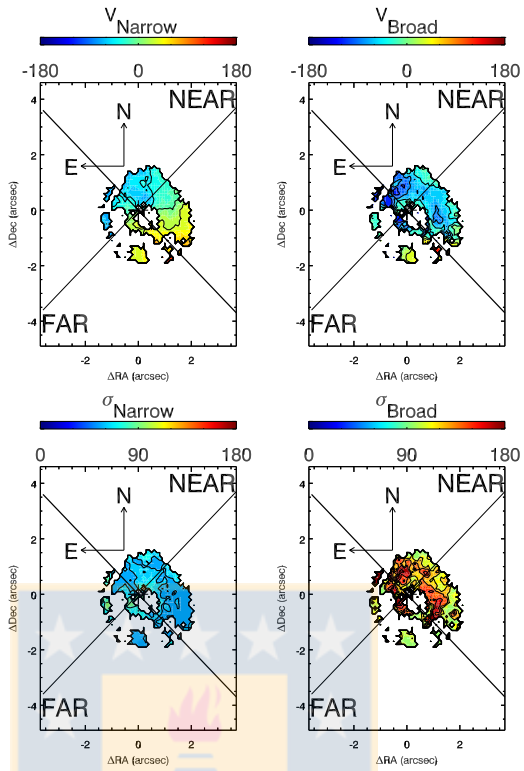

Figure 3.8 Maps of the narrow and broad components of [NII] in NGC 1566. The velocity and dispersion maps of the [NII] emission line obtained from the two-Gaussian fit version of *profit.pro*. Top panels: from left to right, the velocity and velocity dispersion maps of the narrow and broad components, respectively. Bottom panels: the velocity dispersion maps of the narrow (left panel) and broad (right panel) components. Source: Slater et al. (2018).

star-forming region.

The [NII] emission in the inner ∼2″ is double-peaked, and thus cannot be well fit with a single Gauss-Hermite polynomial. We, therefore, used the two Gaussian fit version of *profit.pro* to search for potential independent velocity components in the [NII] emission line. Meaningful two-component fits were obtained in part of the inner 3″ radii nuclear region and the resulting velocity maps are shown in Fig. 3.8. These maps include only pixels for which a double component fit produced a meaningful result. For regions where the two-component fit was not possible, the single component fit remains valid. Note that in the latter case the single component fit shows primarily the equivalent of the narrow component but in a few regions the velocity dispersion of the single component fit is similar to that of the broad component of the two-component fit. The two-component fit is

mainly obtained near the nucleus and on the near side of the galaxy. On the far side (and a small nuclear region to the W on the near side), the regions in which a two component fit is not possible coincide well with the regions of high dust extinction. The 'narrow component' shows velocity dispersions ranging between 60 and 90 km s^{-1} (bottom left panel of the figure) and the velocity field of this component mainly follows that expected from our rotation model. The second component, which we refer to as the 'broad component', shows velocity dispersions of ∼140–160 km s^{-1} (bottom right panel of the figure) and does not appear to participate in regular rotation.

The strong blue residual region to the SE in the single component [NII] residual velocity map is not fit with a double component. The weaker blue residual region to the NW in the single component [NII] residual velocity map is now seen to be blue in its broad component only; in its narrow component this region follows regular rotation. Note that both blue knots do not correspond to regions of high dust columns in the structure map.

Based on the velocity field of the broad component of the two component fit to [NII], the velocity field of the high dispersion ($\gtrsim$120 km s^{-1}) areas in the single component fit to [NII] and the distribution of the nuclear dust, we postulate the presence of an expanding sphere of ionized gas, i.e. a spherical ionized outflow, for the reasons given below. With the presence of dust (dominantly in the plane of the galaxy disk) we would preferably see emission from the hemisphere in front of the galaxy and moving towards us, i.e. blueshifted radial velocities. In the absence of dust one would expect a large dispersion and a median velocity close to systemic. Note that given the relatively low inclination of NGC 1566 (33°), dust in the inner 2″ (∼100 pc) of the disk produce an almost equal extinction of light from the bulge for both the 'near' and 'far' side of the galaxy disk. This is clear in the structure map where dark dust lanes are seen on both the near and far sides in the inner ∼2″. Only at larger radii are the structures of the dust lanes more prominent on the near side of the galaxy disk. In the case of NGC 1566 we do not obtain a two-component fit in areas where the structure map implies marked dust lanes (non-intuitively these are on the far side of the galaxy disk in the innermost arcsec) and find large blue shifts in the broad component of the two-component fit on the near side of the galaxy disk in areas where the structure map shows less marked dust lanes. Further, the maps derived from the single component fit to the [NII] line (Fig. 3.3) show two regions of high dispersion, about 2″ from the nucleus to the SE (the blue knot referred to above) and to the NE. These two regions effectively correspond to the broad component, and are

also blue in their velocity. Thus we effectively see blue velocities in the broad component in almost every compass direction implying a spherical outflow in the inner ∼2″ which is visible to us primarily in areas of lower dust extinction. Similar kinematic signatures, and thus interpretations, were observed and used in previous IFU studies, e.g. in the nearby Seyfert galaxy NGC 2110 (Schnorr-Müller et al., 2014b), and in some radio-quiet quasars (Liu et al., 2013). Nevertheless, despite all these signs, we are not neglecting a potential presence of a bipolar outflow. Namely, it might be reasonable to think that what we see as a spherical outflow might be instead ionized gas ejected from the nucleus in opposite directions but we notice just a part of them as a consequence of a poor resolution in the GMOS data (∼0.5–0.6″).

We note that our postulation of this spherical outflow of ionized gas does not contradict our postulation of cold molecular gas outflows in the galaxy disk. The cold molecular gas outflows are expected to be preferentially detected in the plane of the disk for two reasons: a low density CO outflow would be optically thin and its profile would thus be centered on zero velocity and the significantly larger abundance of molecular gas in the disk as opposed to above the disk, makes the disk molecular gas much easier to detect.

3.3.5 Observed Position-Velocity (pv) Diagrams: ALMA

In this section we present position-velocity (pv) diagrams for the CO J:2-1 line. These pv diagrams were extracted from the ALMA datacubes using a slitwidth of 0.2″; they are thus limited in spatial resolution by the intrinsic resolution of the images (∼0.″4). Fig. 3.9 shows the pv diagrams along the major axis, minor axis, the large scale bar, and other relevant PAs including PA=115° (20° from the minor axis) for a direct comparison with the pv diagram of CO and Hα in Fig. 3 of Agüero et al. (2004). In their figure, the 'Blueshifted Knot' which they interpret as inflow motion is clearly seen in our CO J:2-1 pv diagram.

In each pv diagram we have overlaid the predictions of solid body rotation (white dashed line), the ModC2014 model (purple dashed line), and the sum of the ModC2014 model with our outflow model (solid black line). The solid body rotation and ModC2014 are essentially the same over the inner ±3 arcsec, after which the latter flattens in velocity. Our outflow model was derived as follows: we used the pv diagram along the minor axis (bottom right panel of Fig. 3.9) to measure the radial velocity of the brightest CO emission at a given distance from the nucleus on both the NW (positive offsets in the pv

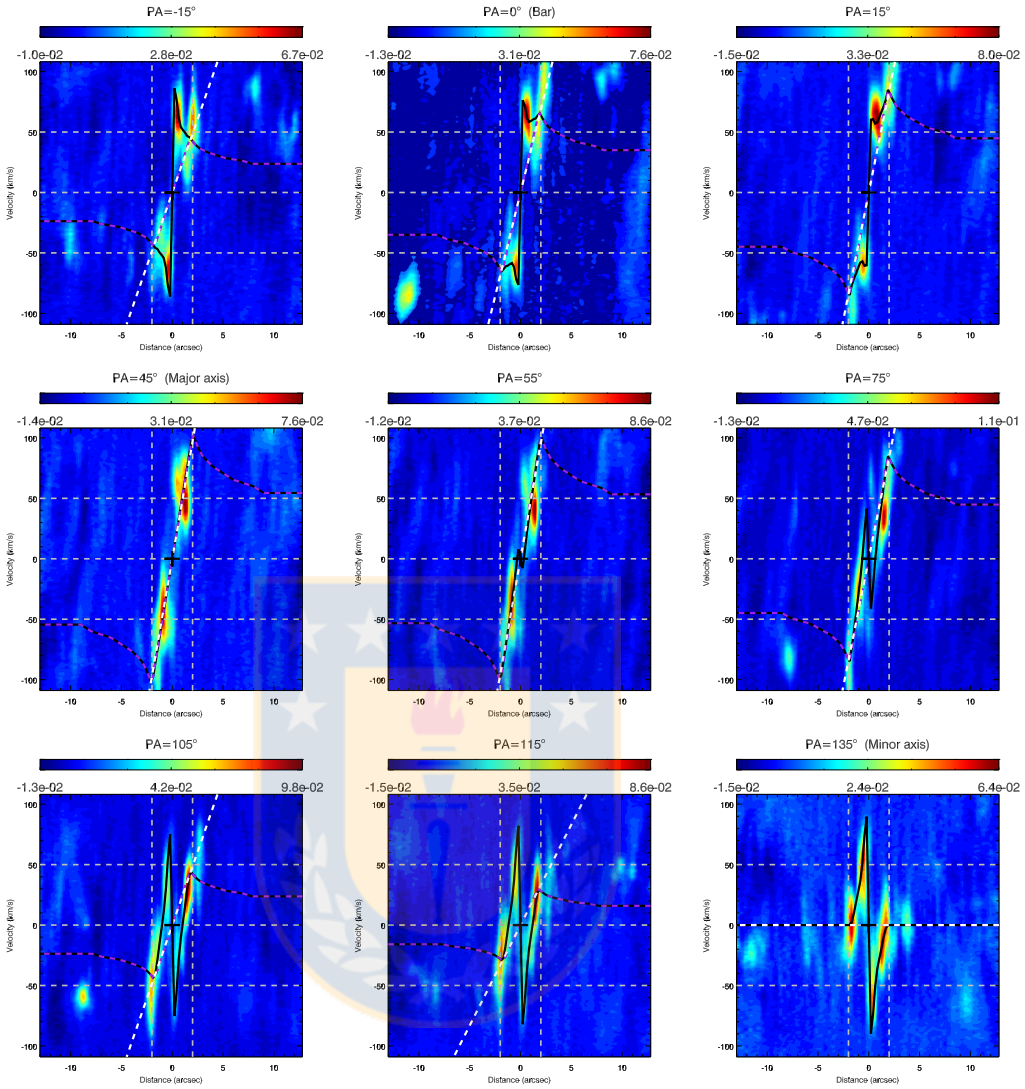

Figure 3.9 PV diagrams of CO J:2-1 in NGC 1566 at several position angles. The CO J:2-1 emission in NGC 1566 along several PAs are shown in color following the color bar above each panel. The PA of the 'slit' over which the pv diagram was extracted is indicated above each panel, as are the PAs corresponding to the major and minor axis of the galaxy, and of the large scale bar. Negative offsets on the x-axis correspond to the PA listed above the panel, i.e. positive offsets are along the 180° plus the listed PA. The black cross indicates the position of the 230 GHz continuum peak (presumed to be the galaxy center) and the systemic velocity of the CO J:2-1 line (1485 km s^{-1}). To guide the eye horizontal and vertical lines delineate ±2 arcsec from the nucleus and ±50 km s^{-1} from the systemic velocity. The dashed white and purple lines are the solid body rotation model and the ModC2014 rotation model, respectively. The solid black line shows the expectation of adding our outflow model to the ModC2014 model (see Sect 3.3.3). The pv diagrams, were created from a 'hybrid' datacube: the inner $\sim 12'' \times 12''$ square region centered on the nucleus is taken from a high resolution (Briggs weighting, Robust=−2) map with spatial resolution $0\farcs52 \times 0\farcs35$ and an r.m.s. noise of 0.1 mJy/beam per channel (up to 2 mJy/beam per channel in channels with strong signal), while the rest of the cube is from a higher signal to noise (Briggs weighting, Robust=2) map with spatial resolution $0\farcs6 \times 0\farcs5$ and an r.m.s. noise of 1.2 mJy/beam per channel (up to 4 mJy/beam per channel in channels with strong signal). Source: Slater et al. (2018).

diagram) and SE sides. The absolute values of these velocities as a function of distance from the nucleus were then interpolated and deprojected (assuming that the outflow is in the disk) to construct a function of outflow velocity vs. position. As seen in the bottom right panel of Fig. 3.9 the redshifted 'outflow' velocities provided more constraints closest to the nucleus and the blueshifted velocities provided better constraints at slightly larger distances. The final outflow model starts with outflow velocities in the disk of 157 km s^{-1} at the (unresolved) nucleus and decreases monotonically to zero velocity 2″ from the nucleus.

First concentrating on the pv diagram along the minor axis in Fig. 3.9, we see that the NW side of the minor axis shows a clear deceleration in velocities when going from 1″ to 2″ from the nucleus, while the SE side the bright emission at 1.5–2″ (the inner spiral arm) shows a larger velocity dispersion which does not clearly vary with distance. However, this SE side shows a clearer decrease in velocities between 0 and 1″. A similar scenario has been reported in NGC 1068 for both hot and cold molecular gas (Barbosa et al., 2014; García-Burillo et al., 2014, respectively); outflowing nuclear molecular gas, with outflow velocity decelerating from 200 km s^{-1} to 0, accumulates in an off-centered ring 100 pc from the nucleus (Barbosa et al., 2014).

For the pv diagram along PA=0, which is aligned with the large scale bar in NGC 1566, we see (1) gas consistent with outflows, which is well fit by our outflow model; (2) gas which is almost in rotation 1–2″from the nucleus on either side, but showing a steeper rotation curve which reaches zero velocity at a position offset from the center.

For the pv diagram along the major axis (PA 45°), several velocity components can be seen. These include gas in rotation, and some contamination from the disk outflow component, since at the nucleus, the 'slit' (limited by the spatial resolution of our ALMA observations) expectedly picks up the gas outflowing along the minor axis and other angles. Moreover, gas in the inner spiral to the NE is preferentially redshifted and gas in the inner spiral to the SW is preferentially blueshifted, i.e. both spirals show ∼40 km s^{-1} (in projection) deviations towards values of zero velocity: the most obvious interpretation of this is that gas originally in circular rotation is slowed down on hitting the ends of the nuclear molecular gas 'bar'. This loss of momentum could potentially result in inflows. Similar velocity offsets are also seen at slit PAs offset 10° from the major axis (e.g. PA=55°; Fig. 3.9), and is very dramatic on the SW side in the pv diagram with slit PA=75°, at the point where an outer spiral pattern breaks off from the inner spiral pattern.

Molecular gas in the inner spirals always show a large velocity dispersion (around ~80 km s^{-1}). The inner spiral to the NW (about 1 arcsec from the nucleus) always show velocities which are bluer than that expected from rotation or rotation+outflow. This is clearly seen in all pv diagrams which intersect this arm (e.g. PAs 45°, 55°, 75°). The opposite inner spiral (that to the SE) shows the opposite, i.e. velocities redder than expected from rotation and rotation+outflow (e.g. most obvious in the PA 105° and 115° pv diagrams) but this velocity offset is not as well defined as in the case of the NW arm. Given that the NW arm is mainly on the near side of the galaxy disk and the E arm is on the far side, this is what would be expected from a streaming outflows along the spiral rather than streaming inflows! We speculate that these structures are absorbing the momentum of the nuclear outflow and thus heating up and expanding.

Another region which consistently shows large differences from the rotation+outflow model is the double cavity (between the nuclear bar-like structure and the inner spiral arms) to the NW and SE, for offsets of 1 to 2 arcsec from the nucleus. When the slit passes through these cavities the pv diagrams (especially those at PA=0, and PA=−15°) show a characteristic pattern which can be explained by slower than rotation velocity between 1 and 2 arcsec (but increasing in the correct sense), and a large dispersion of velocities (all larger than those expected from rotation) at 2 arcsec.

While the predictions of our rotation plus outflow model are in general consistent with the position velocity data at different PAs especially in the inner 2″, at PAs close to 0° (see the pv diagrams at PA=0°,−15° and 15°) one can see significant differences between the data and models in the inner 1.″5. Here we clearly see a component of gas which follows a steep velocity gradient decreasing to zero velocity at a distance of 1.″5 from the nucleus on both sides. One potential explanation for this anomalous rotation is an inner counter rotating gas disk with major axis in PA~0, fed by gas inflowing along the large scale bar. This possibility is motivated by observational evidence that bars are an efficient pathway for transporting gas from galactic scales to nuclear scales in both active and inactive barred galaxies (Sakamoto et al., 1999; Crenshaw et al., 2003; Regan & Teuben, 2004; Sheth et al., 2005). Alternatively, these features are a consequence of perturbations due to the bar, as discussed in the next section.

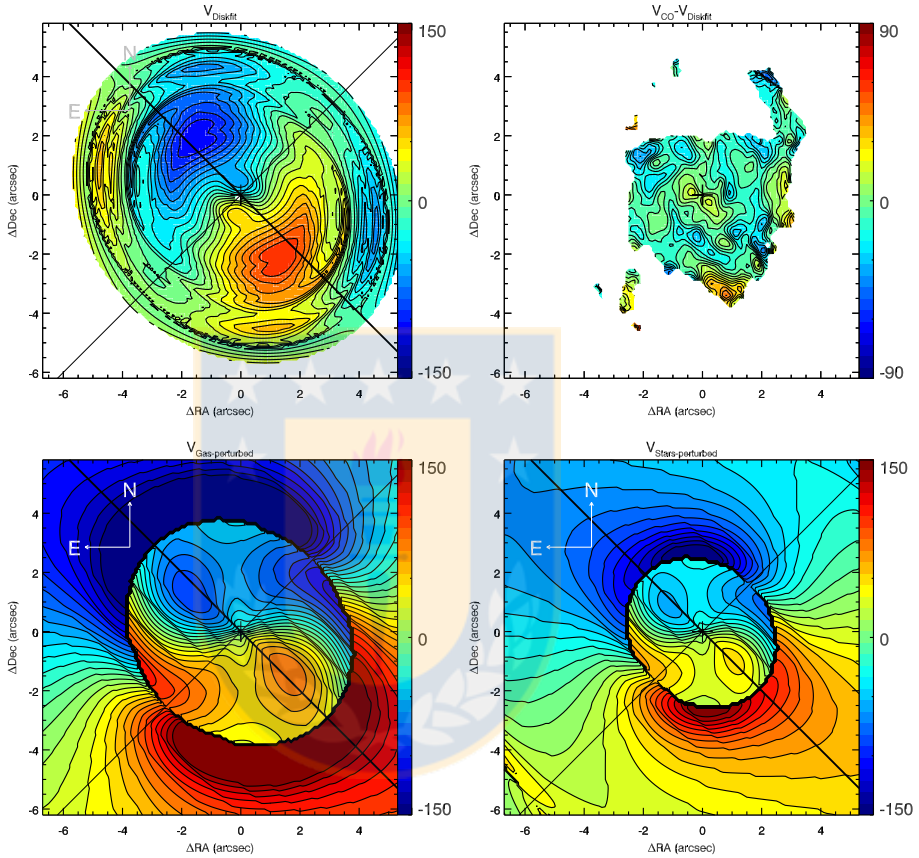

Figure 3.10 Bar-perturbed models; *Diskfit* and customized models for NGC 1566. **Top:** *Diskfit* model, with perturbations from a bar at PA 0°, fit to the CO velocity field (left panel) and the resulting residual CO velocity field (observed − model) (right panel). **Bottom:** illustrative bar-perturbed velocity fields resulting from our linearized epicyclic perturbation models (see text) and using $\lambda = 0.2$ and $\Omega = 120 \mathrm{kms}^{-1}\mathrm{kpc}$. The left (right) panel shows the results when setting the intrinsic rotation curve as that from C14 (our Bertola model fit to the stellar velocity field). Source: Slater et al. (2018).

3.3.6 Modelling Observed Velocities: Bar perturbations

Velocity perturbations due to bar(s) are believed to play an important role in fueling the SMBH and in triggering nuclear star formation. It is well known that NGC 1566 hosts an intermediate strength nuclear bar with radius ∼1.7 kpc in PA≈0 (Hackwell & Schweizer, 1983; Pence et al., 1990; Mulchaey et al., 1997; Agüero et al., 2004; Dicaire et al., 2008; Comerón et al., 2010; Kendall et al., 2011, C14), which could be largely responsible for the velocity perturbations seen in the molecular gas. C14 used torque maps to show that the asymmetries in the velocity field of the nuclear molecular gas are predominantly produced by the bar. They also briefly explore estimates for the bar pattern speed. However, they did not make a detailed kinematic analysis of the bar-produced perturbations.

To analyze the effect of bar-produced perturbations we use both *Diskfit* (Spekkens & Sellwood, 2007) and our own Fourier component decomposition software (Finlez et al., in prep.) based on the the linear perturbation analysis described in Wong et al. (2004); Fathi (2004).

The *Diskfit*[8] package can be used to fit both the image and the velocity field of a galaxy. In imaging mode, an input image is fit with one or more of a bulge, disk, and bar, resulting in estimates of the relative flux and morphology (ellipticity, brightness profile, and PA) of each component. In velocity mode, *Diskfit* models asymmetric rotation-dominated velocity fields using a combination of tangential and radial perturbations to a fitted circular velocity model. We fit our CO J:2-1 velocity field using *Diskfit* considering only m=2 potential perturbation (i.e. bars) modes and using the galaxy nuclear position, galaxy PA, galaxy inclination and bar PA as fixed values (mm continuum peak position, 45°,33°, and 0°, respectively). The best fit model obtained by *Diskfit*, and the velocity residuals (observed − Diskfit model) are shown in the top panels of Fig. 3.10. The best fit model from *Diskfit* differs from our toy rotation model (Fig. 3.7, top left and Sect. 3.3.2) in that the apparent rotation axis moves to a slightly smaller PA in the inner 4″, the inner 1″ shows twisted isophotes, and there is a resonance at ∼4″, which mainly falls in a region where we do not have observed velocities due to low signal to noise.

The residual velocity map obtained after subtracting the *Diskfit* (Fig. 3.10 top right panel) shows smaller deviations from systemic as compared to the velocity residual made from our rotation-only model (top right panel of Fig. 3.7), especially to the SE of the nucleus, and in general in the inner arcsecs. However, the *Diskfit* model still does not attain the highest velocities seen in the inner arcsecs. We note that *Diskfit* only allows us

[8] http://3w.physics.queensu.ca/Astro/people/Kristine_Spekkens/diskfit/

to change basic photometric parameters of the galaxy, e.g., disk PA and inclination and bar PA, and the input observed velocity field. Since all these are relatively well defined for NGC 1566, we are unable to further fine-tune the results of *Diskfit*.

To better illustrate the differences between the *Diskfit* model and the observed velocity field, we plot the *Diskfit* model (orange lines) on the observed pv diagrams at several relevant PAs (Fig. 3.12). We immediately note that the best-fit *Diskfit* model was derived from the velocity field (intensity weighted average velocity at each spatial pixel) rather than the full datacube, so that comparing the model directly to the pv diagram is not really fair. Instead it is more correct to compare the model (orange lines) with the velocities from the moment 1 map (intensity weighted velocity; black dashed lines in the figure). While the *Diskfit* model slightly overpredicts the velocities seen along the major axis (top right panel), and the pattern of the velocities seen along the minor axis (bottom middle panel), it fails to predict (by a factor $\sim$2) the large peak velocities seen along the minor axis (PA=135°), or along PAs 0° and $-15°$. That is, the bar perturbations are unable to explain the $\sim$90 km s^{-1} radial velocities seen in the inner 1″ to the NW and SE of the nucleus.

While *Diskfit* models the observed velocity field with a base rotation model plus perturbations in radial and tangential velocities (one component each in the case of m=2 modes), it does not use (or at least does not provide details to the user) a physically-based model with, e.g., a mass-based rotation curve or a fixed bar pattern speed. We thus additionally model the observed CO velocity field with linearized epicyclic perturbations produced by a bar (for details see, e.g., Wong et al., 2004; Fathi, 2004) applied to a physically derived rotation curve (an exponential disk whose mass is constrained by near-IR photometry) for a given bar pattern speed (Ω), damping factor (associated to a frictional force; λ), and bar PA and ellipticity (Finlez et al., in prep.). Our code is based on the algorithms proposed in Franx et al. (1994), Wong et al. (2004) and Fathi (2004). Note that we specifically use the 'm=2' potential (relevant for bars) which introduces changes in the 1st and 3rd harmonic coefficients (Schoenmakers et al., 1997), and that this perturbation analysis is valid only for 'weak' bars, i.e. when the bar potential does not dominate the disk potential).

We used *Diskfit* to decompose an IRAC 3.6μ image of NGC 1566, obtained from NED, into bulge, disk, and bar components. The galaxy and bar PAs were fixed and other parameters allowed to vary. We further assume a constant mass to light (M/L) ratio for all three components. We find that the disk contains 58% of the total mass (light)

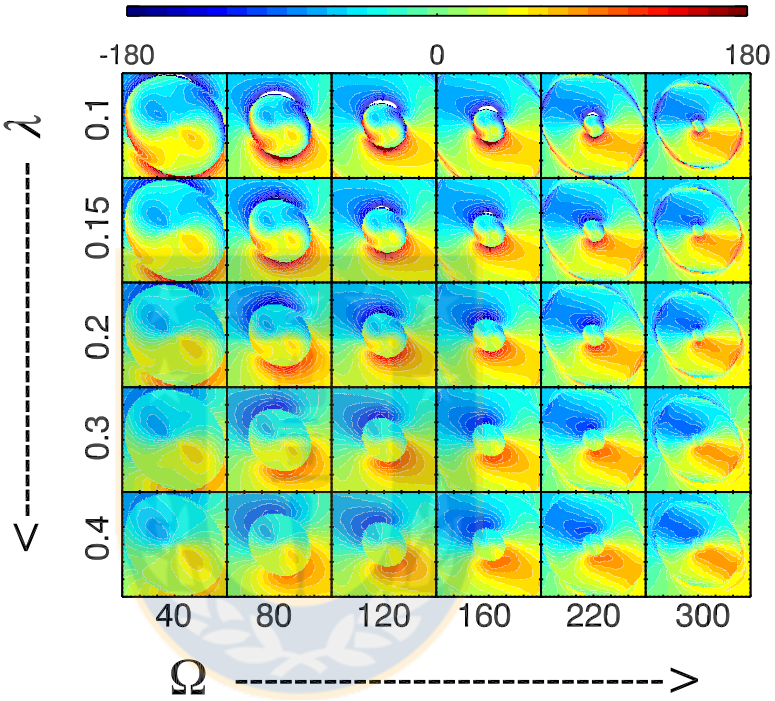

Figure 3.11 Several bar-perturbed models of NGC 1566. The bar-perturbed velocity fields were obtained with our epicyclic perturbation models applied to our best fit Bertola stellar rotation curve (see text), on varying the bar pattern speed (left to right; Ω in units of km s^{-1} kpc^{-1}) and the dimensionless damping parameter (top to bottom; λ). The FOV of each image is $12'' \times 12''$and major tick marks are shown every $1''$. All velocities follow the same color bar shown on the top. Source: Slater et al. (2018).

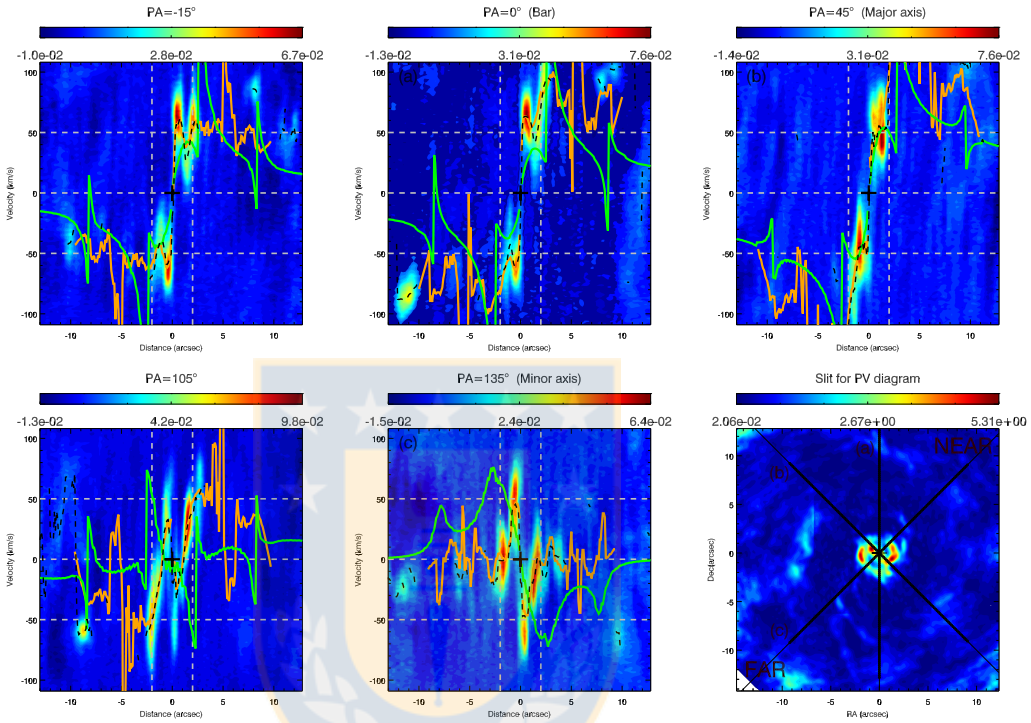

Figure 3.12 PV diagrams of NGC 1566 with bar-perturbed models overplotted. Same as Fig. 3.9, but here the overplotted lines show the velocity of the corresponding pixel in the CO moment 1 map (dashed black lines; i.e. the flux-weighted average velocity at a given pixel), the best-fit velocity field from *Diskfit* (solid orange line), and for comparison the λ=0.2 and Ω=120kms^{-1}kpc model from our linear perturbation analysis (bottom right panel of Fig. 3.10; solid green line). To better trace the highest velocity components in the CO moment 1 (velocity) map, we used a cutoff of 8mJy/beam/channel ($\sim 4\sigma$) to create the moment 1 map which is overplotted here and used as the input map to *Diskfit*. The PA of the 'slit' along which the pv diagram was extracted is marked above each panel. The bottom right panel shows the moment 0 map of CO J:2-1 together with the positions of the slits used to create the pv-diagrams in the upper row panels. Source: Slater et al. (2018).

of NGC 1566 with a bar to disk mass ratio of 0.7. Given the total mass of NGC 1566 derived by Sheth et al. (2010), the disk mass is $2.2\times10^{10}[M_{\odot}]$. Alternatively, the 3.6μ disk luminosity with a $M/L_{3.6\mu}$ ratio of 0.47 (McGaugh & Schombert, 2014) implies a disk mass of $4.4\times10^{9}[\mathrm{M}_{\odot}]$. An exponential disk with these total masses was then used to derive a first-guess intrinsic (i.e. before bar perturbations) axisymmetric rotation curve (details in Finlez et al., in prep.). The disk mass was then slightly adjusted (to $6\times10^{9}[\mathrm{M}_{\odot}]$) in order to better fit (by eye) the model rotation curve of the CO in the inner disk (i.e. ModC2014) or $\sim 2\times10^{9}[\mathrm{M}_{\odot}]$ to agree with our best-fit Bertola model Bertola et al. (1991, Eq. 2) to the stellar velocity field. Note that these masses are an order of magnitude lower than that predicted by Korchagin et al. (2000) ($1.78\times10^{10}[\mathrm{M}_{\odot}]$).

We then ran our linear perturbation code, in m=2 mode, using as inputs the intrinsic axisymmetric rotation curve(s) derived above, the PAs of the galaxy disk and bar, and the bar ellipticity ($\epsilon = 0.42$), the latter derived from our *Diskfit* decomposition. The bar pattern speed (Ω) and the damping factor (λ) were allowed to vary. The resultant model velocity fields for a range of values of Ω and λ, when using the best-fit Bertola model of the stellar velocity field, are shown in Fig. 3.11. The most notable effect of varying Ω is the change in the radii of the resonances. Gas orbits change abruptly when crossing these resonances; the effect of increasing damping (increasing λ) is to smooth out these large swings in the orbits. Most of the panels in Fig. 3.11 show the characteristic 'butterfly' pattern expected from bar perturbations. However, for this butterfly pattern to fall within the central $\sim2''$ as observed, i.e. to explain the innermost high velocity features, one requires extremely high ($\sim$300 km s^{-1} kpc^{-1}) bar pattern speeds. Alternatively, the intrinsic rotation curve requires to rise slower or flatten at lower velocities. We must note that the uncertainty in the distance to NGC 1566 (see Sect. 1) plays a significant role in the bar pattern speeds used here. If a distance of 20 Mpc is used for NGC 1566 then the bar pattern speeds we list here would halve, so that less extreme bar pattern speeds could replicate the observed resonances. In any case, even if the resonance radii are matched, the pattern of the model velocities are significantly different from the observed CO velocity field (and the larger scale Hα velocity field from Pence et al. (1990): specifically at higher pattern speeds the strongest perturbations inside the inner resonance are in PA $\sim100^{\circ}$, offset from the PA of our posited outflow, and beyond the inner resonance the kinematic axis of is highly curved, starting at PA ~0 and then curving to the observed PA of the galaxy.

For illustration, we compare the predictions of the perturbation model which uses the Bertola best fit model to the stellar velocity field as the intrinsic rotation curve, and parameters $\Omega = 120$ [km s^{-1}kpc^{-1}] and $\lambda = 0.2$ (the model shown in the third row, third column of Fig. 3.11) with our observed pv diagrams in Fig 3.12. While this model does not well fit the observed velocity field, it uses a pattern speed argued for in C14 (based on corotation placed at the bar end) and a damping parameter within the range of values typically invoked for other well studied galaxies (between 0–0.5 Wada, 1994; Fathi et al., 2005), and is thus a good reference point.

As a further illustration, the bar-perturbed velocity fields for $\Omega = 120$ [km s^{-1}kpc], $\lambda = 0.2$, and for both options of the intrinsic rotation curve (gas- and stellar-rotation curve models) are shown in bottom panels of Fig. 3.10. The model which uses an intrinsic rotation curve similar to that of the gas (bottom left) exhibits a resonance at $\sim 4''$, similar to that obtained by *Diskfit* (left top), but presents less pronounced nuclear distortions as compared to the *Diskfit* model. Using the slower rising Bertola (stellar velocity) model as the intrinsic rotation model (bottom right) changes the position of the resonance to ($\sim 2.6''$), but also gives lower velocity distortions along the minor axis, or rather the higher velocities seen in the observed velocity field ($\sim 1''$) are further out in the model ($\sim 3''$): therefore, to spatially matching these velocity distortions requires higher bar pattern speeds or a slower rise in the intrinsic axisymmetric rotation curve. Apart from the mismatch in resonance radii, these two panels also clearly illustrate the mismatch between the observed and modelled velocity fields noted above; specifically, the misalignment of kinematic axes inside the resonance (related to the posited outflow), and the large curvature in the kinematic axis beyond the inner resonance.

Overall, we are unable to convincingly fit the observed CO kinematics with perturbations produced by the large scale bar. Our linearized epicyclical bar perturbation models, which use realistic values for the intrinsic rotation curves and the bar pattern speed (with the caveat of the uncertainty in the distance to NGC 1566), are able to reproduce the amplitudes of the inner perturbations. However, the resonances are produced further out than observed, and the velocity changes are not as sharp as observed. Higher bar pattern speeds, perturbations by an inner bar in a different PA, or different intrinsic rotation curves, would be required. *Diskfit* reproduces reasonably many of the observed features in the velocity map, and at first glance provides a reasonable explanation for the perturbations observed, even if the amplitude of these perturbations is not as high as observed.

However, we are wary of the results of *Diskfit* for two main reasons. First, *Diskfit* does not provide feedback on the underlying physical parameters of the resultant model, and thus, e.g., we are unable to evaluate whether the bar pattern speed used is physical and second, we have applied *Diskfit* to about a dozen galaxies for which we have disturbed optical emission line kinematics over the inner 5″ of the galaxy and almost always found relatively good fits (Schnorr-Muller, priv. communication), even though our detailed multi-component analysis either found the perturbations to be due to bars (Schnorr-Müller et al., 2017b) or outflows and/or streaming inflows (most other cases, e.g., Schnorr-Müller et al., 2017a). In fact, Spekkens & Sellwood (2007) obtained a good fit to the velocity field in NGC2976, but to conclude that the perturbations were due to the bar, they confirm their existence at the PA predicted by the model, according previous photometry. This consistently good performance of *Diskfit* makes it more difficult to believe that the fits are truly consistent and physically motivated rather than empirical best fits to distorted velocity fields. We emphasize that we are not stating that bar-related perturbations do not exist in the velocity field, rather we argue that bar-related perturbations are not the unique and dominant driver of the observed nuclear perturbations in the CO velocity maps, and it is most likely that the nuclear perturbations are produced by an AGN-driven outflow.

3.3.7 Modeling Observed Velocities: CO J:2-1 Streaming?

The presence of putative outflows and/or bar related perturbations (previous sections) makes it difficult to search for signatures of streaming motions in the inner few arcsec in velocity maps or even residual velocity maps (e.g. Fig. 3.7). That is, since the velocity maps show the intensity weighted average velocity of the spectrum corresponding to each spatial pixel, they are likely dominated by the 'outflow' signature in the inner $\sim 3''$. Further, when the intensity of the gas in rotation dominates that of the gas in inflow, velocity residual maps will not show strong indications of the inflow. It is thus important to examine the velocity profile of each pixel or aperture in order to separate outflows, rotation, and streaming inflows. Ideally, one requires a complete velocity field to analyze the azimuthal average of radial gas velocities at each radius. While this is often possible in the case of ionized gas, molecular gas is often detected only over a limited range of azimuths at each radius. In the case of NGC 1566, our CO velocity maps are 'complete' out to a radius of $\sim 3''$, beyond which the velocity filling factor is ~5–40%. Under the assumption that these detected CO regions dominate the CO flux at their respective radii, the detected

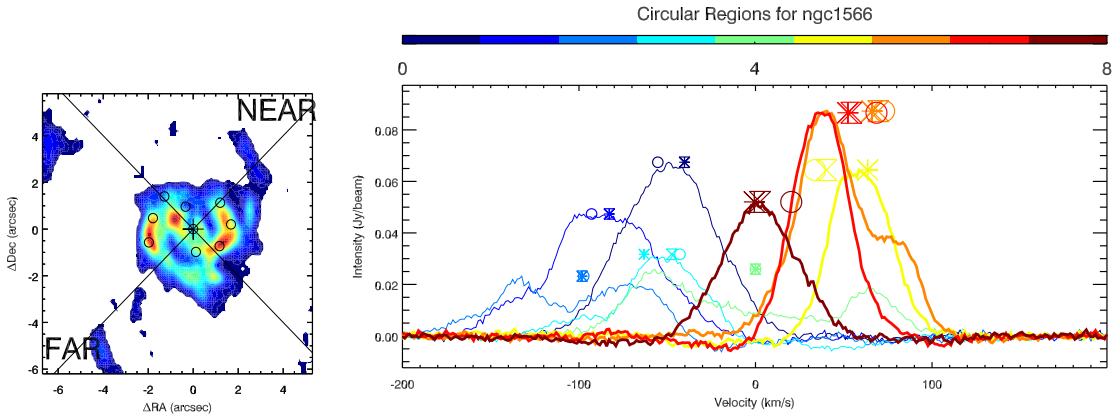

Figure 3.13 CO spectra in apertures along the inner spiral arms of NGC 1566. The left panel shows the location of each circular aperture (0.″2 in radius) overlaid on the CO flux map. For reference, the center of the galaxy, major axis, and the near and far sides of the disk, are indicated. Apertures are numbered 0 to 8 with aperture 0 being the farthest aperture on the E arm, aperture 4 the nuclear one, and aperture 8 the farthest aperture on the W arm. The right panel shows the extracted CO J:2-1 spectra; thick lines are used for the spectra corresponding to apertures from the W arm (Apertures 5 to 8), and different colors are used for each spectrum, following the color bar on top of the panel. Symbols with the corresponding color (plotted at the y value of the peak flux density of the spectrum) denote the radial velocities expected in that aperture for our rotation model (hourglasses), our outflows + rotation model (asterisks), and our rotation plus radial streaming inflow model (open circles). In some apertures, adding outflows and/or streaming inflows does not change the predicted radial velocity; this is a result of projection effects and/or the fact that our outflow model has zero velocity beyond ∼2″ from the nucleus. Source: Slater et al. (2018).

clumps or arms can still be used to constrain the presence of streaming flows. Given the above, we model streaming inflows with a very simple toy model in which the inflow is assumed to have a constant radial inflow velocity (which we fix to 50 km s^{-1} after initial inspection of the results). This velocity is then projected and added to the projected radial velocity expected from our rotational model. We first examine the spectral profiles in apertures along the inner spiral arms (left panel of Fig. 3.13). The CO J:2-1 spectra extracted from these apertures are shown in the right panel of Fig. 3.13, together with the average radial velocities expected from our models of rotation, outflows, and streaming (and combinations thereof).

Analyzing the CO J:2-1 spectra in the right panel of Fig. 3.13 we see the following: (a) The nuclear spectrum (light green) is clearly double peaked: the peaks at V_{rad} ≈65 km s^{-1} are attributed to putative nuclear outflows (previous sub-sections), and the highest veloci-

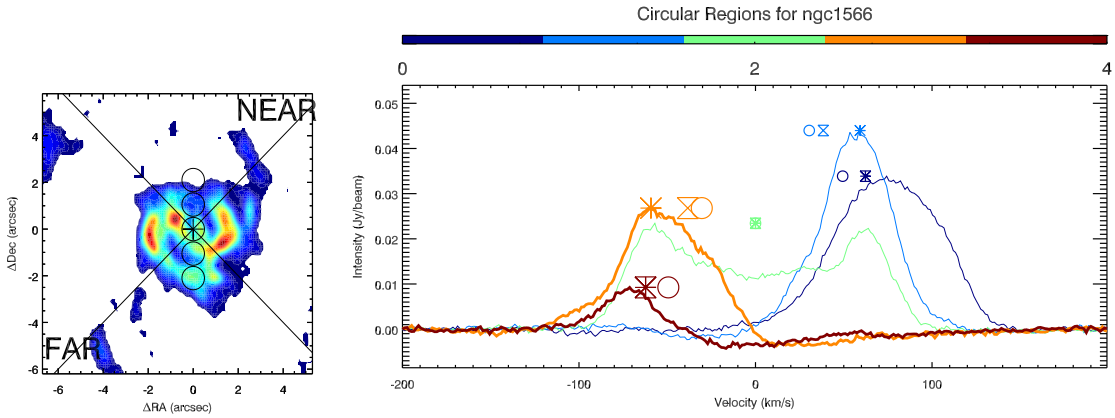

Figure 3.14 CO spectra in apertures along the large scale bar of NGC 1566. Same as Fig. 3.13, but for apertures oriented along the bar. Apertures are numbered 0 (southernmost) to 4 (northernmost), and apertures here are each 0.″5 in radius. Source: Slater et al. (2018).

ties seen are V_{rad} ≈100 km s^{-1}. Note that there is a plateau of CO J:2-1 emission at lower velocities, potentially from gas rotating in the disk (recall that our rotation models predict velocities of V_{rad} ≈0–50 km s^{-1}within this aperture). (b) The off-nuclear apertures show profiles with varied shapes and widths, and the off-nuclear apertures which intersect the galaxy major axis clearly show multiple velocity components. (c) For the W spiral arm (spectra plotted in thick lines) there is a large mismatch between the spectral profiles and the expectations from our rotation model only (hourglass symbols in Fig. 3.13). In order of increasing distance from the nucleus along the W spiral arm, gas in the first aperture rotates faster than predicted; the gas profile in the second aperture has a strong red shoulder at a velocity consistent with rotation, while the profile peak is offset ∼30 km s^{-1} to the blue; gas in the third aperture rotates slower than predicted; and gas in the farthest aperture is centered at zero velocity since the aperture lies on the minor axis of the galaxy. (d) For the E spiral arm (spectra plotted in thin lines) the profiles are more centered on the predictions of our rotation only model. In order of increasing distance from the nucleus along the E spiral arm, gas in the first aperture (which includes the edge of the strong CO knot ∼1″ from the nucleus to to NE) lies close to the prediction of the rotation model but a clear blue shoulder is seen; gas in the second aperture shows a clear double-peaked profile with the expected rotation velocity lying in the middle of the two peaks; gas in the third aperture also shows a broad blue shoulder. (e) Including our decelerating outflow model (i.e. using the predictions of rotation plus outflows; asterisks in the figure) the model

predictions change significantly only for the two off-nuclear apertures closest to the nucleus. Here the aperture to the S (solid yellow spectrum in the figure) fits the prediction satisfactorily, i.e. as if almost all gas is in outflows, but to the N (cyan spectrum), while the aperture profile shows an extra blue wing in the correct velocity direction for outflows the magnitude of the offset does not fit well with our model, and the gas seems to be dominantly in rotation rather than outflows. (f) Using a model which sums our streaming toy model to pure rotation (open circles in the figure), we see that the apertures in the W arm are inconsistent with the predictions of streaming inflows: the mismatch between the spectrum peak and the prediction increases when changing from rotation only to rotation plus radial inflow. In the E arm, however, the profiles are in general as consistent with the streaming inflow+rotation model as with the rotation only model, i.e. while the profile peaks are consistent with rotation, the prominent shoulders on these profiles are roughly consistent with streaming inflows. This is also clearly seen in the skewness map (Fig. 3.6 where almost the full inner spiral arm structure shows a blue 'skewness', independent of being on the near- or far-side of the galaxy disk.

We also show the spectra in apertures along the PA of the large scale bar in Fig. 3.14; here we use larger apertures (0.″5 radius) to obtain a higher signal to noise. Here the peak of the spectral profiles are consistent with the predictions of rotation+outflow and a shoulder is seen roughly at the predicted velocity of rotation plus radial streaming inflows.

To test for streaming inflows along spiral patterns further from the nucleus, we also examined the spectra from apertures along the spiral patterns SE to S of the nucleus which connect to the inner spiral arm discussed above, and spectra in apertures tracing spiral structure to the N and NW of the nucleus, which connect to the W inner spiral. We do not show these spectra as the essential results can be seen in the skewness map of the CO J:2-1 line (Fig. 3.6, left panel): here blue (red) colors represent pixels where the CO spectral profile is skewed in the sense of having excess emission towards the blue (red) of the weighted mean velocity at that pixel. To avoid contamination by noise the skewness was calculated using the spectral profile down to 10% of the peak flux. If most of the gas follows regular rotation and a smaller fraction of gas participates in a radial streaming inflow then we expect blue (red) skewness on the far (near) side of the galaxy. The inner 2″ shows profiles skewed consistently to the blue. show that the gas is mainly consistent with rotation. Two spiral arm sections at ∼10″ from the nucleus (roughly at the putative location of the Inner Lindblad Resonance (ILR) of the large-scale

bar (Comerón et al., 2010, C14)) to the SSE and to the N show a skewness consistent with inflows. All spectra in these arms show non symmetric profiles which are likely from multiple velocity components. In fact velocity differences between the peak of the profile and the shoulders to the red match well the predictions of the offset (from rotation) velocity expected from streaming inflows.

3.3.8 Molecular mass in the inner kiloparsec

Molecular gas mass is typically estimated from the CO luminosity (Solomon & Vanden Bout, 2005) using M_{mol} $[M_\odot] = \alpha_{CO} \times L'_{CO}$ where:

$$L'_{CO} = 3.25 \times 10^7 \times S_{line}\Delta\nu \, \frac{D_L^2}{(1+z)^3 \nu_{obs}^2}. \tag{3.2}$$

Here, L'_{CO} has units of K km s^{-1} pc^2, $S_{line}\Delta\nu$ is the integrated flux density of the CO J:1-0 line in Jy km s^{-1}, D_L is the luminosity distance in Mpc, z is the redshift, and ν_{obs} is the observed frequency in GHz. There remains significant debate on the value of α_{CO}, and we use the value α_{CO}= 4.3 [$M_\odot$ (K km s^{-1} pc^2)$^{-1}$] as suggested by Bolatto et al. (2013) for the Galaxy and other nearby spiral galaxies which are not extreme starbursts. Note that L'_{CO} is directly proportional to the surface brightness in K units, and therefore the L'_{CO} ratio of two CO J transitions gives the ratio of their surface brightness temperatures. Furthermore, L'_{CO} is constant for all J levels if the molecular gas emission comes from thermalized optically-thick regions, i.e., the brightness temperature and line luminosity are independent of J and rest frequency for a given molecule (Solomon & Vanden Bout, 2005).

Since we observed the CO J:2-1 line, we require to convert $L'_{COJ:2-1}$ to $L'_{COJ:1-0}$, a conversion which depends on the physical conditions of the gas. Bajaja et al. (1995) have observed the CO J:1-0 and CO J:2-1 lines in NGC 1566 at low resolution using the SEST telescope, and C14 have presented ALMA CO J:3-2 observations of NGC 1566. The nuclear CO J:2-1 / CO J:1-0 intensity ratio found by Bajaja et al. (1995) is 1 in temperature units: as expected from thermalized optically-thick gas. C14 compared the Bajaja et al. (1995) CO J:2-1 integrated flux densities with their ALMA-derived CO J:3-2 integrated flux densities and inferred that the latter was missing some flux; they thus also assumed that the gas is thermalized and optically-thick in their calculation of molecular gas masses.

To further constrain the observed flux ratios, we downloaded the CO J:3-2 data of C14 from the *ALMA Science Archive*[9] and created a Moment 0 map. For thermalized optically-thick gas one expects that the integrated flux density (in units of Jy km s^{-1}) of each CO J transition varies as ν^2. We find that in the inner $\sim$3″ radius (the inner disk), the integrated CO J:2-1 flux density (251 ± 25 [Jy km s^{-1}]) is 1/2.3 times that of CO J:3-2. Over a larger field, $12'' \times 12''$ in size, the total flux density of the CO(J:2-1) line (406 ± 41 [Jy km s^{-1}]) is half that of CO J:3-2. We thus, as in C14, assume thermalized optically-thick gas, i.e. $L'_{\rm COJ:2-1}/L'_{\rm COJ:1-0} = 1$. Under this assumption, using a value of $\alpha_{\rm CO}$ listed above, and D_L = 10 Mpc, the molecular gas mass in the inner spiral arms is $(6.6 \pm 0.7) \times 10^7 [M_\odot]$, and the total molecular gas mass in the central $12'' \times 12''$ region is $(1.1 \pm 0.1) \times 10^8 [M_\odot]$.

Estimating the molecular gas mass in the nuclear outflows of NGC 1566 is more difficult. Recall that outflowing molecular gas is clearly detected out to $\sim$2″ (Sect. 3.3.3), and perhaps out to 5″ (Sect. 3.3.7). To estimate the mass and momentum of the outflowing gas in the unresolved nucleus we extract the nuclear CO J:2-1 emission spectrum in a circular aperture of 0.″2 in radius (similar to our synthesized beam area; Fig. 3.15). This spectrum appears to be made of three distinct components: a strong blue Gaussian representing emission from the blue outflow ($(2.0 \pm 0.2) \times 10^5$ [$M_\odot$]), a weaker red Gaussian representing emission from the red outflow ($(1.0 \pm 0.1) \times 10^5$ [$M_\odot$]) (Sect. 3.3.3) and an intermediate velocity region (green line in the figure; radial velocities between $\pm$40 km s^{-1}; $(0.8 \pm 0.1) \times 10^5$ [$M_\odot$]). This intermediate velocity region could originate in (a) gas in a spherical outflow in the nucleus since variation in the projection angles to the line of sight will give emission at all velocities; (b) unresolved emission from gas in solid body rotation-only; (c) emission from dispersion-dominated gas in the nucleus. With the masses calculated above, and using the (deprojected) mean flux-weighted velocity of each of the above components under the assumption that the outflows are in the plane of the disk we can estimate the outflow momentum in the unresolved nucleus, obtaining $(-10.5 \pm 1.5) \times 10^6$ [$M_\odot$ km s^{-1}] and $(6.6 \pm 0.9) \times 10^6$ [$M_\odot$ km s^{-1}] for the blue and red outflows in the inner (unresolved; $\lesssim$19.2 pc) nucleus, respectively.

Since the outflows extend beyond the inner (unresolved) nucleus we can extend this outflow mass analysis to larger scales. From the bottom right panel of Fig. 3.9, we can distinguish that the putative outflows along the minor axis show two stages: (1) an initial stage between radii of 0 to $\sim$1″ which show velocities close to the peak velocity, and (2)

[9] https://almascience.nrao.edu/aq/

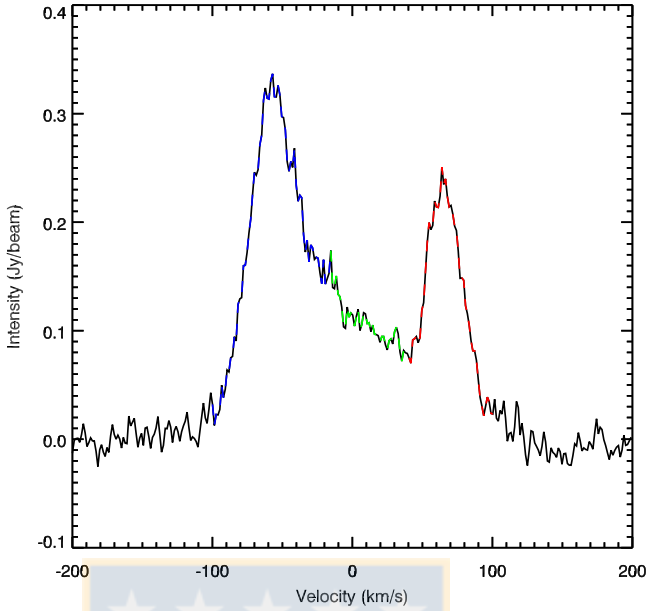

Figure 3.15 The nuclear CO spectrum of NGC 1566. Spectrum (black) corresponds to a circular aperture centered on the nucleus with radius 0.″2 and was divided by eye into three parts: the pure outflow components (blue and red) and an intermediate velocity region (green; see text) between the blue and red outflow peaks. Source: Slater et al. (2018).

a final stage with monotonically decreasing velocities (down to ∼0) between 1″ and 1.″5 from the nucleus. For these two stages (but excluding the innermost 0.″2 considerated as the nuclear outflows above) we obtain total outflow mass values of $(9.3 \pm 0.9) \times 10^6[\mathrm{M}_\odot]$ and $(11.6 \pm 1.2) \times 10^6[\mathrm{M}_\odot]$, respectively.

In the absence of clear signatures of inflowing gas we do not attempt to estimate an exhaustive streaming inflow rate. Instead we show two examples of spectra in apertures for which we found the strongest signatures of non circular motions which could be explained by our toy streaming model (see Sect. 3.3.7) and use these to roughly estimate the mass involved in the inflow. In the E inner spiral we use the spectra of apertures 1 and 2 of Fig. 3.13. These spectra are shown in Fig. 3.16, with the red overlay denoting the velocities over which the emission is from gas potentially participating in the streaming inflows. For each of these apertures we find masses of $\sim (1.1 \pm 0.4) \times 10^5$ $[M_\odot]$ potentially participating in a streaming inflow. We performed the same exercise with four apertures in the outer extension of the E spiral arm (not shown) and find a median mass

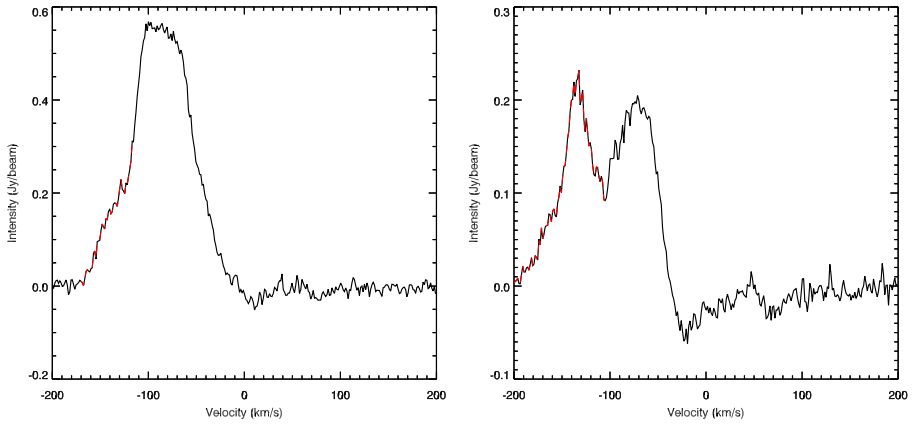

Figure 3.16 CO spectra extracted above the inner disk in NGC 1566. Spectra extracted from apertures 1 and 2 of Fig. 3.13 (the E inner spiral arm) are shown in black. The red overlay marks the velocities over which emission comes from gas potentially participating in streaming inflows. Source: Slater et al. (2018).

of $\sim (4 \pm 0.4) \times 10^4$ [$M_\odot$] potentially participating in a streaming inflow.

3.3.9 Mass of the SMBH in NGC 1566

To estimate the black hole mass in NGC 1566 , we use the empirical correlation between SMBH mass and stellar velocity dispersion $\sigma_\star$ (Ferrarese & Merritt, 2000; Gebhardt et al., 2000; Tremaine et al., 2002; Gültekin et al., 2009; Kormendy & Ho, 2013). Note that this M-$\sigma_\star$ relationship can also be reliably applied to nearby AGNs (Nelson et al., 2004; Woo et al., 2010; Graham et al., 2011). While there are several versions of the M-$\sigma_\star$ relation we use that of Gültekin et al. (2009) for their entire sample for several reasons; they demonstrate that previous studies are biased by considering culled samples according whether the SMBH sphere of influence is resolved (see Sect. 4 of their paper). Therefore we get:

$$\left(\frac{M_{BH}}{M_\odot}\right) = 10^{(8.12\pm0.08)} \cdot \left(\frac{\sigma}{200}\right)^{(4.24\pm0.41)} \tag{3.3}$$

where σ, is the central velocity dispersion in km s^{-1}. To obtain the latter, we fit the integrated spectrum from our GMOS/IFU datacube with the program *pPXF* described in Cappellari & Emsellem (2004). The spectrum from 5700Å to 6300Å was fit in *pPXF* using SSPs templates from Bruzual & Charlot (2003), obtaining a central stellar velocity dispersion of $\sigma_\star = 116 \pm 9$ km s^{-1}. This value is consistent with that obtained using $\sigma_\star$

from Bottema (1992) for the innermost region in NGC 1566, and larger than the bulge stellar velocity dispersion used in other previous studies (van der Kruit & Freeman, 1984; Nelson & Whittle, 1995; Woo & Urry, 2002).

Our measured value of σ implies an estimated super massive black hole mass of $M_{BH} = 1.3 \pm 0.6 \times 10^7$ [$M_\odot$].

3.3.10 Bolometric luminosity and accretion, inflow, and outflow rates

Given the SMBH mass estimated above, for which the Eddington Luminosity is $L_{Edd} = (4.0 \pm 1.8) \times 10^{11}$ [$L_\odot$], we would like to ascertain the bolometric luminosity of the AGN L_{Bol} as well the Eddington ratio ($l_{Edd} = \frac{L_{Bol}}{L_{Edd}}$).

Several differing values for L_{Bol}, for NGC 1566 have been obtained in previous studies. Here we use two different approaches to estimate L_{Bol}: from the nuclear [OIII] luminosity, and from the nuclear hard X-ray luminosity. The nuclear 2–10 keV luminosity as measured by *XMM* and scaled to our adopted distance (10 Mpc) is $L_X = (7 \pm 3) \times 10^{33}$ [W] (Levenson et al., 2009). Using the hard X-ray to bolometric luminosity conversion of Ulvestad & Ho (2001) ($L_{Bol} = 6.7 \times L_{X(2-10keV)}$) we obtain $L_{Bol} = (4.69 \pm 2) \times 10^{34}$ [W]. The nuclear [OIII] flux (Moustakas et al., 2010) at our adopted distance gives $L_{[OIII]} = (8.2 \pm 1.8) \times 10^{31}$ [W]. Using the scaling of Heckman et al. (2004) modified as recommended in Dumas et al. (2007) ($L_{Bol} = 90 \times L_{[OIII]}$) we obtain $L_{Bol} = (7.42 \pm 1.62) \times 10^{33}$ [W]. These two methods thus give relatively consistent values for L_{Bol} and we thus adopt the mean value of $L_{Bol} = (2.7 \pm 1.3) \times 10^{34}$ [W] which implies $l_{Edd} \approx 2.0 \times 10^{-4}$, i.e. a relatively low efficiency regime for the SMBH, considering the fact that in the most active galaxies, gas is accreted onto the SMBH in a efficient regime with ratios between 0.01-1 (Khorunzhev et al., 2012). We can now estimate the mass accretion rates as follows:

$$\dot{m} = \frac{L_{Bol}}{c^2 \eta} \tag{3.4}$$

where η is the accretion efficiency which in nearby galaxies with geometrically thin, optically thick accretion disks, is typically taken to be 0.1 (Soltan, 1982; Fabian & Iwasawa, 1999; Yu & Tremaine, 2002; Davis & Laor, 2011). We thus get an accretion rate of $\dot{m} = (4.8 \pm 2.3) \times 10^{-5}$ [$M_\odot yr^{-1}$].

We note that very discrepant values of L_{Bol} were obtained by Woo & Urry (2002) who integrated the flux in the spectral energy distribution (SED) of NGC 1566 using data from

NED, after averaging multiple datapoints in the same band and correcting for dust. The value of L_{Bol} they obtained, scaled to our adopted distance, is $L_{Bol} = 7.2 \times 10^{36}$ [W]. This implies $l_{Edd} = 0.05$ and an accretion rate of $\dot{m} = 1.3 \times 10^{-2}$ [$M_{\odot}yr^{-1}$], 3 orders of magnitude higher than the values obtained above. Two potential reasons for this large discrepancy are (a) flux variability in the hard X-ray, see e.g. Landi et al. (2005); (b) the use of large (galaxy-wide), rather than nuclear, apertures for the data in NED. In Sect. 3.3.8 we roughly estimated the mass of the molecular gas potentially participating in streaming inflows using six apertures along the SSE to E spiral arm. This can be used to estimate a rough mass inflow rate. The radius of each aperture (0.″2) corresponds to a linear diameter of 19 pc. A streaming inflow velocity of $\sim$ 50 km s^{-1} would imply an aperture crossing time of $\sim 3.8 \times 10^5$ [yr], and thus a mass inflow rate of 0.1 [$M_{\odot}yr^{-1}$] along this spiral arm.

A similar procedure can be used to estimate the outflow rates. We use the molecular masses deduced for the blue and red components of the outflows in the nuclear (0.″2 radius) aperture (see Sect. 3.3.8 and Fig. 3.15). In Sect. 3.3.3 we have argued that the velocity of the outflows in the nucleus is $\sim$ 180 km s^{-1} in the plane of the disk, which gives a crossing time of around 5.42×10^4 [yr] for the nuclear 0.″2 aperture used. The nuclear molecular mass outflow rates are thus 3.7 [$M_{\odot}yr^{-1}$] for the blueshifted component and 1.9 [$M_{\odot}yr^{-1}$] for the redshifted component. Note that these outflows do not appear to escape from the nucleus, but instead 'pile up' in the inner gas ring (see the CO residual map and pv diagrams). We can also estimate the kinetic power associated with cold molecular outflow following, e.g., Harrison et al. (2014) and Lena (2015):

$$\dot{E}_{out} = \frac{\dot{M}_{out}}{2}(v^2_{outflow} + 3\sigma^2). \tag{3.5}$$

Assuming a nuclear velocity dispersion of 60 km s^{-1} (see Fig. 3.6) and, as mentioned above, $v_{outflow}$ = 180 km s^{-1}, we obtain a total outflow kinetic power (over both blue and red outflow components) of $\dot{E}_{out} = 7.62 \times 10^{33}$ [W]. The ratio between the outflow kinetic power and the AGN bolometric luminosity is thus $\frac{\dot{E}_{out}}{L_{Bol}} \approx 0.28$. This is significantly larger than the values obtained in previous studies of nearby active galaxies which found $\frac{\dot{E}_{out}}{L_{Bol}}$ ranging between 0.1-10% (e.g. Storchi-Bergmann et al., 2010; Müller-Sánchez et al., 2011; Harrison et al., 2014; Lena, 2015; Müller-Sánchez et al., 2016) or even lower (e.g. Barbosa et al., 2009, less than 0.01%). However all of these studies have measured out-

flow masses using ionized gas, which is expected to be a minor fraction of the total gas content and also, using measurements on larger spatial scales than those considered here (0.″4 or ∼24 pc).

3.4 Summary and Conclusions

We have analyzed the kinematics in the inner kiloparsec of the nearby active galaxy NGC 1566, using ALMA observations of CO J:2-1 along with GMOS/IFU data of ionized gas emission lines and stellar absorption lines. Our results allow us to conclude that:

- NGC 1566 presents a cold molecular dense disk in the inner 144 pc, along with a clear two-arm spiral structure in the inner 96 pc. These structures are also seen in our ionized gas ([NII]) images, as well as in previous studies using CO J:3-2 and optical/IR emission lines. The inner spiral arms and dense disk appear to have some continuity with more extended CO J:2-1 spiral arms which extend out of the inner disk to larger scales, and which coincide with dust lanes seen in HST images.

- Ionized gas and stars are detected over the full IFU FOV at high signal to noise. The [NII] emission is peaked at the nucleus and is also strong at the known star-forming region to the SW, about 1.″5 from the nucleus.

- The superior spectral resolution (∼2.6 km s^{-1}) and image fidelity in this new CO J:2-1 datacube allows improved constraints on the nuclear kinematics. Further, our use of pv diagrams (rather than only intensity weighted velocity maps) allows the full exploitation of our velocity resolution. The molecular gas kinematics of the inner disk is dominated by rotation with peak velocities of $\sim \pm 140$ km s^{-1}. The residual velocity field shows clear signs of non rotational motion especially in the innermost ∼2″ region. We argue that the strongest deviations are the result of nuclear outflows, though the strong two-arm inner spiral structure and large-scale bar also play a role. The CO rotational curve over the inner ∼3″ is asymmetric, which could be the consequence of a warped disk. PV diagrams at PAs between $-15°$ to $15°$ show some discrepancies from our rotation + outflow model at radii ∼1.″5 from the nucleus. These discrepancies could be explained by perturbations due to the barred potential and/or streaming velocities.

- We argue for the presence of nuclear (inner ∼2″) molecular gas outflows in the plane of the galaxy disk, without ruling out the presence of bar- or spiral-related perturbations (see Sect. 3.3.6 for a detailed analysis of the potential bar influence). The arguments for a nuclear outflow include: (a) several previous authors have claimed kinematic and morphological evidence of outflows in the NLR, which likely intersect the galaxy disk given the observed geometries; (b) The nucleus shows a double-peaked profile with FWZI 200 km s^{-1}, higher than that seen in the lower fidelity maps of C14, and which imply inclination corrected outflow velocities of up to 180 km s^{-1} in the plane of the disk. A large angle between the outflow axis and the line of sight is unlikely since this would imply extremely high true outflow velocities. Attributing these velocity features to other perturbations in the plane of the disk and along the minor axis requires true radial velocities around ∼80–130 km s^{-1}in the nuclear region where rotation velocities are expected to be ≤40 km s^{-1}. In Sect. 3.3.6 we analysed the large scale bar perturbation and its implications, showing that it does not reliably produce both the morphology and the large perturbations seen in the observed velocity field; (c) the pv diagram along the minor axis (bottom right panel of Fig. 3.9) connects high-velocity components to the zero velocity components seen at r ≈1.″8 on both sides of the nucleus. The regions with the largest velocity deceleration are correlated with the regions brightest in CO and thus richest in molecular gas, indicating that the outflows decelerate due to mass loading which is clearly seen in the inner arcsec to the N and in the r∼ 1–2″ range to the S; (d) the pv diagrams (Fig. 3.9) show velocity deviations which are consistent with radial outflows not just in the minor axis, but also in the plane of the disk over all PAs and over apertures at distances of several synthesized beams from the nucleus (see Sect. 3.3.5); and (e) the consistence with the evidence of a nuclear spherical (or bipolar) outflow in our ionized gas kinematics. We also argue that the molecular outflow is primarily detected within the galaxy disk. The supporting arguments for this include the low velocity dispersion of the molecular gas, the absence of evidence for radio jet-related outflows, the posited deceleration of the outflow, which would be consistent with the high density of gas in the galaxy disk. Other potential scenarios as warped disk or non coplanar disk cannot be constrained by us due to the limited resolution, the sparse velocity field and the lack of a reliable circular rotation model.

- While the stellar and ionized gas kinematics predominantly traces rotation in the galaxy disk, we find evidence of two components in the ionized gas: a narrow (σ ~60 km s^{-1}) component detected over almost the full field of view and which traces rotation in the disk, and a broad component detected in the inner ~3″radius. We postulate that the broad component of ionized gas is part of a nuclear spherical outflow. The broad component of the [NII] emission line does not participate in the rotation of the galaxy disk. Instead it is preferentially blueshifted, as expected since nuclear dust obscures the receding side of the spherical outflow. Its velocity dispersion, velocity, and the correlation with strong and weaker dust features in the nucleus all strengthen the arguments for the spherical ionized gas outflow. Despite this, we are not ruling out the possibility of a bipolar outflow which currently is impeded by a poor resolution in the GMOS data. We are unable to test for deceleration in this outflow.

- We have constrained and analyzed the circular vs. perturbed kinematics of the CO gas in the disk using *Kinemetry*, *Diskfit*, and linear perturbation theory. Large radial velocity perturbations are clearly required. The *Diskfit* model better fits the observed data as compared to the pure rotation model, but still does not attain the highest velocities seen in the inner arcsecs and fails to predict the large peak velocities seen along the minor axis in pv diagram (bottom middle panel in Fig. 3.12). The relatively good fits obtained by *Diskfit* do not necessarily imply that the perturbations are bar related. Our concerns here include the lack of definition of the physical parameters (e.g., pattern speed) used, and our findings that *Diskfit* typically provides good fits to perturbed kinematics of other similar datasets, even in the absence of a bar. For our linear epicyclic perturbation (in the presence of a bar or m=2 mode) modelling, which provides a more physically-based model as compared to *Diskfit*, we used two input rotation models, one based on the best-fit gas rotation model and one on the best-fit stellar rotation model. In both cases we varied the bar pattern speed and damping factor. While the perturbed velocity fields show the characteristic butterfly pattern expected from bar perturbations, very high pattern speeds ($\gtrsim$ 300 km s^{-1} kpc^{-1}) are required to cause a resonance close to r$\approx$1″ and thus explain the observed high-velocity features along the minor axis. We note however that if the true distance to NGC 1566 is higher, the problem of high pattern speeds is mitigated. Even if the resonance radii are matched, the velocity structures

seen in the models are not aligned with or as sharp as those observed.

- We are unable to definitely prove the existence of streaming inflows based on the kinematics of the molecular or ionized gas. This is in part due to the line profiles being complex with evidence of multiple velocity components, and also due to an asymmetry in the velocity profiles of the near and far sides of the disk, which could be due to disk warping or the non-axisymmetric potential. We present and analyze specific apertures along a spiral arm where the spectral profiles are similar to those expected from our toy streaming inflow model and from these we estimate a potential streaming inflow rate of 0.1 [$M_{\odot}yr^{-1}$].

- We estimate the molecular mass of the unresolved nuclear outflow (the innermost 0.″2 aperture) as $(3.8 \pm 0.4) \times 10^5$ [$M_{\odot}$] and its momentum as $(10.5 \pm 1.5) \times 10^6$ [$M_{\odot}$ km s^{-1}] and $(6.6 \pm 0.9) \times 10^6$ [$M_{\odot}$ km s^{-1}] for the blue and red outflows, respectively. Summing all gas believed to be participating in the nuclear outflow (out to $\sim$ 1.″5 or $\sim$72 pc from the nucleus) we find a mass of 2.1×10^7 [$M_{\odot}$]. Given the nuclear velocities, the implied outflow rates from the nuclear 0.″2 region are 3.7 [$M_{\odot}yr^{-1}$] for the blueshifted component and 1.9 [$M_{\odot}yr^{-1}$] for the redshifted component. We emphasize that these outflows appear to decelerate within the inner 100 pc and thus the gas is not lost to the galaxy nucleus.

- We have used the results of three methods to estimate L_{Bol}: from the nuclear [OIII] luminosity, from the nuclear hard X-ray luminosity, and from a SED fit. The first two methods give consistent results: a mean value of $L_{Bol} = (2.7 \pm 1.3) \times 10^{34}$ [W], which implies l_{Edd} of $\sim 2.2 \times 10^{-4}$, indicating a relatively low efficiency regime for the SMBH, and an accretion rate of $\dot{m} = (4.8 \pm 2.3) \times 10^{-5}$ [$M_{\odot}yr^{-1}$], significantly smaller than the posited nuclear molecular outflow rate.

- A direct comparison between the molecular outflow kinetic power and the AGN bolometric luminosity gives a ratio of $\frac{\dot{E}_{out}}{L_{Bol}} \approx 0.28$, a value significantly larger than typical values (between 0.01–10%) found from previous studies ionized gas in nearby AGNs. This supports the idea that the ionized gas is a minor fraction of the total gas content.

4

Conclusions

4.1 General Conclusions

This work can be summarized as follows:

- Spectral line imaging as moment maps and pv diagrams, give a more detailed information of the kinematics. However, 3-D analysis (RA, DEC, Vel) rather than just 2-d images like moment maps, complement the kinematic description to disentangle the kinematic components in several sources specially, in some which can present an important deviation but it is not as stronger as to be detected in averaged maps like velocity fields.

- The CO J:2-1 integrated maps in our sample showed sources with disk-like rotation and some with spiral arms. The residual maps of most of the galaxies showed the presence of significant perturbations with clear signs of outflows/inflows in NGC 1386, NGC 2110 and of course in NGC 1566.

- Some important morphological features reported in some sources analized in Chapt. 2 are: a decoupled inner region and also into a counter-rotating one in NGC 1667 likely a direct consequence of a bar (classical effect at lower radii of the ILR) and a possible recent minor merger in the inner 5″ in NGC 2110 due to its strongly disturbed maps seen in its velocity field and specially in its velocity dispersion.

- We postulated an AGN decelerated outflow scenario in molecular gas for NGC 1566 mainly because: a) The nucleus shows a double peaked profile with Full Width at

Zero Intensity, higher than that seen in the lower fidelity maps from previous studies, and which imply inclination corrected outflow velocities of up to 180 km s^{-1} in the plane of the disk. b) The pv diagram along the minor axis connects high velocity components to the zero velocity components seen at the inner 1.8″ from the nucleus and also, the velocity decrease is agree for crossing higher density regions c) The pv diagrams show velocity deviations which are consistent with a radial outflow in the plane of the disk over all PAs and d) There is consistence with the evidence of a nuclear spherical (or bipolar) outflow in our ionized gas kinematics at similar scales.

- With NGC 1566, we have noted the importance to take into account the bar structure in galaxies which presents this morphology in the gas kinematics. Despite of its influence mainly a greater radii than the ILR radius as have been pointed out by previous authors, its influence in non-circular components could be also important in the inner kpc. In NGC 1566this issue was reported by previous studies and it was put for testing in this work. By bar modelling, we could not discard the influence of the bar in the nuclear kinematics of CO J:2-1 although instead previous authors, we argue for nuclear non-circular components strongly dominated by AGN feedback making the bar impact at these scales, negligible.

- Despite of we were unable to definitely prove the existence of streaming inflows based mainly on the kinematics of CO J:2-1, We presented and analyzed specific apertures along a spiral arm estimating a potential streaming inflow rate of 0.1 [$M_{\odot}yr^{-1}$]. Making a direct comparison with one of our accretion rates estimated of $\dot{m} = (4.8 \pm 2.3) \times 10^{-5}$ [$M_{\odot}yr^{-1}$], we can realized that the latter is ∼4 orders of magnitude lower than just an estimated 'lower limit' of inflow rate for this galaxy, which implies that the real (not measured) inflow rate is sufficiently greater (more than 4 order of magnitude) to lead the accumulation of enough gas in the inner few hundred parsecs, to trigger the formation of new stars, leading to the growth of the galaxy bulge meaningfully. We are in front to a scenario completely different from studies related to ionized gas where typical differences between inflow rates and accretion rates are around 2 to 3 orders of magnitude (Storchi-Bergmann, 2014).

4.2 Future Prospective

In the nearest future results imperative to extend our deeper kinematic analysis applied in NGC 1566 to the rest of galaxies in our sample. After this, it would be important extend the study of cold molecular kinematics to more sets of AGN previously well studied in other gas phases as optical or infrared and so, understanding the possible similarities and differences among several AGN types.

It is clear that one of the important problems to study the AGN physical processes is to obtain high-spatial resolution data since everything important happens in the central few hundred parsecs of active galaxies. However, nowadays this is easier with the recent new generation of telescopes like ALMA and also with others which are part of the next generation as SKA.

Therefore, we are in the best epoch to study the gas kinematics at high spatial resolution and covering almost the entire electromagnetic spectrum. The latter is an important issue considering that AGN are the most broad-band emitters in the universe. As an example, in this work it has been demonstrated that feedback processes as nuclear outflows in NGC 1566 take part at different phases of the gas (ionized gas and cold molecular gas) with a presumable same origin but morphologically different. Thus it is evident the importance to elucidate these components not only from one wavelength range only, but by taking multi-wavelengths observations in order to get the full picture of their physical properties, and here is where the new generations of detectors, telescopes as well as new interferometric techniques will play an important role to achieve this goal in the coming years.

Bibliography

Agüero, E. L., Díaz, R. J., & Bajaja, E., *A&A*, 414:453–461, February 2004.

Alloin, D., Pelat, D., Phillips, M., & Whittle, M., *ApJ*, 288:205–220, January 1985.

Antonucci, R., *ARA&A*, 31:473–521, 1993.

Baillard, A., Bertin, E., de Lapparent, V., Fouqué, P., Arnouts, S., Mellier, Y., Pelló, R., Leborgne, J.-F., Prugniel, P., Makarov, D., Makarova, L., McCracken, H. J., Bijaoui, A., & Tasca, L., *A&A*, 532:A74, August 2011.

Bajaja, E., Wielebinski, R., Reuter, H.-P., Harnett, J. I., & Hummel, E., *A&AS*, 114:147, November 1995.

Baldry, I. K., Glazebrook, K., Brinkmann, J., Ivezić, Ž., Lupton, R. H., Nichol, R. C., & Szalay, A. S., *ApJ*, 600:681–694, January 2004.

Barbosa, F. K. B., Storchi-Bergmann, T., Cid Fernandes, R., Winge, C., & Schmitt, H., *MNRAS*, 371:170–184, September 2006.

Barbosa, F. K. B., Storchi-Bergmann, T., Cid Fernandes, R., Winge, C., & Schmitt, H., *MNRAS*, 396:2–18, June 2009.

Barbosa, F. K. B., Storchi-Bergmann, T., McGregor, P., Vale, T. B., & Rogemar Riffel, A., *MNRAS*, 445:2353–2370, December 2014.

Beckmann, V. & Shrader, C. *The AGN phenomenon: open issues*. In *Proceedings of "An INTEGRAL view of the high-energy sky (the first 10 years)" - 9th INTEGRAL Workshop and celebration of the 10th anniversary of the launch (INTEGRAL 2012). 15-19 October 2012. Bibliotheque Nationale de France, Paris, France. Published online at ¡A href="http://pos.sissa.it/cgi-bin/reader/conf.cgi?confid=176"¿http://pos.sissa.it/cgi-bin/reader/conf.cgi?confid=176¡/A¿, id.69*, page 69, 2012.

Bertola, F., Bettoni, D., Danziger, J., Sadler, E., Sparke, L., & de Zeeuw, T., *ApJ*, 373: 369–390, June 1991.

Bolatto, A. D., Wolfire, M., & Leroy, A. K., *ARA&A*, 51:207–268, August 2013.

Boone, F., Baker, A. J., Schinnerer, E., Combes, F., García-Burillo, S., Neri, R., Hunt, L. K., Léon, S., Krips, M., Tacconi, L. J., & Eckart, A., *A&A*, 471:113–125, August 2007.

Bottema, R., *A&A*, 257:69–84, April 1992.

Bournaud, F. & Combes, F., *A&A*, 392:83–102, September 2002.

Bruzual, G. & Charlot, S., *MNRAS*, 344:1000–1028, October 2003.

Cappellari, M. & Emsellem, E., *PASP*, 116:138–147, February 2004.

Casasola, V., Combes, F., García-Burillo, S., Hunt, L. K., Léon, S., & Baker, A. J., *A&A*, 490:61–76, October 2008.

Cicone, C., Maiolino, R., Sturm, E., Graciá-Carpio, J., Feruglio, C., Neri, R., Aalto, S., Davies, R., Fiore, F., Fischer, J., García-Burillo, S., González-Alfonso, E., Hailey-Dunsheath, S., Piconcelli, E., & Veilleux, S., *A&A*, 562:A21, February 2014.

Colina, L. & Wada, K., *ApJ*, 529:845–852, February 2000.

Combes, F. *AGN Fueling: The observational point of view*. In Collin, S., Combes, F., & Shlosman, I., editors, *Active Galactic Nuclei: From Central Engine to Host Galaxy*, volume 290 of *Astronomical Society of the Pacific Conference Series*, page 411, 2003.

Combes, F. *Infall and Accretion*. In Knapen, J. H., Mahoney, T. J., & Vazdekis, A., editors, *Pathways Through an Eclectic Universe*, volume 390 of *Astronomical Society of the Pacific Conference Series*, page 369, June 2008.

Combes, F. *Models of AGN feedback*. In Ziegler, B. L., Combes, F., Dannerbauer, H., & Verdugo, M., editors, *Galaxies in 3D across the Universe*, volume 309 of *IAU Symposium*, pages 182–189, February 2015. doi: 10.1017/S1743921314009636.

Combes, F., García-Burillo, S., Casasola, V., Hunt, L. K., Krips, M., Baker, A. J., Boone, F., Eckart, A., Marquez, I., Neri, R., Schinnerer, E., & Tacconi, L. J., *A&A*, 565:A97, May 2014.

Comerón, S., Knapen, J. H., Beckman, J. E., Laurikainen, E., Salo, H., Martínez-Valpuesta, I., & Buta, R. J., *MNRAS*, 402:2462–2490, March 2010.

Crenshaw, D. M., Kraemer, S. B., & Gabel, J. R., *AJ*, 126:1690–1698, October 2003.

Cresci, G. & Maiolino, R., *Nature Astronomy*, 2:179–180, March 2018.

Czerny, B. & Hryniewicz, K., *A&A*, 525:L8, January 2011.

da Silva, P., Steiner, J. E., & Menezes, R. B., *MNRAS*, 470:3850–3876, October 2017.

Davies, R. L., Dopita, M. A., Kewley, L., Groves, B., Sutherland, R., Hampton, E. J., Shastri, P., Kharb, P., Bhatt, H., Scharwächter, J., Jin, C., Banfield, J., Zaw, I., James, B., Juneau, S., & Srivastava, S., *ApJ*, 824:50, June 2016.

Davis, S. W. & Laor, A., *ApJ*, 728:98, February 2011.

de Vaucouleurs, G., *ApJ*, 181:31–50, April 1973.

Dicaire, I., Carignan, C., Amram, P., Hernandez, O., Chemin, L., Daigle, O., de Denus-Baillargeon, M.-M., Balkowski, C., Boselli, A., Fathi, K., & Kennicutt, R. C., *MNRAS*, 385:553–605, April 2008.

Diniz, M. R., Riffel, R. A., Storchi-Bergmann, T., & Winge, C., *MNRAS*, 453:1727–1739, October 2015.

Dumas, G., Mundell, C. G., Emsellem, E., & Nagar, N. M., *MNRAS*, 379:1249–1278, August 2007.

Ehle, M., Beck, R., Haynes, R. F., Vogler, A., Pietsch, W., Elmouttie, M., & Ryder, S., *A&A*, 306:73, February 1996.

Elmegreen, D. M., Elmegreen, B. G., & Eberwein, K. S., *ApJ*, 564:234–243, January 2002.

Elvis, M., Fassnacht, C., Wilson, A. S., & Briel, U. *Extended X-Ray Emission in Seyfert Galaxies*. In Meurs, E. J. A. & Fosbury, R. A. E., editors, *European Southern Observatory Conference and Workshop Proceedings*, volume 32 of *European Southern Observatory Conference and Workshop Proceedings*, page 243, July 1989.

Emsellem, E., Goudfrooij, P., & Ferruit, P., *MNRAS*, 345:1297–1312, November 2003.

Emsellem, E., Fathi, K., Wozniak, H., Ferruit, P., Mundell, C. G., & Schinnerer, E., *MNRAS*, 365:367–384, January 2006.

Emsellem, E., Renaud, F., Bournaud, F., Elmegreen, B., Combes, F., & Gabor, J. M., *MNRAS*, 446:2468–2482, January 2015.

Englmaier, P. & Shlosman, I., *ApJ*, 617:L115–L118, December 2004.

Erwin, P., *A&A*, 415:941–957, March 2004.

Fabian, A. C., *ARA&A*, 50:455–489, September 2012.

Fabian, A. C. & Iwasawa, K., *MNRAS*, 303:L34–L36, February 1999.

Fanaroff, B. L. & Riley, J. M., *MNRAS*, 167:31P–36P, May 1974.

Fathi, K. *Morphology and Dynamics in the Inner Regions of Spiral Galaxies*. PhD thesis, University of Groningen, 2004.

Fathi, K., van de Ven, G., Peletier, R. F., Emsellem, E., Falcón-Barroso, J., Cappellari, M., & de Zeeuw, T., *MNRAS*, 364:773–782, December 2005.

Ferrarese, L. & Ford, H., *Space Sci. Rev.*, 116:523–624, February 2005.

Ferrarese, L. & Merritt, D., *ApJ*, 539:L9–L12, August 2000.

Feruglio, C., Maiolino, R., Piconcelli, E., Menci, N., Aussel, H., Lamastra, A., & Fiore, F., *A&A*, 518:L155, July 2010.

Finlez, C., Nagar, N., & others, in prep.

Franx, M., van Gorkom, J. H., & de Zeeuw, T., *ApJ*, 436:642–653, December 1994.

Ganguly, R. & Brotherton, M. S., *ApJ*, 672:102–107, January 2008.

García-Burillo, S., Combes, F., Hunt, L. K., Boone, F., Baker, A. J., Tacconi, L. J., Eckart, A., Neri, R., Leon, S., Schinnerer, E., & Englmaier, P., *A&A*, 407:485–502, August 2003.

García-Burillo, S., Combes, F., Schinnerer, E., Boone, F., & Hunt, L. K., *A&A*, 441: 1011–1030, October 2005.

García-Burillo, S., Combes, F., Usero, A., Aalto, S., Krips, M., Viti, S., Alonso-Herrero, A., Hunt, L. K., Schinnerer, E., Baker, A. J., Boone, F., Casasola, V., Colina, L., Costagliola, F., Eckart, A., Fuente, A., Henkel, C., Labiano, A., Martín, S., Márquez, I., Muller, S., Planesas, P., Ramos Almeida, C., Spaans, M., Tacconi, L. J., & van der Werf, P. P., *A&A*, 567:A125, July 2014.

García-Burillo, S., Combes, F., Usero, A., Aalto, S., Colina, L., Alonso-Herrero, A., Hunt, L. K., Arribas, S., Costagliola, F., Labiano, A., Neri, R., Pereira-Santaella, M., Tacconi, L. J., & van der Werf, P. P., *A&A*, 580:A35, August 2015.

Gebhardt, K., Bender, R., Bower, G., Dressler, A., Faber, S. M., Filippenko, A. V., Green, R., Grillmair, C., Ho, L. C., Kormendy, J., Lauer, T. R., Magorrian, J., Pinkney, J., Richstone, D., & Tremaine, S., *ApJ*, 539:L13–L16, August 2000.

González Delgado, R. M., Arribas, S., Pérez, E., & Heckman, T., *ApJ*, 579:188–204, November 2002.

Graham, A. W., Onken, C. A., Athanassoula, E., & Combes, F., *MNRAS*, 412:2211–2228, April 2011.

Greene, J. E., Zakamska, N. L., & Smith, P. S., *ApJ*, 746:86, February 2012.

Greenhill, L. J., Booth, R. S., Ellingsen, S. P., Herrnstein, J. R., Jauncey, D. L., McCulloch, P. M., Moran, J. M., Norris, R. P., Reynolds, J. E., & Tzioumis, A. K., *ApJ*, 590: 162–173, June 2003.

Gruppioni, C., Berta, S., Spinoglio, L., Pereira-Santaella, M., Pozzi, F., Andreani, P., Bonato, M., De Zotti, G., Malkan, M., Negrello, M., Vallini, L., & Vignali, C., *MNRAS*, 458:4297–4320, June 2016.

Gültekin, K., Richstone, D. O., Gebhardt, K., Lauer, T. R., Tremaine, S., Aller, M. C., Bender, R., Dressler, A., Faber, S. M., Filippenko, A. V., Green, R., Ho, L. C., Kormendy, J., Magorrian, J., Pinkney, J., & Siopis, C., *ApJ*, 698:198–221, June 2009.

Haan, S., Schinnerer, E., Emsellem, E., García-Burillo, S., Combes, F., Mundell, C. G., & Rix, H.-W., *ApJ*, 692:1623–1661, February 2009.

Hackwell, J. A. & Schweizer, F., *ApJ*, 265:643–647, February 1983.

Harrison, C. M., Alexander, D. M., Mullaney, J. R., & Swinbank, A. M., *MNRAS*, 441: 3306–3347, July 2014.

Heckman, T. M., *A&A*, 87:152–164, July 1980.

Heckman, T. M. & Best, P. N., *ARA&A*, 52:589–660, August 2014.

Heckman, T. M., Kauffmann, G., Brinchmann, J., Charlot, S., Tremonti, C., & White, S. D. M., *ApJ*, 613:109–118, September 2004.

Ho, L. C., *ARA&A*, 46:475–539, September 2008.

Ho, L. C., Filippenko, A. V., & Sargent, W. L. W. *The Palomar Observatory dwarf Seyfert survey.* In Courvoisier, T. & Blecha, A., editors, *Multi-Wavelength Continuum Emission of AGN*, volume 159 of *IAU Symposium*, pages 275–278, 1994.

Ho, L. C., Filippenko, A. V., & Sargent, W. L. W., *ApJ*, 487:568–578, October 1997a.

Ho, L. C., Filippenko, A. V., & Sargent, W. L. W., *ApJS*, 112:315–390, October 1997b.

Hollyhead, K., Adamo, A., Bastian, N., Gieles, M., & Ryon, J. E., *MNRAS*, 460:2087–2102, August 2016.

Hopkins, P. F. & Quataert, E., *MNRAS*, 415:1027–1050, August 2011.

Hopkins, P. F. & Quataert, E., *MNRAS*, 407:1529–1564, September 2010.

Hubble, E. P., *ApJ*, 64, December 1926.

Hunt, L. K., Combes, F., García-Burillo, S., Schinnerer, E., Krips, M., Baker, A. J., Boone, F., Eckart, A., Léon, S., Neri, R., & Tacconi, L. J., *A&A*, 482:133–150, April 2008.

Ishibashi, W. & Fabian, A. C., *MNRAS*, 427:2998–3005, December 2012.

Kauffmann, G., Heckman, T. M., Tremonti, C., Brinchmann, J., Charlot, S., White, S. D. M., Ridgway, S. E., Brinkmann, J., Fukugita, M., Hall, P. B., Ivezić, Ž., Richards, G. T., & Schneider, D. P., *MNRAS*, 346:1055–1077, December 2003.

Kawamuro, T., Ueda, Y., Tazaki, F., & Terashima, Y., *ApJ*, 770:157, June 2013.

Kendall, S., Kennicutt, R. C., & Clarke, C., *MNRAS*, 414:538–564, June 2011.

Khachikian, E. Y. & Weedman, D. W., *ApJ*, 192:581–589, September 1974.

Khorunzhev, G. A., Sazonov, S. Y., Burenin, R. A., & Tkachenko, A. Y., *Astronomy Letters*, 38:475–491, August 2012.

Kilborn, V. A., Koribalski, B. S., Forbes, D. A., Barnes, D. G., & Musgrave, R. C., *MNRAS*, 356:77–88, January 2005.

Kim, W.-T. & Elmegreen, B. G., *ApJ*, 841:L4, May 2017.

Korchagin, V., Kikuchi, N., Miyama, S. M., Orlova, N., & Peterson, B. A., *ApJ*, 541: 565–578, October 2000.

Kormendy, J. & Ho, L. C., *ARA&A*, 51:511–653, August 2013.

Kormendy, J. & Richstone, D., *ARA&A*, 33:581, 1995.

Krajnović, D., Cappellari, M., de Zeeuw, P. T., & Copin, Y., *MNRAS*, 366:787–802, March 2006.

Krips, M., Eckart, A., Neri, R., Pott, J. U., Leon, S., Combes, F., García-Burillo, S., Hunt, L. K., Baker, A. J., Tacconi, L. J., Englmaier, P., Schinnerer, E., & Boone, F., *A&A*, 442:479–493, November 2005.

Landi, R., Malizia, A., & Bassani, L., *A&A*, 441:69–82, October 2005.

Laor, A. *What is the Broad Line Region?* In Richards, G. T. & Hall, P. B., editors, *AGN Physics with the Sloan Digital Sky Survey*, volume 311 of *Astronomical Society of the Pacific Conference Series*, page 169, June 2004.

Lena, D. *Aspects of Supermassive Black Hole Growth in Nearby Active Galactic Nuclei*. PhD thesis, Rochester Institute of Technology, 2015.

Lena, D., Robinson, A., Storchi-Bergman, T., Schnorr-Müller, A., Seelig, T., Riffel, R. A., Nagar, N. M., Couto, G. S., & Shadler, L., *ApJ*, 806:84, June 2015.

Leroy, A. K., Walter, F., Martini, P., Roussel, H., Sandstrom, K., Ott, J., Weiss, A., Bolatto, A. D., Schuster, K., & Dessauges-Zavadsky, M., *ApJ*, 814:83, December 2015.

Levenson, N. A., Radomski, J. T., Packham, C., Mason, R. E., Schaefer, J. J., & Telesco, C. M., *ApJ*, 703:390–398, September 2009.

Liu, G., Zakamska, N. L., Greene, J. E., Nesvadba, N. P. H., & Liu, X., *MNRAS*, 436: 2576–2597, December 2013.

Lynden-Bell, D. & Rees, M. J., *MNRAS*, 152:461, 1971.

Ma, J., *Chinese J. Astron. Astrophys.*, 1, October 2001.

Maciejewski, W., *MNRAS*, 354:883–891, November 2004a.

Maciejewski, W., *MNRAS*, 354:892–904, November 2004b.

Mahony, E. K., Oonk, J. B. R., Morganti, R., Tadhunter, C., Bessiere, P., Short, P., Emonts, B. H. C., & Oosterloo, T. A., *MNRAS*, 455:2453–2460, January 2016.

Maiolino, R., Russell, H. R., Fabian, A. C., Carniani, S., Gallagher, R., Cazzoli, S., Arribas, S., Belfiore, F., Bellocchi, E., Colina, L., Cresci, G., Ishibashi, W., Marconi, A., Mannucci, F., Oliva, E., & Sturm, E., *Nature*, 544:202–206, March 2017.

Makarov, D., Prugniel, P., Terekhova, N., Courtois, H., & Vauglin, I., *A&A*, 570:A13, October 2014.

Malkan, M. A., Gorjian, V., & Tam, R., *ApJS*, 117:25–88, July 1998.

Martini, P. *Why does low-luminosity AGN fueling remain an unsolved problem?* In Storchi-Bergmann, T., Ho, L. C., & Schmitt, H. R., editors, *The Interplay Among Black Holes, Stars and ISM in Galactic Nuclei*, volume 222 of *IAU Symposium*, pages 235–241, November 2004. doi: 10.1017/S1743921304002170.

Martini, P., Pogge, R. W., Ravindranath, S., & An, J. H., *ApJ*, 562:139–151, November 2001.

Martini, P., Regan, M. W., Mulchaey, J. S., & Pogge, R. W., *ApJ*, 589:774–782, June 2003.

McGaugh, S. S. & Schombert, J. M., *AJ*, 148:77, November 2014.

McMullin, J. P., Waters, B., Schiebel, D., Young, W., & Golap, K. *CASA Architecture and Applications*. In Shaw, R. A., Hill, F., & Bell, D. J., editors, *Astronomical Data Analysis Software and Systems XVI*, volume 376 of *Astronomical Society of the Pacific Conference Series*, page 127, October 2007.

Mezcua, M., Prieto, M. A., Fernández-Ontiveros, J. A., Tristram, K., Neumayer, N., & Kotilainen, J. K., *MNRAS*, 452:4128–4144, October 2015.

Morganti, R., Tsvetanov, Z. I., Gallimore, J., & Allen, M. G., *A&AS*, 137:457–471, June 1999.

Morganti, R., Peck, A. B., Oosterloo, T. A., van Moorsel, G., Capetti, A., Fanti, R., Parma, P., & de Ruiter, H. R., *A&A*, 505:559–567, October 2009.

Morganti, R., Frieswijk, W., Oonk, R. J. B., Oosterloo, T., & Tadhunter, C., *A&A*, 552: L4, April 2013.

Morganti, R., Oosterloo, T. A., Oonk, J. B. R., Frieswijk, W., & Tadhunter, C. N. *Radio Jets Clearing the Way Through a Galaxy: Watching Feedback in Action in the Seyfert Galaxy IC 5063*. In Iono, D., Tatematsu, K., Wootten, A., & Testi, L., editors, *Revolution in Astronomy with ALMA: The Third Year*, volume 499 of *Astronomical Society of the Pacific Conference Series*, page 125, December 2015.

Moustakas, J., Kennicutt, Jr., R. C., Tremonti, C. A., Dale, D. A., Smith, J.-D. T., & Calzetti, D., *ApJS*, 190:233-266, October 2010.

Mulchaey, J. S., Regan, M. W., & Kundu, A., *ApJS*, 110:299–319, June 1997.

Müller-Sánchez, F., Prieto, M. A., Hicks, E. K. S., Vives-Arias, H., Davies, R. I., Malkan, M., Tacconi, L. J., & Genzel, R., *ApJ*, 739:69, October 2011.

Müller-Sánchez, F., Comerford, J., Stern, D., & Harrison, F. A., *ApJ*, 830:50, October 2016.

Mundell, C. G. & Shone, D. L., *MNRAS*, 304:475–480, April 1999.

Nagar, N. M., Wilson, A. S., Mulchaey, J. S., & Gallimore, J. F., *ApJS*, 120:209–245, February 1999.

Nelson, C. H. & Whittle, M., *ApJS*, 99:67, July 1995.

Nelson, C. H., Green, R. F., Bower, G., Gebhardt, K., & Weistrop, D., *ApJ*, 615:652–661, November 2004.

Nesvadba, N. P. H., Boulanger, F., Salomé, P., Guillard, P., Lehnert, M. D., Ogle, P., Appleton, P., Falgarone, E., & Pineau Des Forets, G., *A&A*, 521:A65, October 2010.

Norman, C. A., Sellwood, J. A., & Hasan, H., *ApJ*, 462:114, May 1996.

Osterbrock, D. E., *ApJ*, 249:462–470, October 1981.

Osterbrock, D. E., *QJRAS*, 25:1, March 1984.

Pence, W. D., Taylor, K., & Atherton, P., *ApJ*, 357:415–425, July 1990.

Pérez-Ramírez, D., Knapen, J. H., Peletier, R. F., Laine, S., Doyon, R., & Nadeau, D., *MNRAS*, 317:234–248, September 2000.

Perley, R. A., Dreher, J. W., & Cowan, J. J., *ApJ*, 285:L35–L38, October 1984.

Pfefferkorn, F., Boller, T., & Rafanelli, P., *A&A*, 368:797–816, March 2001.

Querejeta, M., Meidt, S. E., Schinnerer, E., García-Burillo, S., Dobbs, C. L., Colombo, D., Dumas, G., Hughes, A., Kramer, C., Leroy, A. K., Pety, J., Schuster, K. F., & Thompson, T. A., *A&A*, 588:A33, April 2016.

Ramakrishnan, V., Nagar, N. M., Slater, R., Finlez, C., Storchi-Bergmann, T., Schnorr-Mller, A., Riffel, R. A., Mundell, C. G., & Robinson, A., 2018.

Regan, M. W. & Teuben, P. J., *ApJ*, 600:595–612, January 2004.

Riffel, R., Riffel, R. A., Ferrari, F., & Storchi-Bergmann, T., *MNRAS*, 416:493–500, September 2011.

Riffel, R. A., *Ap&SS*, 327:239–244, June 2010.

Riffel, R. A., Storchi-Bergmann, T., Winge, C., McGregor, P. J., Beck, T., & Schmitt, H., *MNRAS*, 385:1129–1142, April 2008.

Riffel, R. A., Storchi-Bergmann, T., Riffel, R., & Pastoriza, M. G., *ApJ*, 713:469–474, April 2010.

Riffel, R. A., Storchi-Bergmann, T., & Winge, C., *MNRAS*, 430:2249–2261, April 2013.

Roche, N., Humphrey, A., Lagos, P., Papaderos, P., Silva, M., Cardoso, L. S. M., & Gomes, J. M., *MNRAS*, 459:4259–4280, July 2016.

Rodríguez-Ardila, A., Prieto, M. A., Mazzalay, X., Fernández-Ontiveros, J. A., Luque, R., & Müller-Sánchez, F., *MNRAS*, 470:2845–2860, September 2017.

Roy, A. L., Norris, R. P., Kesteven, M. J., Troup, E. R., & Reynolds, J. E., *ApJ*, 432: 496–507, September 1994.

Sakamoto, K., Okumura, S. K., Ishizuki, S., & Scoville, N. Z., *ApJ*, 525:691–701, November 1999.

Sakamoto, K., Aalto, S., Combes, F., Evans, A., & Peck, A., *ApJ*, 797:90, December 2014.

Scannapieco, E., *ApJ*, 837:28, March 2017.

Schinnerer, E., Eckart, A., Tacconi, L. J., Genzel, R., & Downes, D., *ApJ*, 533:850–868, April 2000.

Schmidt, M. & Green, R. F., *ApJ*, 269:352–374, June 1983.

Schmitt, H. R. & Kinney, A. L., *ApJ*, 463:498, June 1996.

Schmitt, H. R., Ulvestad, J. S., Antonucci, R. R. J., & Kinney, A. L., *ApJS*, 132:199–209, February 2001.

Schnorr-Müller, A., Storchi-Bergmann, T., Nagar, N. M., & Ferrari, F., *MNRAS*, 438: 3322–3331, March 2014a.

Schnorr-Müller, A., Storchi-Bergmann, T., Nagar, N. M., Robinson, A., Lena, D., Riffel, R. A., & Couto, G. S., *MNRAS*, 437:1708–1724, January 2014b.

Schnorr-Müller, A., Storchi-Bergmann, T., Ferrari, F., & Nagar, N. M., *MNRAS*, 466: 4370–4380, April 2017a.

Schnorr-Müller, A., Storchi-Bergmann, T., Nagar, N. M., Robinson, A., & Lena, D., *MNRAS*, 471:3888–3898, November 2017b.

Schoenmakers, R. H. M., Franx, M., & de Zeeuw, P. T., *MNRAS*, 292:349, December 1997.

Sellwood, J. A. & Debattista, V. P. *Secular Evolution in Barred Galaxies*. In Sandqvist, A. & Lindblad, P. O., editors, *Lecture Notes in Physics, Berlin Springer Verlag*, volume 474 of *Lecture Notes in Physics, Berlin Springer Verlag*, page 43, 1996. doi: 10.1007/BFb0101964.

Sellwood, J. A. & Wilkinson, A., *Reports on Progress in Physics*, 56:173–256, February 1993.

Seyfert, C. K., *ApJ*, 97:28, January 1943.

Shen, J. & Sellwood, J. A., *ApJ*, 604:614–631, April 2004.

Sheth, K., Vogel, S. N., Regan, M. W., Thornley, M. D., & Teuben, P. J., *ApJ*, 632:217–226, October 2005.

Sheth, K., Regan, M., Hinz, J. L., Gil de Paz, A., Menéndez-Delmestre, K., Muñoz-Mateos, J.-C., Seibert, M., Kim, T., Laurikainen, E., Salo, H., Gadotti, D. A., Laine, J., Mizusawa, T., Armus, L., Athanassoula, E., Bosma, A., Buta, R. J., Capak, P., Jarrett, T. H., Elmegreen, D. M., Elmegreen, B. G., Knapen, J. H., Koda, J., Helou, G., Ho, L. C., Madore, B. F., Masters, K. L., Mobasher, B., Ogle, P., Peng, C. Y., Schinnerer, E., Surace, J. A., Zaritsky, D., Comerón, S., de Swardt, B., Meidt, S. E., Kasliwal, M., & Aravena, M., *PASP*, 122:1397, December 2010.

Silk, J., *ApJ*, 772:112, August 2013.

Simões Lopes, R. D., Storchi-Bergmann, T., de Fátima Saraiva, M., & Martini, P., *ApJ*, 655:718–734, February 2007.

Singh, V., Shastri, P., & Risaliti, G., *A&A*, 532:A84, August 2011.

Slater, R., Finlez, C., Nagar, N. M., Schnorr-Müller, A., Storchi-Bergmann, T., Lena, D., Ramakrishnan, V., Mundell, C. G., Riffel, R. A., Peterson, B., Robinson, A., & Orellana, G., *ArXiv e-prints*, April 2018.

Smajić, S., Moser, L., Eckart, A., Busch, G., Combes, F., García-Burillo, S., Valencia-S., M., & Horrobin, M., *A&A*, 583:A104, November 2015.

Solomon, P. M. & Vanden Bout, P. A., *ARA&A*, 43:677–725, September 2005.

Soltan, A., *MNRAS*, 200:115–122, July 1982.

Sorce, J. G., Tully, R. B., Courtois, H. M., Jarrett, T. H., Neill, J. D., & Shaya, E. J., *MNRAS*, 444:527–541, October 2014.

Spekkens, K. & Sellwood, J. A., *ApJ*, 664:204–214, July 2007.

Storchi-Bergmann, T. *Feeding and feedback in nearby AGN - comparison with the Milky Way center*. In Sjouwerman, L. O., Lang, C. C., & Ott, J., editors, *The Galactic Center: Feeding and Feedback in a Normal Galactic Nucleus*, volume 303 of *IAU Symposium*, pages 354–363, May 2014. doi: 10.1017/S174392131400091X.

Storchi-Bergmann, T., Rodriguez-Ardila, A., Schmitt, H. R., Wilson, A. S., & Baldwin, J. A., *ApJ*, 472:83, November 1996.

Storchi-Bergmann, T., Dors, Jr., O. L., Riffel, R. A., Fathi, K., Axon, D. J., Robinson, A., Marconi, A., & Östlin, G., *ApJ*, 670:959–967, December 2007.

Storchi-Bergmann, T., Lopes, R. D. S., McGregor, P. J., Riffel, R. A., Beck, T., & Martini, P., *MNRAS*, 402:819–835, February 2010.

Storchi-Bergmann, T., Riffel, R. A., Riffel, R., Diniz, M. R., Borges Vale, T., & McGregor, P. J., *ApJ*, 755:87, August 2012.

Sun, A.-L., Greene, J. E., & Zakamska, N. L., *ApJ*, 835:222, February 2017.

Tremaine, S., Gebhardt, K., Bender, R., Bower, G., Dressler, A., Faber, S. M., Filippenko, A. V., Green, R., Grillmair, C., Ho, L. C., Kormendy, J., Lauer, T. R., Magorrian, J., Pinkney, J., & Richstone, D., *ApJ*, 574:740–753, August 2002.

Tully, R. B., Courtois, H. M., Dolphin, A. E., Fisher, J. R., Héraudeau, P., Jacobs, B. A., Karachentsev, I. D., Makarov, D., Makarova, L., Mitronova, S., Rizzi, L., Shaya, E. J., Sorce, J. G., & Wu, P.-F., *AJ*, 146:86, October 2013.

Ulvestad, J. S. & Ho, L. C., *ApJ*, 558:561–577, September 2001.

Urry, C. M. & Padovani, P., *PASP*, 107:803, September 1995.

van der Kruit, P. C. & Freeman, K. C., *ApJ*, 278:81–88, March 1984.

van der Laan, T. P. R., Schinnerer, E., Boone, F., García-Burillo, S., Combes, F., Haan, S., Leon, S., Hunt, L., & Baker, A. J., *A&A*, 529:A45, May 2011.

Veilleux, S. & Rupke, D. S., *ApJ*, 565:L63–L66, January 2002.

Veilleux, S., Cecil, G., & Bland-Hawthorn, J., *ARA&A*, 43:769–826, September 2005.

Wada, K., *PASJ*, 46:165–172, April 1994.

Weaver, K. A., Wilson, A. S., & Baldwin, J. A., *ApJ*, 366:50–63, January 1991.

Westoby, P. B., Mundell, C. G., Nagar, N. M., Maciejewski, W., Emsellem, E., Roth, M. M., Gerssen, J., & Baldry, I. K., *ApJS*, 199:1, March 2012.

Wong, T., Blitz, L., & Bosma, A., *ApJ*, 605:183–204, April 2004.

Woo, J.-H. & Urry, C. M., *ApJ*, 579:530–544, November 2002.

Woo, J.-H., Treu, T., Barth, A. J., Wright, S. A., Walsh, J. L., Bentz, M. C., Martini, P., Bennert, V. N., Canalizo, G., Filippenko, A. V., Gates, E., Greene, J., Li, W., Malkan, M. A., Stern, D., & Minezaki, T., *ApJ*, 716:269–280, June 2010.

Xie, F.-G., Yuan, F., & Ho, L. C., *ApJ*, 844:42, July 2017.

Yu, Q. & Tremaine, S., *MNRAS*, 335:965–976, October 2002.